NTNU – Trondheim
Norwegian University of
Science and Technology

Hyperspectral Imaging of In Vitro Wound Models from Human Skin

Ingvild Johanne
Åsmundhavn Haneberg

Master of Science in Physics and Mathematics	
Submission date:	September 2014
Supervisor:	Morten Kildemo, IFY
Co-supervisor:	Lise Lyngsnes Randeberg, IET

Norwegian University of Science and Technology
Department of Physics

Master thesis

Hyperspectral imaging of in vitro wound models from human skin

---

Ingvild Haneberg

Norwegian University of Science and Technology

NTNU
Det skapende universitet

15. september 2014

Abstract

In vitro wounds from human skin have been analysed using hyperspectral imaging. The purpose of this research is to use hyperspectral imaging as a diagnosis tool for skin wounds. The imaging period was 22 days.

The images were analysed using Matlab. This includes noise removal, calibration to reflectance, RGB image analysis, reflectance spectrum analysis, spectral angle mapper and Monte Carlo. From this analysis, reflectance maxima and minima were identified, the change in reflectance values with time, chromophores and cytochromes in skin were indentified and classification analysis were performed to study the change in relative ratios of pixels of the different classes.

Results from the analysis show that the reflectance decreases with time, skin has the lowest reflectance and wound has the highest reflectance. Some samples showes signs of healing, but no samples healed completely. An infection occurred in some of the samples between day 8 and day 10, and this infection is detectable in reflectance spectrums and to some extent in SAM classifications.

Sammendrag

Denne oppgaven omhandler hyperspektral avbildning av in vitro sår fra menneskehud. Formålet med dette er å bruke hyperspektral avbildning til diagnose av hudsår. Avbildningsperioden var 22 dager.

Bildene ble analysert med Matlab. Dette omfatter støyfjerning, kalibrering til reflektans, analyse av RGB-bilder, analyse av reflektansspektrum, spectral angle mapper og Monte Carlo. Denne analysen førte til at minima og maksima fra reflektansspektre ble identifisert, endringen i reflektans som følge av tid, identifisering av kromoforer og cytokromer i hud og klassifiseringsanalyse ble gjort for å følge endringen i relative forholdet av piksler mellom de ulike klassene.

Resultater fra analysen tyder på at reflektans minker med tiden, og at huden har den laveste reflektansen og såret har den høyeste reflektansen. Noen sårmodeller viser tegn på heling, men ingen av sårmodellene helet komplett. Det oppstod en infeksjon i noen av sårmodellen mellom dag 8 og dag 10, og denne infeksjonen kan detekteres i reflektansspektrum og til en viss grad i SAM-klassifiseringen.

Preface

This thesis is the final part of a Master of Technology in Engineering Physics at The Norwegian University of Science and Technology (NTNU). The work was conducted at the Department of Electronics and Telecommunication (IET) and at the Department of Cancer Research and Molecular Medicine at the Faculty of Medicine at St Olavs Hospital in Trondheim.

This thesis is based on previous work performed by the author [1]. Parts from the previous work has been reused in various sections of this thesis, in particularly the theory chapter. If not stated otherwise, all images and figures are produced by and belong to me.

I would like to sincerely thank my supervisors Lise Lyngsnes Randeberg and Morten Kildemo, for all help, support and opportunities. I would also like to thank Matija Milanic, Brita Pukstad, Tore Landsem, Lukasz Paluchowski, Ivan Pavlovic and Asgeir Bjørgan for invaluable help and support.

Ingvild Haneberg
September 2014, NTNU Trondheim

Table of contents

List of figures **10**

List of tables **10**

1 Introduction **16**

2 Theory **18**

2.1 Skin 18

2.1.1 Reepithelializing 19

2.1.2 Cytochromes 21

2.2 Optical reflectance and transmission 23

2.2.1 Absorption 23

2.2.2 Scattering 25

2.2.3 Extinction 27

2.3 Transport of light in tissue 27

2.3.1 Diffusion theory 28

2.3.2 Monte Carlo simulation 29

2.4 Hyperspectral imaging 32

2.5 Noise removal 32

2.6 Spectral angle mapper SAM 34

3 Methods of analysis **35**

3.1 Preparation 35

3.1.1 Preparation of the samples 35

3.1.2 Experimental setup 44

3.2 Hyperspectral imaging procedure 45

3.3 Analysis of data 48

3.3.1 White light images 48

4 Results and discussion **51**

4.1 Experimental setup 51

4.2 Sample health 52

4.3 White light images 52

4.3.1 RGB images of wound models 53

4.3.2 Reflectance spectrums 57

4.3.3 Normalized reflectance spectrums 68

4.3.4 Chromophores 74
4.3.5 Spectral angle mapper 76
4.3.6 Relative ratios SAM analysis 80
4.3.7 Monte Carlo simulation 83

5 Conclusions 84

A Appendix 90

A.1 Reading header files 90
A.2 Import images 93
A.3 Convert to reflectance 97
A.4 Forward MNF transformation 98
A.5 Inverse MNF transformation 102
A.6 Create RGB image of sample 103
A.7 Select pixels from the classes skin, wound and wound edge 104
A.8 Plot the average reflectance 107
A.9 Spectral angle mapper 109
A.10 Plot SAM results 110
A.11 Plotting normalized reflectance spectrums 111
A.12 RGB images of samples 114
A.12.1 Tray I 114
A.12.2 Tray II 116
A.12.3 Tray III 118
A.13 Reflectance spectrums 120
A.13.1 Tray I 120
A.13.2 Tray II 124
A.13.3 Tray III 129
A.13.4 Normalized reflectance spectrums 133
A.14 Relative ratios SAM 137

List of figures

1 The composition of epidermis [10]. 18
2 The composition of dermis [13]. 19
3 Reepithelialization phases [14]. 20
4 Migration of the activated keratinocytes [14]. 21
5 Absorption spectrum of cytochrome c [17] 22
6 The absorption coefficient of blood, methemoglobin, water and the melanin model for sun-protected North-European skin ($\mu_{a,m,694} = 350\text{m}^{-1}$) [19]. 24
7 Program flow in MCML, reproduced from [7]. 31
8 Donated skin piece. 35
9 Illustration of the wound models. 36
10 Sample holder insert seen from above. 37
11 Sample holder insert seen from above. 38
12 Sample holder insert seen from above. 39
13 Sample holder insert seen from the side. 39
14 Well tray I with infected wound models. Photo by Brita Pukstad. . 40
15 Well tray II with infected wound models. Photo by Brita Pukstad. 41
16 Well tray III with infected wound models. Photo by Brita Pukstad. 41
17 Well tray I without infected wound models. 42
18 Well tray II without infected wound models. 42
19 Well tray III without infected wound models. 43
20 Imaging setup. 44
21 Imaging setup. 45
22 Sample holder insert seen from the side. 46
23 Schematic of the optical layout of the HySpex VNIR-1600 hyperspectral camera [31]. 47
24 Average reflectance of white reference standard. 52
25 RGB image of I-1-A on day 1 53
26 RGB image of I-4-A on day 1 54
27 RGB image of II-1-A on day 2 55
28 RGB image of II-3-A on day 2 55
29 RGB image of III-5-A on day 1 56
30 Average reflectance spectrum of skin, wound and wound edge for I-1-A from day 1 57

31 Average reflectance spectrum of skin, wound and wound edge for I-1-A from day 8 58
32 Average reflectance spectrum of skin, wound and wound edge for III-5-A from day 1 59
33 Average reflectance spectrum of skin, wound and wound edge for III-5-A from day 8 60
34 Average reflectance spectrum of skin, wound and wound edge for III-5-A from day 16 61
35 Average reflectance spectrum of skin, wound and wound edge for III-5-A from day 22 62
36 Average reflectance spectrum of skin, wound and wound edge for II-3-A from day 2 63
37 Average reflectance spectrum of skin, wound and wound edge for II-3-A from day 8 64
38 Average reflectance spectrum of the skin I-1-A 65
39 Average reflectance spectrum of the wound I-1-A 66
40 Average reflectance spectrum of the wound edge I-1-A 66
41 Average reflectance spectrum of the skin I-4-A 67
42 Average reflectance spectrum of the medium from day 1 68
43 Normalized average reflectance spectrum of the skin I-1-A 69
44 Normalized average reflectance spectrum of the wound I-1-A . . . 70
45 Normalized average reflectance spectrum of the edge I-1-A 70
46 Normalized average reflectance spectrum of the skin I-4-A 71
47 Normalized average reflectance spectrum of the skin III-5-A 72
48 Normalized average reflectance spectrum of the wound III-5-A . . 73
49 Normalized average reflectance spectrum of the edge III-5-A . . . 73
50 SAM I-1-A day 1, 8 and 10. 77
51 SAM I-1-A day 1, 8, 16 and 22. 78
52 SAM III-2-A day 1, 8, 16 and 22. 79
53 Relative ratios of skin, wound and wound edge from SAM of I-1-A. 80
54 Relative ratios of skin, wound and wound edge from SAM of I-5-A. 81
55 Monte Carlo simulation of bloodless skin and wound. 83
56 RGB image of I-2-A on day 1 114
57 RGB image of I-3-A on day 1 115
58 RGB image of II-2-A on day 2 116
59 RGB image of II-6-A on day 2 117
60 RGB image of III-1-A on day 1 118

61 RGB image of III-2-A on day 1 119
62 RGB image of III-3-A on day 1 119
63 Average reflectance spectrum of skin, wound and wound edge for I-2-A from day 1 120
64 Average reflectance spectrum of skin, wound and wound edge for I-2-A from day 8 121
65 Average reflectance spectrum of skin, wound and wound edge for I-5-A from day 1 121
66 Average reflectance spectrum of skin, wound and wound edge for I-5-A from day 8 122
67 Average reflectance spectrum of skin, wound and wound edge for I-5-A from day 16 122
68 Average reflectance spectrum of skin, wound and wound edge for I-5-A from day 22 123
69 Average reflectance spectrum of skin, wound and wound edge for II-2-A from day 2 124
70 Average reflectance spectrum of skin, wound and wound edge for II-2-A from day 8 125
71 Average reflectance spectrum of skin, wound and wound edge for II-2-A from day 16 125
72 Average reflectance spectrum of skin, wound and wound edge for II-2-A from day 22 126
73 Average reflectance spectrum of skin, wound and wound edge for II-6-A from day 2 126
74 Average reflectance spectrum of skin, wound and wound edge for II-6-A from day 8 127
75 Average reflectance spectrum of skin, wound and wound edge for II-6-A from day 16 127
76 Average reflectance spectrum of skin, wound and wound edge for II-6-A from day 22 128
77 Average reflectance spectrum of skin, wound and wound edge for III-2-A from day 1 129
78 Average reflectance spectrum of skin, wound and wound edge for III-2-A from day 8 130
79 Average reflectance spectrum of skin, wound and wound edge for III-2-A from day 16 130

80 Average reflectance spectrum of skin, wound and wound edge for III-2-A from day 22 131
81 Average reflectance spectrum of skin, wound and wound edge for III-3-A from day 1 131
82 Average reflectance spectrum of skin, wound and wound edge for III-3-A from day 8 132
83 Normalized average reflectance spectrum of the skin I-2-A 133
84 Normalized average reflectance spectrum of the wound I-2-A . . . 134
85 Normalized average reflectance spectrum of the edge I-2-A 134
86 Normalized average reflectance spectrum of the skin II-1-A 135
87 Normalized average reflectance spectrum of the skin II-3-A 135
88 Normalized average reflectance spectrum of the wound II-3-A . . 136
89 Normalized average reflectance spectrum of the edge II-3-A 136
90 Relative ratios of skin, wound and wound edge from SAM of I-2-A. 137
91 Relative ratios of skin, wound and wound edge from SAM of II-2-A. 137
92 Relative ratios of skin, wound and wound edge from SAM of II-3-A. 138
93 Relative ratios of skin, wound and wound edge from SAM of II-6-A. 138
94 Relative ratios of skin, wound and wound edge from SAM of III-2-A.139
95 Relative ratios of skin, wound and wound edge from SAM of III-5-A.139

List of tables

1 Comparison of various medical imaging modalities 16
2 Specifications for HySpex VNIR-1600 46
3 Specifications for diffuse reflectance standard 47
4 Characteristic maxima and minima for intact skin 74
5 Characteristic maxima and minima for wound 74
6 Characteristic maxima and minima for wound edge 75

1 Introduction

The human skin is susceptible to wounds caused by accidents or illness, and as most wounds heals without complications, in some cases it is helpful or even necessary to be able to know how or if the wound is healing at all. The healing of wounds in human skin is a complex process that involves cell migration, proliferation and differentiation [2]. This thesis aims to show that hyperspectral imaging can be used and utilized as a tool for diagnosis of skin wounds. Hyperspectral imaging is an imaging technique that combines spectroscopy and imaging and allows the recording of the entire spectrum for every pixel on the entire image. The data produced can then be analyzed and used for diagnosis [3].

The origin of hyperspectral imaging is military use, as it was developed as a tool for satellite imaging [4]. The purposes of this is mainly finding objects, identifying materials, or detecting processes. Within the field of biomedical optics, hyperspectral imaging has been used for detection and characterization of advanced atherosclerotic plaques in vitro [5], monitoring tumor hypoxia, cancer detection [4] and assessing the risk of diabetic foot ulcer development [6].

The mostly used tecniques used in medical imaging are x-ray, ultrasound, computed tomography and magnetic resonnance imaging. Comparing optical imaging with these other methods, as in table 1 [7], it is apparent that there would be many advantages to use optical imaging:

Table 1: Comparison of various medical imaging modalities

Characteristics	X-ray imaging	Ultrasonography	MRI	Optical imaging
Soft-tissue contrast	poor	good	excellent	excellent
Spatial resolution	excellent	good	good	mixed
Maximum imaging depth	excellent	good	excellent	good
Function	none	good	excellent	excellent
Nonionizing radiation	no	yes	yes	yes
Data acquisition	fast	fast	slow	fast
Cost	low	low	high	low

The human skin is divided into three layers; epidermis, dermis and hypodermis.

The epidermis is the outer protective layer, dermis is where the blood vessels are, nourishing the skin, and the hypodermis is mainly fat cells. Light penetrates through the first two layers, and can be reflected back. By measuring the amount of reflected light, it is possible to aquire information about structures in the skin.

There are several benefits of using optical imaging in biological tissue. Some of these are listed below [7]:

- Optical photons provide nonionizing and safe radiation for medical application.
- Optical spectra - based on absorption, fluorescence, or Raman scattering - provide biochemical information because they are related to molecular conformation.
- Optical absorption provides contrast for functional imaging.
- Optical scattering spectra provides information about the size distribution of optical scatterers, such as cell nuclei.
- Optical polarization provides information about structurally anisotropic tissue components, such as collagen and mucle fiber.

The purpose of this research is to use hyperspectral imaging in the diagnosis of wound healing. The imaging has been done in vitro with human skin samples derived from excess skin after plastic abdominal surgery. It is important to use human skin instead of a skin imitation model to be able to accurately study the healing process of a wound. Several in vitro and in vivo models have previously been used to study skin wounds but human wounds in vivo are variable and difficult to sample, and the healing process is influenced by the nutritional status of the patient, the circulation, age, infections and initial treatment of the wound [2].

Previous work on this subject has shown that it is possible to use hyperspectral imaging in skin wound diagnosis [8]. The use of a hyperspectral imaging setup would provide a simple and fast diagnosis of the skin wound. In this project, the hyperspectral images have been analysed by examining change and differences in reflectance spectrums, spectral angle mapper classification and Monte Carlo simulation.

2 Theory

This chapter includes an overview of the composition of the human skin and the processes included in wound healing, optical properties of the skin, light propagation in skin and an introduction to hyperspectral imaging. The principles of the image analysis will also be presented.

2.1 Skin

The human skin is named cutis, and is composed of two layers, a top layer called epidermis and a bottom layer called dermis. Below dermis, there is a subcutaneous fat layer.

The epidermis varies in thickness from 0,3 mm to 1,5 mm, and consists of a multilayer plate epitel. Almost all of the cells in epidermis, around 90%, are keratinocytes [9]. The epidermis is further divided into layers called strata. These layers are the basale layer, the spinous layer, the granular layer and the corneum layer, as seen in Figure 1[10].

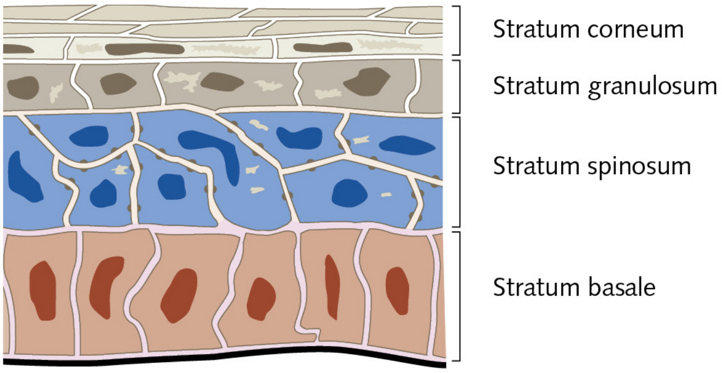

Figure 1: The composition of epidermis [10].

The basal cells undergo mitosis, leading to a renewal of the epidermis. During the growth of new cells, the older cells get pushed upwards in the epidermis. So as the cells mature, they travel upwards. The new keratinocytes change structure during maturing, and eventually become flat squamous cells in the stratum corneum. The keratinocytes syntesizes keratins, which are structural proteins. Keratin are together with filaggrin tightly packed in arrays. This leads to the flattening of the cells and gives the structure of the stratum corneum [11]. There are no blood vessels in the epidermis, which means that that the epidermis and especially the stratum basale relies on the dermis for nutrition [12].

The dermis, which is located below the epidermis, varies in thickness from 1,4 mm to 4 mm. Dermis consists of collagen and elastic fibers, and is divided into two layers, where the lower is called the reticular dermis and the upper is called the papillary dermis [9]. An illustration of the composition of dermis can be seen in Figure 2 [13].

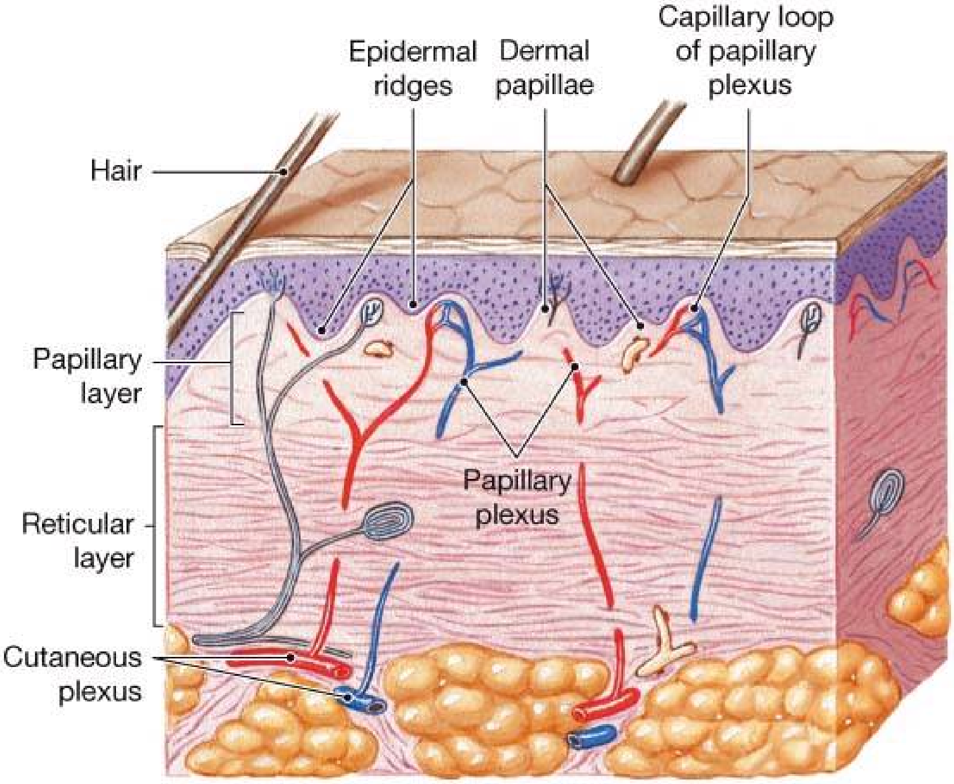

Figure 2: The composition of dermis [13].

Most of the cells in the dermis are fibroblasts or macrophages. The fibroblasts are mainly distributed in the papillary dermis, producing the protein fibres collagen and elastin fibres and renewing the extracellular matrix. The macrophages eliminate foreign material and damaged tissue [11].

2.1.1 Reepithelializing

The repair of the skin after injury is called reepithelializing. Wound healing is a process that can be divided into four overlapping phases [14]. These phases are

- Inflammation and clot formation

- Keratinocyte activation and migration
- Remodeling of the basement membrane and extracellular matrix
- Dermal and epidermal maturation

Reepithelializing occurs during the final three of these stages.The reepithelializing process begins with keratinocytes migrating from the edges of the wound, followed by their proliferation, stratification and redifferentiation to form an intact epithelium [14]. An illustration of the reepithelialization phases can be seen in Figure 3 [14].

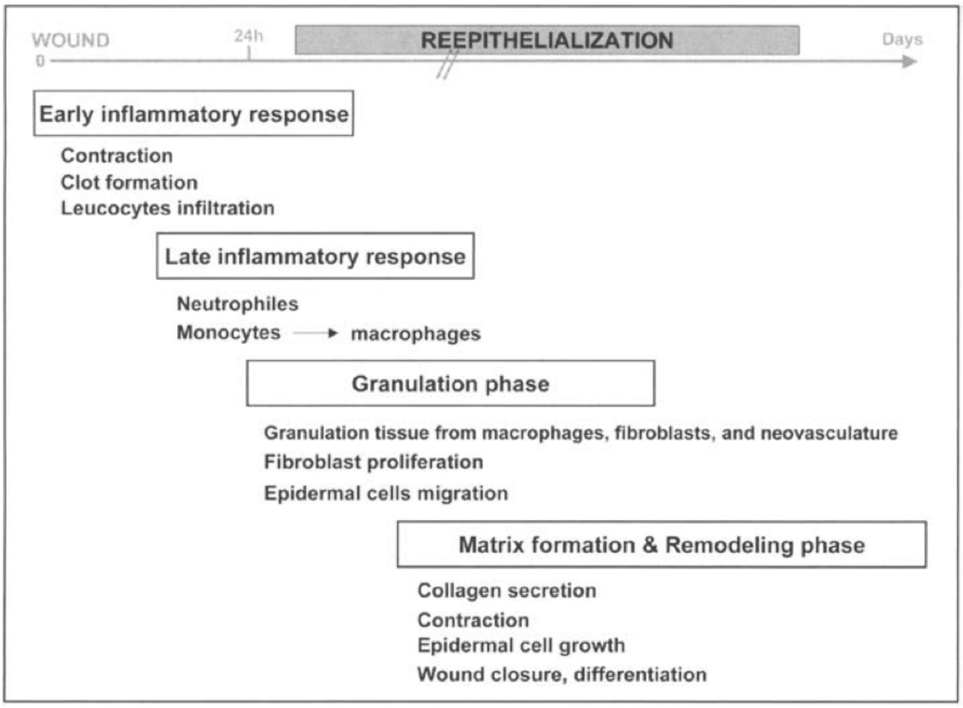

Figure 3: Reepithelialization phases [14].

As seen in Figure 3, the healing process of a wound starts 12 to 24 hours adter the wound occurs. After the wound is made, the first phase is initiated by local inflammation leading to the formation of a fibrin clot. The blood vessels contract and decrease the wound extent. The leucocytes start to infiltrate, and provides a source of neutrophils, monocytes (which mature to macrophages), cytokines and growth factors which amplify the wound signal. In the next phase, the granulation phase, macrophages, keratinocytes and fibroblasts gets activated, leading to the formation of granulation tissues. When the wound is completely covered by this tissue, the wound can close. Activated keratinocytes migrate from the wound margins in the bottom layers of epidermis to the granulation tissue, as seen in Figure 4 [14].

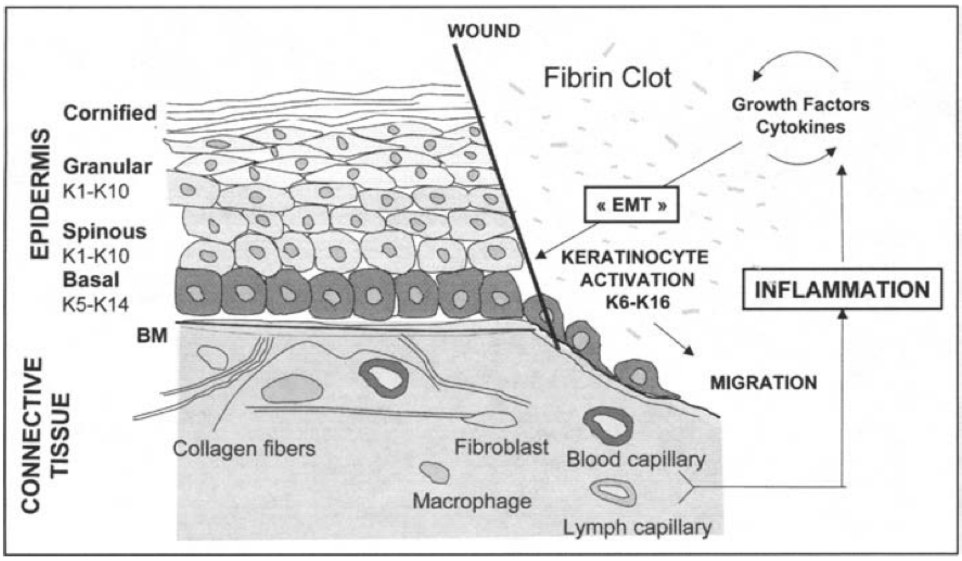

Figure 4: Migration of the activated keratinocytes [14].

Only one layer of keratinocytes will migrate from the wound margins and towards the middle of the wound, and after the whole wound is covered, the keratinocytes will start to differentiate. After the whole healing process is completed, the structure of epidermis will be reestablished.

2.1.2 Cytochromes

A cytochrome complex is a heme protein. Cytochromes carries electrons and protons across the cell membrane [15]. Cytochrome c is known for its function in the mitochondria. Here, it is a key participant in the life-supporting function of ATP synthesis [16].

Figure 5 shows the absorption spectrum of cytochrome c. This can be used to identify possible cytochrome peaks in spectrums from human skin.

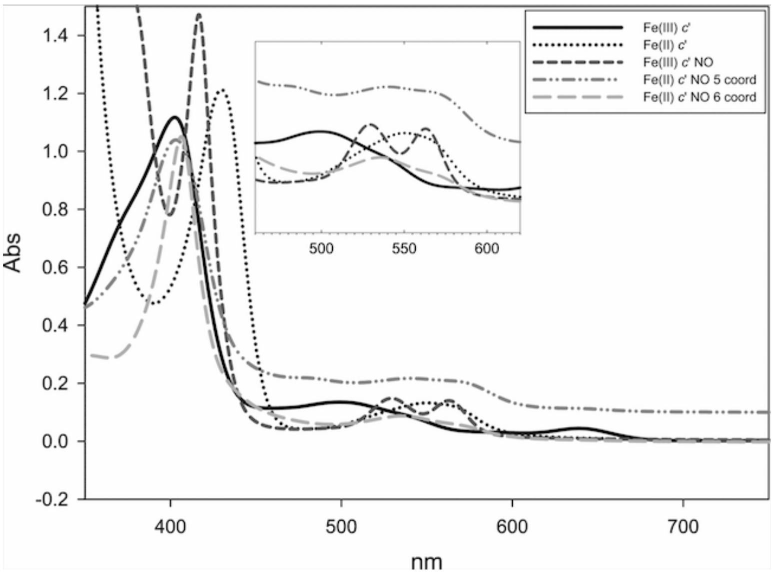

Figure 5: Absorption spectrum of cytochrome c [17]

2.2 Optical reflectance and transmission

Light is electromagnetic ratiation with the properties of waves. The electromagnetic spectrum can be divided into band based on the wavelength [18]. In hyperspectral imaging, the light source appears as a plane wave. Biological tissues are referred to as scattering media, resulting from the strong optical scattering that characterized the tissues [7].

2.2.1 Absorption

Tissue can absorb photons so that electrons can be elevated to an excited state. This electron can then relax to the ground state and give off luminescence or heat. The intensity of the absorbed light in an ideal absorbing medium, assuming zero scattering, is proportional to the absorbing cross-sectional are σ_a of the object. This absorption cross-sectional area is related to the geometric cross-sectional area of the absorber,

$$\sigma_a = Q_a \sigma_g, \tag{1}$$

where Q_a is the absorption efficiency, and σ_g is the geometric cross-sectional area. If there are more than one absorbing object, the total absorbing cross-sectional are is the sum of the individual areas,

$$\sigma_{a,tot} = \sigma_{a,1} + \sigma_{a,2} + \cdots + \sigma_{a,N}, \tag{2}$$

where $\sigma_{a,i}$ denotes the individual cross-sectional areas and N is the total number of absorbers.

The absorption coefficient μ_a is defined as the probability of photon absorption in a medium, per unit path length,

$$\mu_a = N_a \sigma_a, \tag{3}$$

where N_a is the number density of absorbers and σ_a is the absorption cross-sectional area. Assuming an ideal absorber, there will be no scattering, and the the absorption cross section σ_a indicates the absorption capability. Light is attenuated as it propagates in an ideal absorber, this can be expressed as

$$\frac{dI}{I} = -\mu_a dx, \tag{4}$$

where I is the light intensity and x is the distance along the propagation direction. Equation (4) means that the percentage of light that is absorbed in the interval $(x, x + dx)$ is proportional to the product of μ_a and dx. Equation (4) can be integrated into Beer law,

$$I(x) = I_0 e^{-\mu_a dx}, \tag{5}$$

where I_0 is the light intensity at $x = 0$. The minus sign in both equation (4) and equation (5) is due to the light beeing attenuated as it propagates in the tissue. Beer law states that there is a logarithmic relation between the absorption coefficient of the tissue and the length of the propagation path. For equation (5) to be valid, the absorbers must be independent of each other, the absorbing medium must be homogeneous at the site of action and the incoming radiation must be coherent and monochromatic.

The most important absorbers in biological tissue are hemoglobin, melanin, water, bilirubin, beta-carotene and lipids [7]. Figure 6 [19] shows the absorption spectra for melanin, hemoglobin and water. The absorption spectra are multiplied by their volume fractions and summed to yield the total, wavelength-dependent dermal absorption coefficient [19]. The epidermal melanin amount is denoted by the melanin absorption at 694 nm ($\mu_{a,m,694}$) [19].

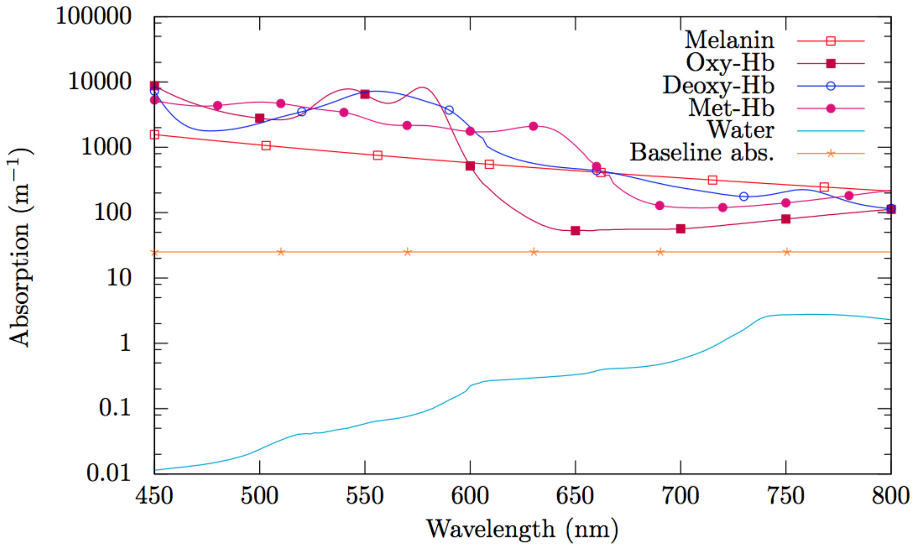

Figure 6: The absorption coefficient of blood, methemoglobin, water and the melanin model for sun-protected North-European skin ($\mu_{a,m,694} = 350\text{m}^{-1}$) [19].

2.2.2 Scattering

In addition to beeing absorbing, biological tissue is also scattering. Assuming an ideal scattering medium, with $\mu_a = 0$, the intensity of the scattered light is proportional to the scattering cross-sectional area σ_s of the object. The scattering cross-sectional area is proportional to the geometric cross-sectional area of the scatterer,

$$\sigma_s = Q_s \sigma_g, \tag{6}$$

where Q_s is the scattering efficiency and σ_g is the geometric cross-sectonal area of the scatterer. In tissue, there are multiple scattering objects, and the total scattering cross section is the sum of the individual scattering cross-sectional areas,

$$\sigma_{s,tot} = \sigma_{s,1} + \sigma_{s,2} + \cdots + \sigma_{s,N}, \tag{7}$$

where $\sigma_{s,i}$ denotes the individual cross-sectional areas and N is the total number of scatterers.

The scattering coefficient μ_s is defined as the probability of photon scattering in a medium per unit path length. The scattering coefficient is defined as

$$\mu_s = N_s \sigma_s, \tag{8}$$

where N_s is the number density of scatterers and σ_s is the scattering cross section. From equation (8), the scattering coefficient can be defined as the total cross-sectional are for scattering per unit volume [7].

In a scattering medium, there is a probability of backscattered photons. When the light is scattered a sufficient amount of times in a medium, the light propagation can be represented by the reduced scattering. The reduced scattering coefficient is defined as

$$\mu_s' = \mu_s \cdot (1 - g), \tag{9}$$

where $g = \overline{cos(\theta)}$ is the anisotropy factor, which is the average cosine of the scattering angle θ [7]. g has a value between -1 and 1, where a value of zero indicates isotropic scattering and a value close to unity indicates dominantly forward scattering [7]. The anisotropy factor for most biological tissues is around 0.9 [7]. If normal scattering, by the original scattering coefficient μ_s, can be represented by a series of scattering events, reduced scattering can be represented by, on a macroscopic scale, one scattering event.

There are multiple scatterers in biologial tissue. Some of the most important are collagen, myelin, cell membranes and cell organelles.

Scattering of light by a spherical particle can be modeled exactly by the Mie[1] theory. The Mie theory assumes homogeneous spherical scattering particles of isotropic material, and utilizes two properties; the relative refractive index between the scattering particle and the medium, $n_r = n_s/n_m$ (where the subscript s refers to the scattering particle and the subscript m to the medium), and the size parameter $x = 2\pi r/(\lambda/n_m)$ (where r is the radius of the scattering particle). The incident light is assumed to be a plane monochromatic wave. Mie scattering theory is directly derived from Maxwell's equations, and the solution takes the form of an analytical infinite series. The wavelength dependency for the Mie theory can be expressed as [7]

$$y = n_{rel}x = \frac{2\pi n_s a}{\lambda}, \tag{10}$$

where $x = ka$ is the size parameter, a is the radius of the scattering particle, $n_{rel} = n_s/n_b$ is the relative refractive index of the sphere with refractive index n_s in a background medium with refractive index n_b [7].

The Mie theory reduces to the Rayleigh[2] theory if the spherical particle is much smaller than the wavelength [7]. The Rayleigh scattering theory is valid for elastic scattering of light or electromagnetic radiation by particles much smaller than the wavelength of the light. The incident light is assumed to be a monochromatic plane wave, and scattering is caused by localized scattering centers. The scattering cross section σ_s can be calculated by the Rayleigh theory,

$$\sigma_s = \frac{a^6}{\lambda^4}, \tag{11}$$

where a is the radius of the scattering particles and λ is the wavelength of the incoming light. Equation (11) shows that scattering depends on the size of the particle and the wavelength of the light. Smaller wavelengths are much more

---

[1] Gustaf Adolf Feodor Wilhelm Ludwig Mie, 1869 - 1957, German physicist

[2] John William Strutt, 3rd Baron Rayleigh, 1842 - 1919, English physicist

effectively scattered than longer wavelengths, as long as the particles are much smaller than the wavelength when using the Rayleigh theory. The Mie theory can be used regardless of particle size, but is more difficult to calculate than the Rayleigh theory.

2.2.3 Extinction

Since both absorption and scattering are present in biological tissue, an extinction coefficient can be defined as the sum of the absorption coefficient and the scattering coefficient,

$$\mu_t = \mu_a + \mu_s, \tag{12}$$

where μ_t is the extinction coefficient, or the total interaction coefficient. For extinction, as for ideal scattering, there is a probability for backscattering, and a reduced extinction coefficient can be defines as

$$\mu_t' = \mu_a + \mu_s', \tag{13}$$

using μ_s' from equation (9) [7].

2.3 Transport of light in tissue

Photon transport in biological tissue can be modeled by the radiative transfer equation. This equation is difficult to solve, and can be approximated to a diffusion equation. However, the diffusion approximation will provide less accurate solutions than the Monte Carlo method [7].

When light is scattered in multiple events, it will lose its coherence and the polarization can be neglected. The absorption and scattering events in tissue leads to the Boltzmann photon transport equation,

$$\hat{s} \cdot \nabla L(\vec{r}, \hat{s}) = \mu_s \cdot \int_{4\pi} L(\vec{r}, \hat{s}') p(\hat{s}' \cdot \hat{s})\, d\Omega' - \mu_t L(\vec{r}, \hat{s}) + S(\vec{r}, \hat{s}), \tag{14}$$

where the radiance L is defined as the spectral radiance integrated over a narrow frequency range $[\nu, \nu + \Delta\nu]$:

$$L(\vec{r}, \hat{s}) = L_\nu(\vec{r}, \hat{s})\Delta\nu, \tag{15}$$

where the spectral radiance L_ν is the energy flow per unit normal area per unit solid angle per unit temporal frequency bandwidth, and the normal area is perpendicular to the flow direction. $\vec{r}$ is the position and $\hat{s}$ is unit direction vector [7]. The phase function p in equation (14) describes the probability of scattering in direction $\hat{s}'$ when the original direction of the photon was $\hat{s}$. The last term S is the source term. The derivation of (14) can be found in [7].

The left-hand side of equation (14) describes loss due to divergence of the light beam. The integration of L and p on the right-hand side is the main scattering term, where photons are scattered according to the phase function. μ_t is the extinction coefficient. S denotes the source term, where new photons enter the position $\vec{r}$ in the direction $\hat{s}$.

The phase function is usually the Henyey-Greenstein phase function,

$$p(\hat{s}' \cdot \hat{s}) = p(cos\theta) = \frac{1-g^2}{2(1+g^2-2gcos\theta)^{\frac{3}{2}}}, \tag{16}$$

where θ is the angle between the original photon direction and the scattered photon direction, and g is the anisotrophy factor, which is defined as

$$g = \int cos\theta p(cos\theta) d(cos\theta). \tag{17}$$

The anisotrophy factor is the average cosine of the scattering angle.

The Boltzmann equation, (14), can be solved using the Monte Carlo method, or by diffusion theory.

2.3.1 Diffusion theory

From the definition of the fluence rate ϕ and the flux $\vec{j}$ [20], and integrating the Boltzmann equation (14) over all solid angles, a continuity equation can be obtained:

$$\nabla\vec{j}(\vec{r}) = -\mu_a\phi(\vec{r}) + q(\vec{r}), \tag{18}$$

where the integrated L and $L\vec{s}$ have been replaced with respectively the fluence rate ϕ and the diffuse photon flux vector $\vec{j}$, and the integrated source function S has been replaced by q.

If the scattering is assumed to be much stronger than absorption, then the radiance can be expressed as an isotropic fluence rate ϕ plus a small directional flux $\vec{j}$. Equation (14) is then reduced to a diffusion equation [20]. By substituting a diffusion approximation of L [21] into (14) and multiplying by $\hat{s}$ and integrating over all solid angles, gives [20]

$$\vec{j}(\vec{r}) = -D\nabla\phi(\vec{r},t), \tag{19}$$

where D is the photon-diffusion coefficient. Combining equation (18) and (19) gives an expression for the fluence rate without the flux,

$$\nabla^2\phi - \frac{\phi}{\delta^2} = -\frac{q}{D}, \tag{20}$$

where the optical penetration depth δ is defined as

$$\delta = \sqrt{\frac{D}{\mu_a}}. \tag{21}$$

Equation (20) can be applied for each layer in the skin, with depth-varying source function. For a more detailed introduction to diffusion theory, see [1].

2.3.2 Monte Carlo simulation

Monte Carlo (MC) simulation is a method for modelling light propagation, which is used within, amongst others, medical dosimetry [22], metereology [23] and probability theory [24].

The idea behind using MC in photon migration modelling in biological tissue is to regard the photon as a particle, and give each photon a random pathlength and direction of propagation based on the probability distribution defined by μ_a, μ_s, $p(\theta)$ and the refractive index of the tissue. By tracking a sufficient number of photons, physical quantities such as diffuse reflectance can be estimated [7].

By the Monte Carlo method, an ensemble of biological tissues is modeled for the averaged characteristics of photon transport [7]. This ensemble consists of all the instances of the tissues that are microscopically different but macroscopically identical [7]. For the method to be statistically valid, a large number of photons have to be tracked, which is time consuming. However, multiple physical quantities can be simultanously estimated [7]. Some of these include relative specific absorption, relative fluence, relative diffuse reflectance and relative diffuse transmittance, all of which are relative to the incident energy [7].

A Monte Carlo-implementation of (14) will involve tracking each photon packet and accounting for absorption and scattering losses as according to the mechanisms described by (14) using probabilistic methods [25]. Figure 7 shows a flowchart for the Monte Carlo package MCML [7]. s denotes the stepsize. This is sampled from a random distribution which describes the probability of encountering an absorption or scattering event. If the particle hit the boundary between the two layers, the reflection and trasmission will be described by Fresnel's equations. If not, they are moved according to step size. The weight of the photon packet is reduced as according to absorption and back-scattering determined by μ_t. The new scattering direction is then determined by sampling a random variable from (16) [25]. Photons with too small weight will be eliminated, but the Russian roulette will keep some of them alive to ensure energy conservation.

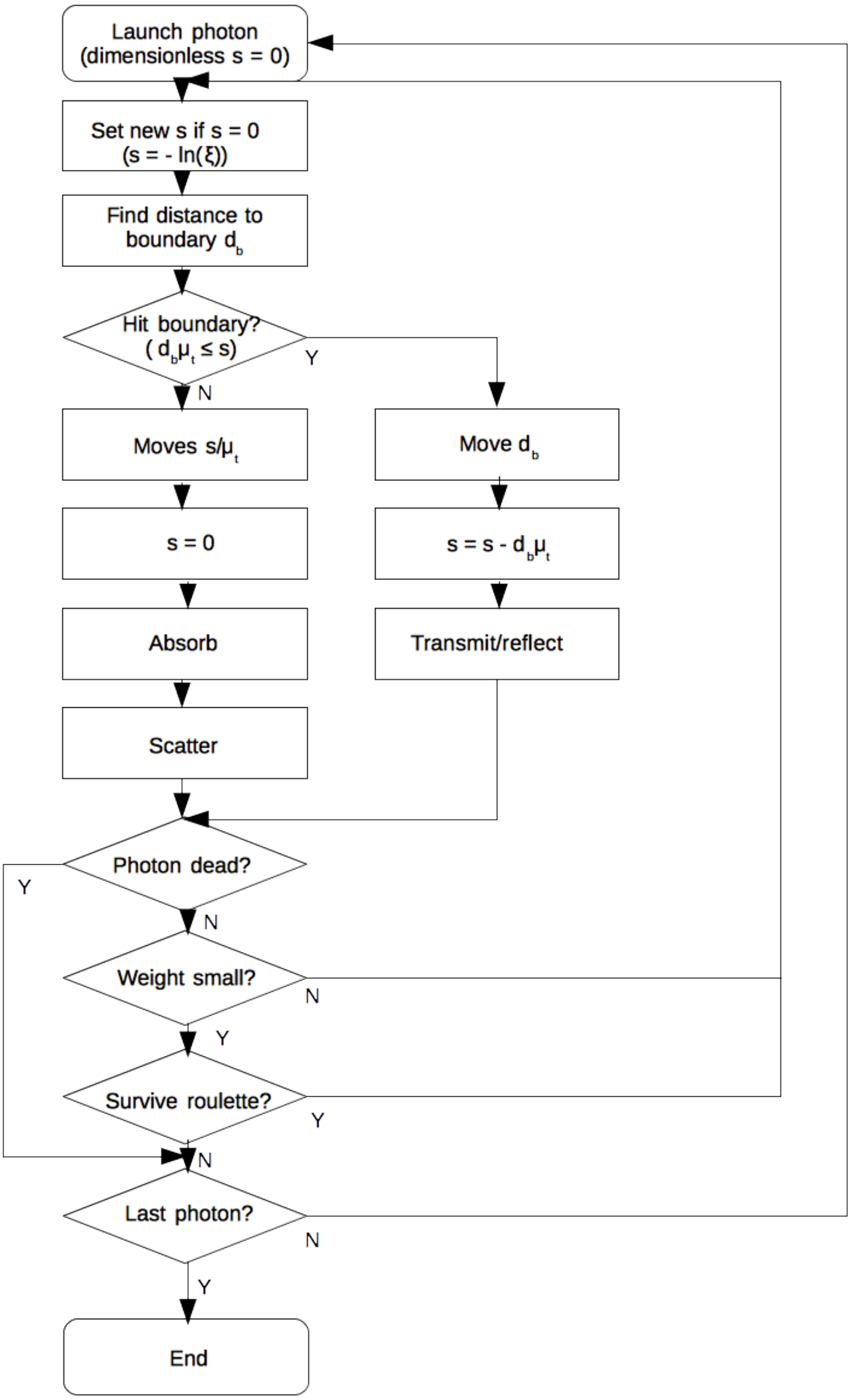

Figure 7: Program flow in MCML, reproduced from [7].

2.4 Hyperspectral imaging

This chapter contains an introduction to hyperspectral imaging and the concept behind using hyperspectral imaging for medical applications.

Hyperspectral imaging is an imaging technique that combines spectroscopy and imaging and allows the recording of an emission spectrum limited by the detector used, for every pixel on the entire image. Hyperspectral imaging combines both spatial and spectral information. The data from hyperspectral imaging is called a hypercube, containing information in two spatial directions and one spectral direction. Hyperspectral data are images of the surface radiance [4]. This radiance can be converted to reflectance data from the full spectrum. The concept behind hyperspectral imaging is that a two dimensional image is recorded at discrete emission wavelength intervals, where each image contains spatial and spectroscopic (intensity) information at a given wavelength [3].

There are numerous possible applications for hyperspectral imaging, for spectroscopic analysis, image analysis and tissue optics. From spectroscopic analysis, it is possible to extract information about, for example, blood oxygenation, pigmentation in the skin, erythema and edema. From image analysis, there are for example spectral differences, classification, information about structure and locating hidden objects. Tissue optics can give information about the propagation of light in turbid media and optical properties by applying invers models as the diffusion model and Monte Carlo.

The quality of the data from hyperspectral imaging, where the amount of photons available per spectral band is limited, relies on the signal-to-noise ratio (SNR) that the system can provide. The overall SNR is determined by the intensity of the incoming light from a reflection-, transmission- or fluorescence process, the overall effect of noise from sources like photon noise, dark current noise and readout noise, and also system losses that originates from optical transmission, absorption and quantum efficiency [26]. Similarly, a combination of some of these factors determines the total sensitivity per spectral band of the system [26].

2.5 Noise removal

Noise removal can either be done by averaging over the neighboring pixels, or by a minimal noise fraction (MNF) transform. A MNF transform will guarantee that the principal componens in the image will be ranged from the least noisy to the most noisy, measured by a signal-to-noise (SNR) ratio. Firstly, a forward MNF rotation is done. The MNF transform is a linear transformation which is essentially two cascaded Principal Components Analysis (PCA) transformations. This forward transform allows to eliminate the bands that contains mostly noise. The inverse transform is then done using only the selected bands that contain useful information. This drastically reduces the amount of data that has to be processed further, and the result is a noise reduced image without any loss of spatial resolution.

Assuming the hyperspectral image consist of n bands with spatial coordinates x and y, the data set for the image can then be expressed as [27]

$$A_i(x,y), i = 1,2,...,n \tag{22}$$

A_i can then be divided into one component for the signal and one for the noise, respectively $S(x,y)$ and $N(x,y)$, under the restricten that the signal and the noise are orthogonal. The data set thus consist of [27]

$$A(x,y) = S(x,y) + N(x,y). \tag{23}$$

The signal-to-noise ratio for the i-th band is defined as [27]

$$\frac{Var\{S_i(x,y)\}}{Var\{N_i(x,y)\}}, \tag{24}$$

the ratio of the signal variance and the noise variance. The maximum noise fraction transformation are then defined as the linear transformations [27]

$$Y_i(x,y) = a_i^T A(x,y), i = 1,...,p. \tag{25}$$

The signal-to-noise eventually becomes [27]

$$\frac{Var\{a_i^T N(x,y)\}}{Var\{a_i^T A(x,y)\}} = \frac{a_i^T \Sigma_N a_i}{a_i^T \Sigma a_i}, \tag{26}$$

and the vectors a_i are eigenvectors to the real, symmetrick, generalized eigenproblem [27]

$$det\{\Sigma_N - \eta\Sigma\} = 0. \tag{27}$$

Then the signal-to-noise ratio for $Y_i(x,y)$ is given by [27]

$$SNR = \frac{1}{\eta_i} - 1, \tag{28}$$

where η_i is the eigenvalue of Σ_N with respect to Σ. For the invers transform, $Y(x,y)$ is multiplicated by the invers of a^T [27],

$$A(x,y) = (a^T)^{-1} Y(x,y). \tag{29}$$

In summary, the first transformation decorrelates and rescales the noise in the data. This results in transformed data in which the noise has unit variance and no band to band correlations. The second transformation is a standard PCA of the noise-whitened data.

2.6 Spectral angle mapper SAM

SAM is a method for classification of an image spectrum. SAM compares an unknown pixel spectrum to a reference spectrum.

In a SAM analysis, the spectrums are viewed as n-dimensional vectors, where n is the number of spectral bands. Each vector has a certain length and direction. The length of the vector is determined by the brightness of the pixel, while the direction represents the spectral information [28].

Spectral differences between pixels will affect the angle between the vectors. The angle increases with differences between the two spectrums, and the angle can have values between 0 and $\pi/2$ [28]. Equation (30) shows how the spectral angle θ is calculated [28],

$$\theta = \cos^{-1}\left(\frac{\sum_{i=1}^{n} t_i r_i}{\sqrt{\sum_{i=1}^{n} {t_i}^2 \sum_{i=1}^{n} {r_i}^2}}\right), \tag{30}$$

where n is the number of spectral bands, t is the reflectance of the actual spectrum and r is the reflectance of the reference spectrum [28]. Pixels are classified by calculating the spectral angles between the reflectance spectrum of the target spectra and the reference spectra [28]. Each pixel will be assigned to the class according to the lowest spectral angle value [28]. Pixels with an angle larger than a predefined boundary will be unclassified.

3 Methods of analysis

3.1 Preparation

This chapter includes a description of the preparation of the wound models and the experimental setup.

3.1.1 Preparation of the samples

The skin used for the wound models, was donated human skin from plastid abdominal surgery. The surgery took place at Aleris in Trondheim, April 8 2014, and the surgeon was Ivan Pavlovic. The donor was healthy and admitted for elective abdominoplasty, and had beforehand agreed to give access to excess skin. There was no available information about age and gender of the donor. The use of the human skin is ethically approved, as it does not affect an otherwise planned surgery and follow-up postoperatively. The skin would otherwise been thrown away, but is instead useful in further research. Figure 8 shows the whole piece of skin that was donated from the surgery.

Figure 8: Donated skin piece.

The skin samples were made by Brita Pukstad, by using punch biopsies with diameters of 3 mm, 4 mm and 8 mm. The 8 mm punch biopsy was used to cut out the whole skin sample for all of the samples. The 3 mm and 4 mm punch biopsies were used to make the wound in the samples. The wound models were placed in containers with respect to the medthod that was used in the making. The skin samples were made approximately 1,5 hours after surgery. The skin was prepared by cleaning the skin to remove blood from the surface.

The wound models were made by first using the smaller punch biopsy to cut out the diameter of the wound by cutting approximately 1 mm down in the epidermis and slightly into the dermis. The skin was then lifted with either a cannula or a custom made suction device, and then cut away using a pair of scissors. The final step is then to cut out the whole wound model by using the 8 mm punch biopsy, lift the samples with a tweezer and cut them loose. The wound models were sorted into well trays of 6 well each, with nutrition medium. The medium used was Dulbecco's Modified Eagle Medium (DMEM) (Gibco, USA). 10% fetal calf serum (FCS), 50μg/ml penicillin, 50 U/ml streptomycin and glutamine were added to the DMEM. Figure 9 shows an illustration of the wound models.

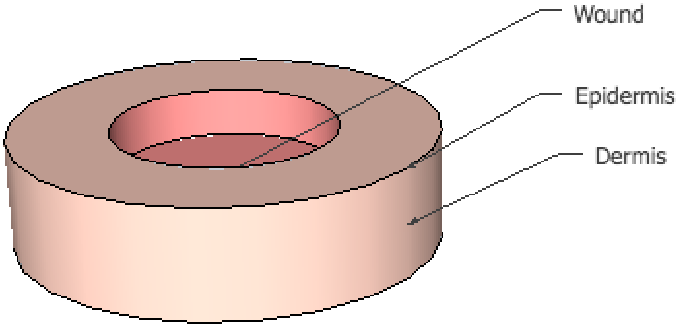

Figure 9: Illustration of the wound models.

Figure 10 shows how the samples were lifted with the cannula, and here, cut with knife. However, scissors proved to make cleaner cuts so none of the final wound models were cut with a knife. Figure 11 shows how the suction device was used to lift the wound.

When making the wound models, it is important to make them as uniform and equal to insure that they behave as similar as possible. The crucial factors in preparing the wound models are:

- Only one skin sample in each well in the well tray.

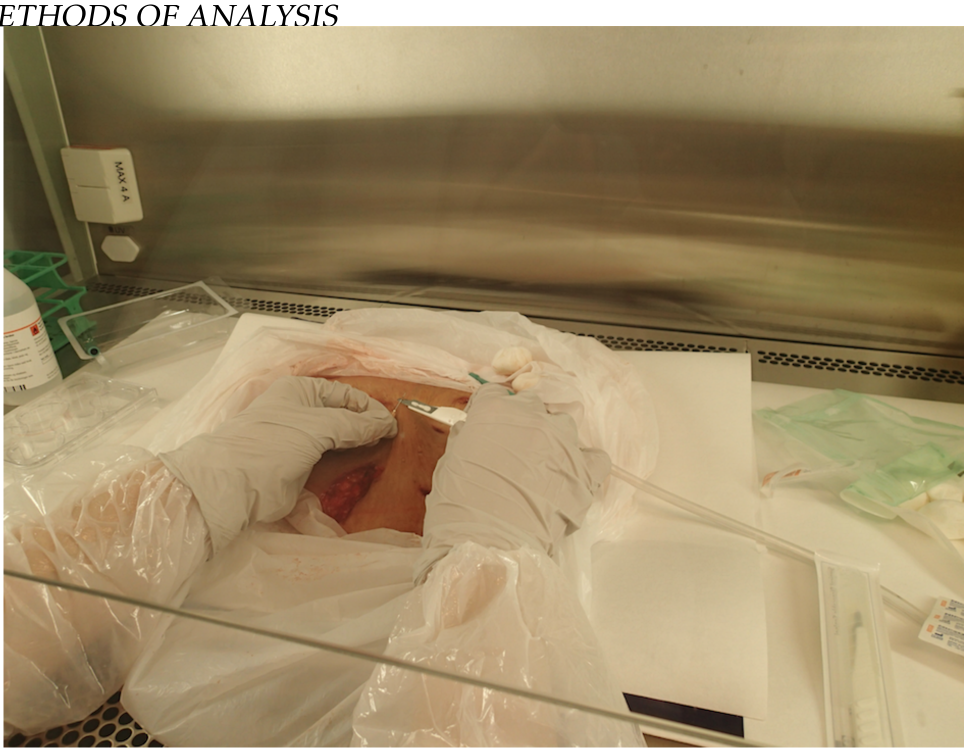

Figure 10: Sample holder insert seen from above.

- The amount of medium have to be measured and should be the same in each space.
- Wells with only medium should be included for reference.
- Skin samples without wound should be included for reference with respect to shrinking. These should be the same size as the wound models.

The well trays used in the experiment have 6 wells each. Inside each well, there was a custom made insert plate used to keep the wound models in a fixed spot, and preventing them to drown in the medium. The inserts are made of some stainless metal with holes drilled in to insure nutrition supply to the wound models. The well tray inserts were made by Tore Landsem, staff engineer at the Department of Electronics and Telecommunications at NTNU. Figure 12 shows one of the inserts from above, and Figure 13 shows the insert from the side.

There were only one wound model placed in each well in the trays. A total of three well trays were used. The trays were numered with roman numbers, I, II and III. Tray I includes wound models with 3 mm wounds lifted up with the suction device and cut with scissors. Tray II includes 3 mm wounds lifted with a cannula and cut with scissors. Tray III includes 4 mm wounds lifted with a can-

Figure 11: Sample holder insert seen from above.

nula and cut with scissors.

In between the imaging, the well trays were kept in a Forma Steri-Cycle CO_2 incubator (Thermo Scientific, Waltham, Massachusetts, USA). This cabinet incubates at 37° Celcius and with 5% CO_2.

Immediately after every imaging session, the medium was changed. The amount of medium used was 5 mL for all the wells. This provides the skin with sufficient nutrition, in addition to access to air. Lack of oxygen would prevent the keratinocytes from forming epithelial layers [29].

On April 19., it was discovered that an infection had occurred in some of the samples since the last imaging. These samples had to be removed immediately after imaging this day. After removing the infected samples, the rest of the samples and the well tray inserts were cleaned then inserted into new trays. The infected wells are the following: I-1, I-2, II-1, II-3 and III-3. Figure 14, Figure 15 and Figure 16 shows pictures of the well trays taken on April 19. Figure 17, Figure 18 and Figure 19 shows the well trays after the infected samples have been removed, the remaining cleaned and moved to new well trays.

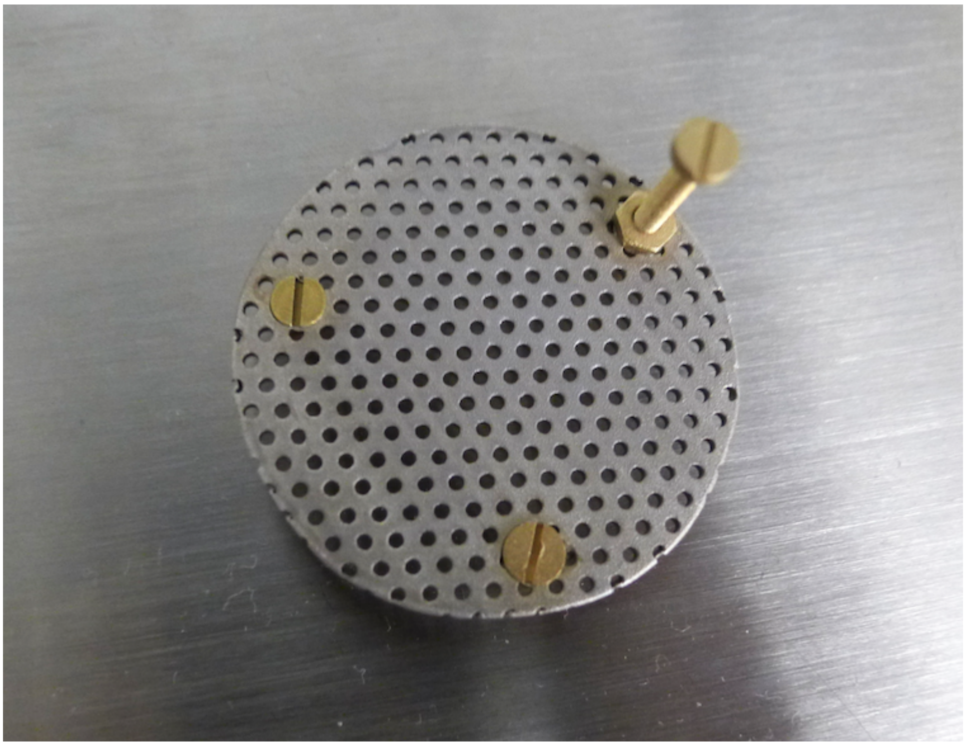

Figure 12: Sample holder insert seen from above.

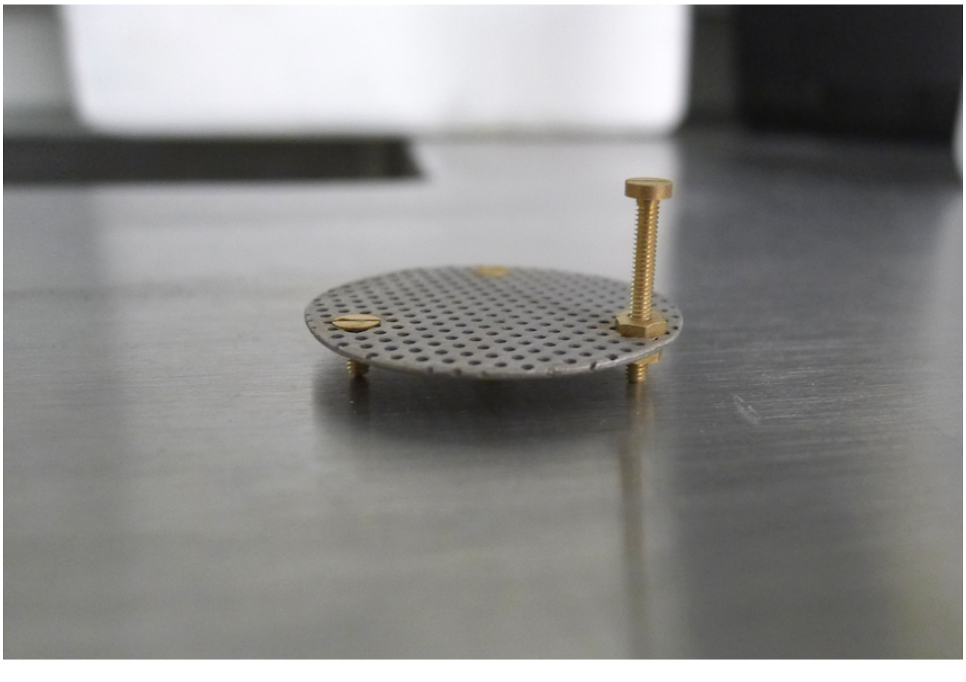

Figure 13: Sample holder insert seen from the side.

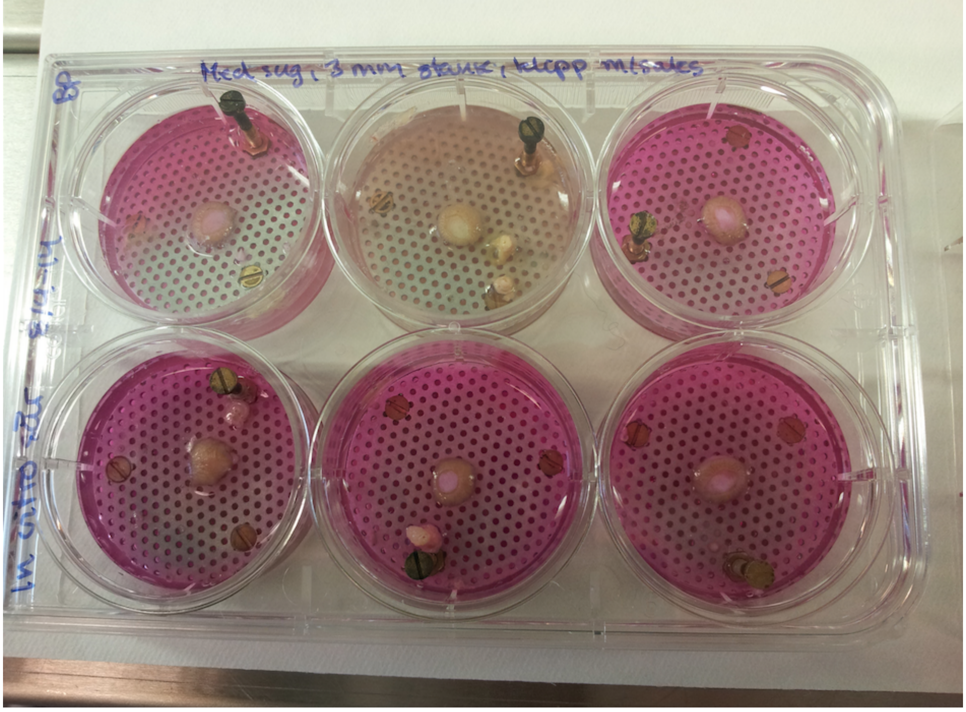

Figure 14: Well tray I with infected wound models. Photo by Brita Pukstad.

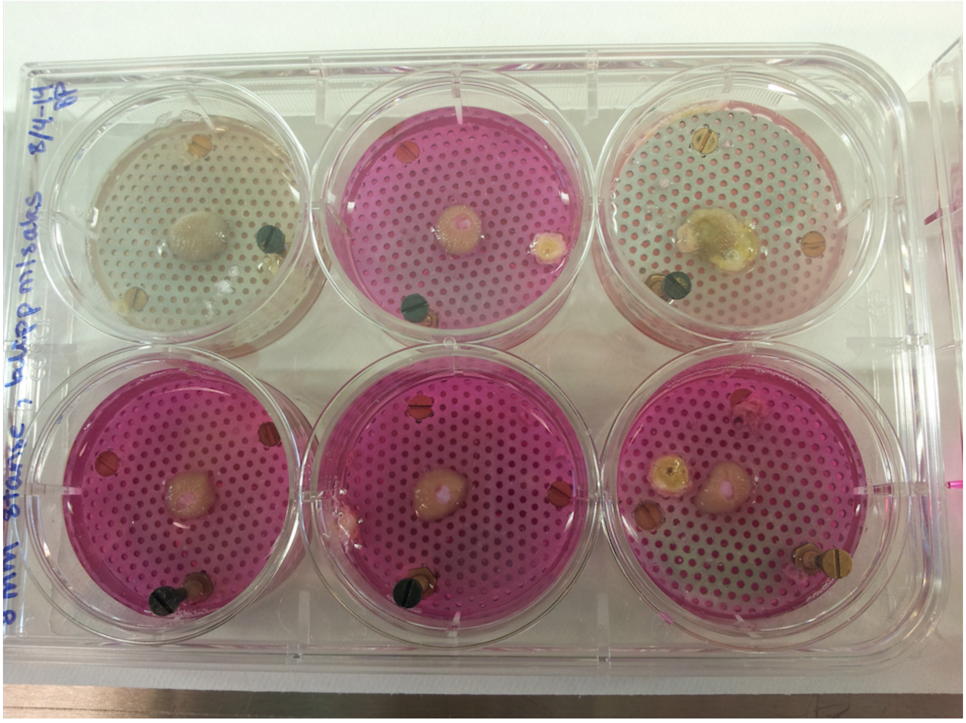

Figure 15: Well tray II with infected wound models. Photo by Brita Pukstad.

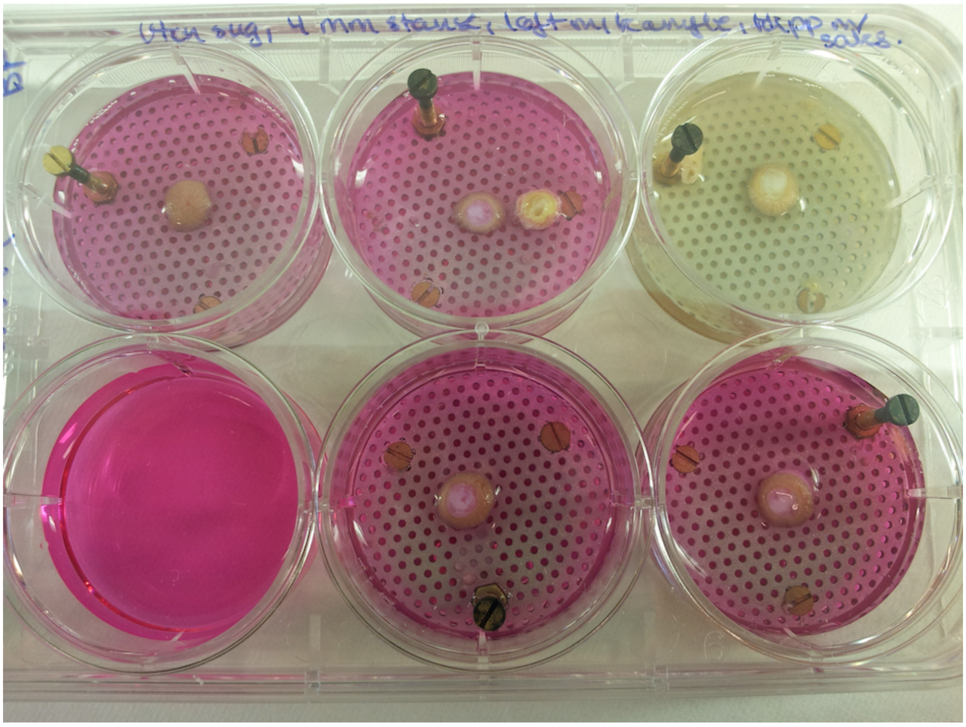

Figure 16: Well tray III with infected wound models. Photo by Brita Pukstad.

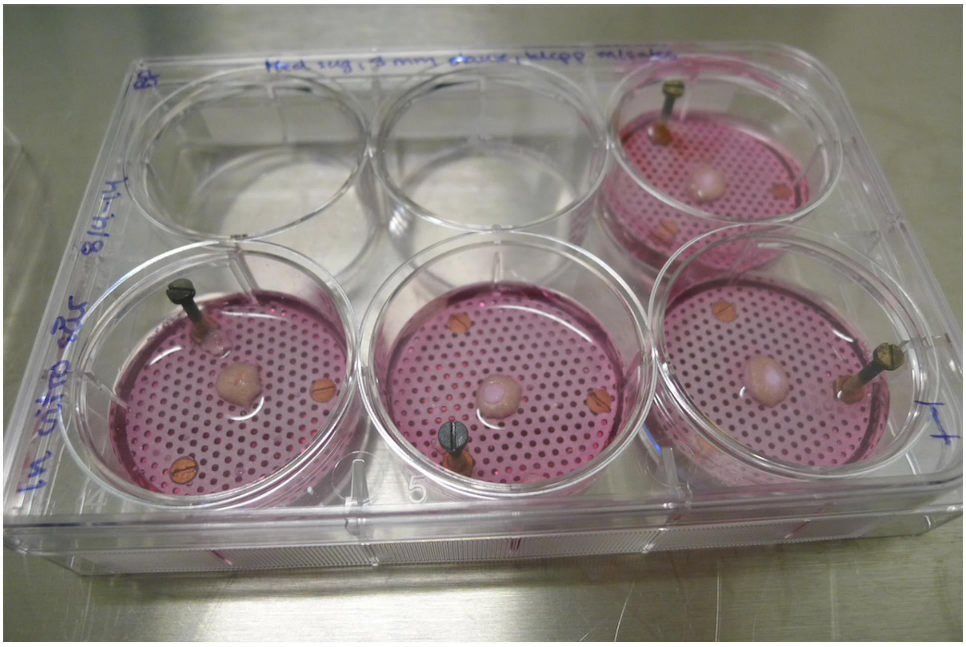

Figure 17: Well tray I without infected wound models.

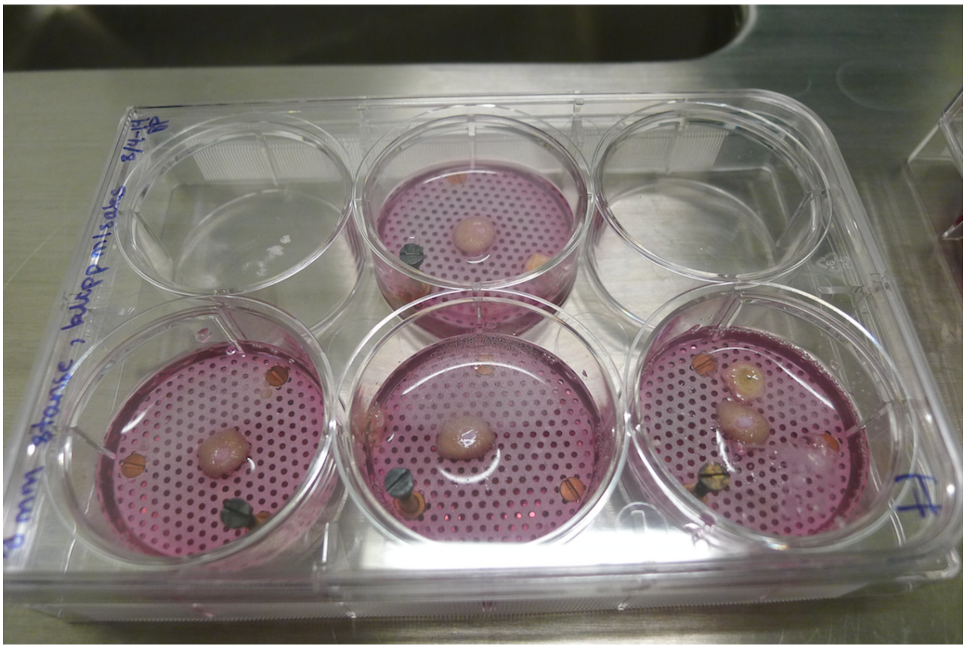

Figure 18: Well tray II without infected wound models.

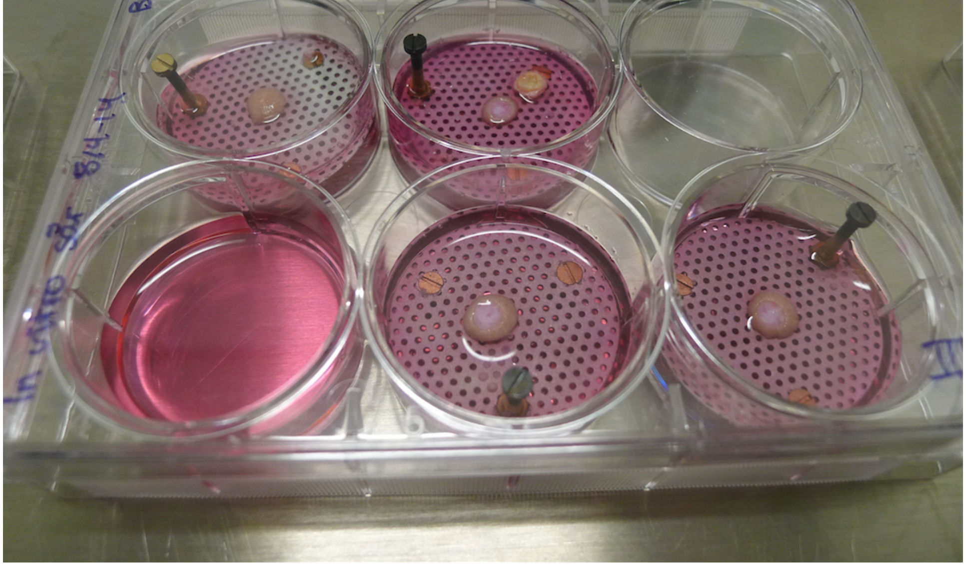

Figure 19: Well tray III without infected wound models.

3.1.2 Experimental setup

The camera is mounted on a robust rack. The camera can be moved up or down do adjust focus. There is a horizontal translation stage located under the camera, that allows the samples to be scanned by the camera. The translation stage is driven by a Standa 8SMC1-USBhF-B1-1 Stepper Motor Controller (Standa Ltd, Svitrigailos 4-39, 03222 Vilnius, Lithuania) [30]. The translation stage is controlled in the image aquisition software used. Attached to the horizontal translation stage is a custom made support plate for the well tray and a reference standard, made by Tore Landsem. This support plate provides a smooth and steady surface.

The light sources (one for white and blue light, and one for UV light) are mounted next to the camera lens, at an angle providing the highest illumination possible. Attached to the camera lens, is a polarizer. The reason for this is to avoid specular reflections in the image. Specular reflection results in saturated pixels, and saturated pixel does not contain any information.

Figure 20 shows the setup from the side. The big black box is the camera, the light source to the right of the camera is white and blue light. The custom made support plate is mounted on the translation stage, shown with the white reference standard and the well tray. The translation stage moves the tray from right to left.

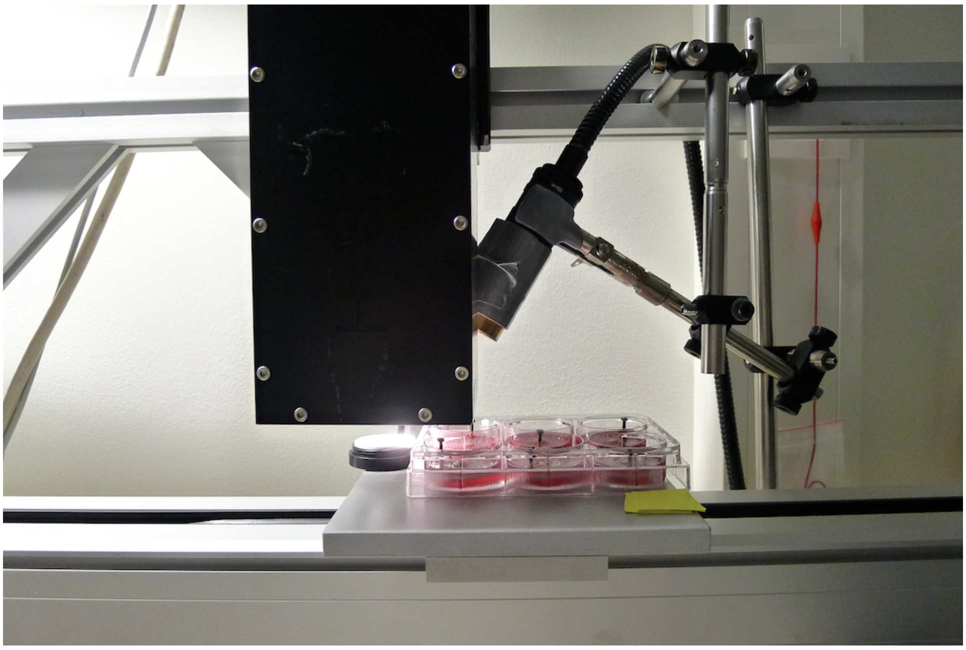

Figure 20: Imaging setup.

Figure 21 shows the arrangement of the light sources and camera lens. Here, the camera lens and a UV light source can be seen.

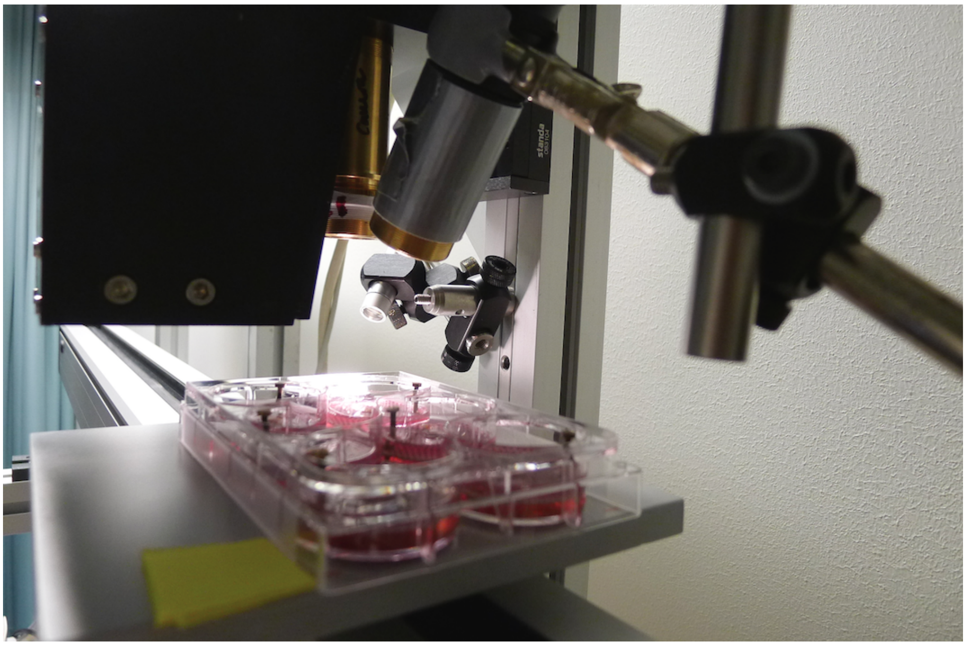

Figure 21: Imaging setup.

In Figure 22, the setup is shown from the side where the UV light source is mounted.

3.2 Hyperspectral imaging procedure

This chapter explains how the hyperspectral imaging was performed and the equipment used.

The imaging was done every second day from April 8. 2014 to April 29. 2014, resulting in a total of 12 measurements. The imaging was done in the Hyperspectral lab at St. Olavs Hospital in Trondheim. The hyperspectral camera used was the HySpex VNIR-1600 developed and manufactured by Norsk Elektro Optikk [31]. This is a line-scanning camera that records lines of 1600 pixels and 160 bands, or wavelengths. The specifications for the HySpex VNIR-1600 are given in table 2 [32].

Inside the camera, the light from the scene is focused by an aspheric mirror onto a slit that defines an instantaneous field of view [26]. Behind the slit, a second

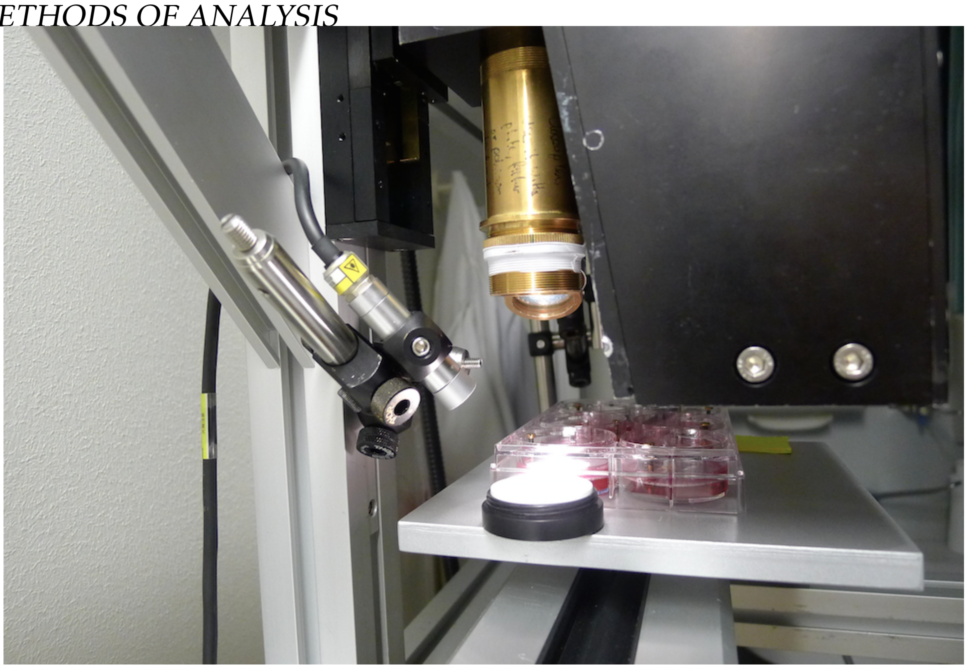

Figure 22: Sample holder insert seen from the side.

Table 2: Specifications for HySpex VNIR-1600

Detector	Si CCD 1600 1200
Spectral range	0,4 - 1,0 μm
Spatial pixels	1600
FOV	17 degrees
Pixel FOV across/along track	0,18 mrad/0,36 mrad
Spectral sampling	3,7 nm
Digitalization	12 bit
Max frame rate	135 fps

aspheric mirror collimates the light onto a transmission grating for spectral dispersion in a plane perpendicular to the slit [26]. An objective lens focuses the light onto a two-dimensional detector array [26]. Figure 23 shows the optical layout of the camera.

The camera uses a custon software provided by NEO, called HySpex Ground [31]. This software aquires and saves the images as a .hyspex file, with a corresponding header file that contains information about the image. The images were initially inspected using ENVI [33] and imported into Matlab [34] for analysis. The hyspex-images can be converted to radiance data using the software HySpex RAD [31].

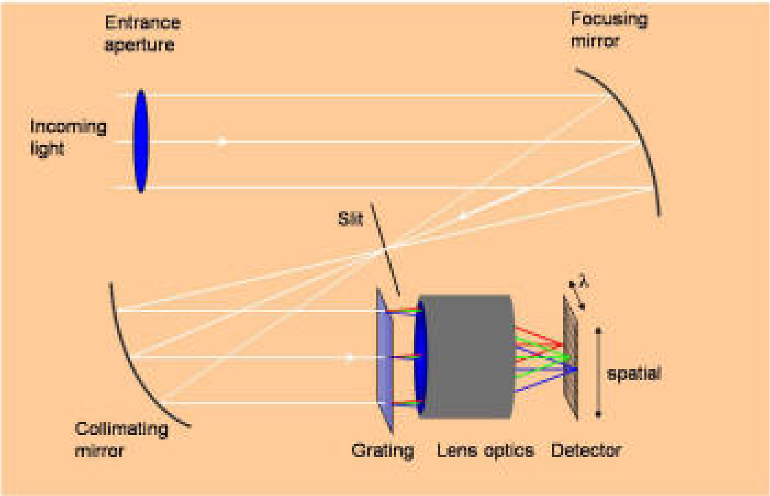

Figure 23: Schematic of the optical layout of the HySpex VNIR-1600 hyperspectral camera [31].

There is a reflectance standard included in all the images. This standard is a Spectralon Diffuse Reflectance Standard SRS-99-010 (Labsphere Inc., Reflectance Calibration Laboratory, North Sutton, USA) [35]. The specifications for the reflectance standard can be found in table 3.

Table 3: Specifications for diffuse reflectance standard

Reflectance factor	99 %
Reflective area (inches)	1,25 D
Dimensions (inches)	1,50 D x 0,55 H

The imaging was done using white light, blue light (440 nm) and UV light. The light source for white and blue light was a Schott-Fostec DCR II (SCHOTT MORITEX Corporation, 3-13-45 Senzui, Asaka-shi, 351-0024 Saitama, Japan). The blue light was achieved by attaching a blue filter to the light source. The blue filter was a Asahi Spectra XHQA440 High Transmission Bandpass Filter (Asahi Spectra USA, Inc., 23505 Crenshaw Boulevard, Suite 229 Torrance, CA 90505, USA) [36].

For the white light imaging, 80 % of the total light power was used. This was found to be the level where there was close to zero specular reflections. The integration time used for white light imaging was 7500 ms. For blue light, 100 %

of the available power was used, and an integration time of 50000 ms. White and blue light imaging was done this exact way for all the well trays and all the imaging sessions.

UV imaging was done with two different integration times, one for two of the trays, and one for the last tray. This was done to insure at least some of the samples were exposed to less UV radiation. The longest integration time of 50000 ms was used for tray I and III, and the shorter integration time of 10000 ms was used for tray II.

The blue light av UV images will not be presented in this thesis, but the imaging was done using these light sources as well, as the process of preparing and taking care of the wound models is a time consuming process and the access to available skin can sometimes be limited. By doing imaging with all three light sources, the blue light and UV images will thus be ready for future analysis.

3.3 Analysis of data

This chapter presents the methods of analysis of the hyperspectral images.

3.3.1 White light images

White light analysis was done with Matlab. The images were imported into Matlab and analysed by plotting reflectance spectrums of the wound, the intact skin and the wound edge. Before the images was analysed, they were converted to radiance using the HySpex RAD.

For each image, there is a corresponding header file. This header file contains information such as

- The number of lines and samples, the spatial dimensionality of the image.
- The number of bands, the spectral dimensionality of the image.
- Data type, header offset, interleave and byte order. Data needed to load the binary data with Matlab.

This header file was first imported into Matlab using the script readHyperHeader, which can be found in Appendix A.1. The image itself can then be imported using the script getHSI, from Appendix A.2, using the data from the header file.

To view the image, the matlab tool imtool() was used.

After importing the image, the sample and white standard were located, and saved as individual images in Matlab using the code in Appendix A.2. Each individual sample was then converted to reflectance data, using the script in Appendix A.3. To eliminate noise from the data, the images can be transformed using the minimal noise fraction (MNF). This is done by first applying a forward MNF transform, using the script in Appendix A.4, and then an inverse MNF transform, using the script in Appendix A.5. The individual samples were then saved as a data file for further analysis. This was done because of limited storage space, as the .hyspex-files created in this hyperspectral imaging session are typically of 5 GB or larger.

In the forward MNF transform, the number of neighbour points included in noise matrix estimation were 2, and saturation was set to 0. In the inverse MNF transform, the number of included MNF vectors was set to 5.

Using the inverse transformed image, an RGB image of the sample was created, using the Matlab code in Appendix A.6. This RGB image was used to identify and distinguish between the intact skin, the wound and the wound edge. The code in Appendix A.7 was then used to create arrays with the average reflection from the different classes in the sample. The average reflection was then plotted against the wavelength, comparing both the different classes for each sample, and the development over time. This was done using the script in Appendix A.8.

The spectral angle mapper (SAM) analysis was done using reference spectrums from day 4, the third day of measurements. The code for the SAM analysis can be found in Appendix A.9 and Appendix A.10. In A.10, black and white images from the SAM classification were plotted for each class, and then combined to see how the whole sample was classified and to give an idea of how much of the sample was classified as skin, wound or wound edge. The number of pixels classified as skin, wound and wound edge were summed.

The reflectance spectrums were also normalized at an appropriate wavelength using the script from Appendix A.11, and plotted versus the wavelength. The normalization was done by creating a variable for the spectrum at the chosen wavelength, and then dividing the whole spectrum by this value. Most of the spectrums were normalized at band 105, which corresponds to a wavelength of 788 nm. Those not normalized at 788 nm were normalized close to this wavelength, depending on the shape of the spectrums.

4 Results and discussion

In this chapter, the most significan results will be presented and discussed. This includes original images, reflection spectrums from the different classes and comparison of these, classification results and statistical analysis.

4.1 Experimental setup

By building the setup and mounting the camera, the light sources and the placement of the samples, there were some important features that had to be optimized.

In the previous experiment, executed in fall 2013 [1], the camera was mounted on the horizontal translation stage. This time, the horizontal translation stage was placed so that the well tray and the white standard were the moving parts. This was done to better position the light sources. As light is a limiting factor in this type of hyperspectral imaging, the orientation of the light source with respect to both light intensity and polarization is important.

The well tray was placed on a support plate made of sandblasted metal. The sandblasting provided a matte surface, which is good for avoiding unnecessary saturation in the images due to reflections from the light sources. Even though the support plate provided the necessary support for the well tray, there was a minor problem where the vibration from the translation stage made the well tray and reflectance standard moved slightly on the support plate, and there were some occations where the reflectance standard fell off the support plate as the support plate was not long enough to hold both the well tray and the reflectance standard.

Another important improvement done in this exsperiment was the use of the well tray inserts to prevent the samples from moving around in the medium and from drowning. The samples were exposed to a lot of movement, as they had to be carried from the lab were the incubator was located and the hyperspectral imaging lab. The medium was changed in the same lab as the incubator was located.

4.2 Sample health

As mention in the section about preparing the samples, the wells I-1, I-2, II-1, II-3 and III-3 got infected between imaging on April 17 and April 19. Unfortunately, the source of this infection is not yet known. All the wounds, both healthy and infected were sent to histology, but the results are at this point not ready. As a result of this infection, all of the infected samples had to be removed to avoid contamination to the other wound models, and thus there are no recorded images of the infected samples after day 10, April 19.

A reason for doing imaging as often as every second day is not only to be able to closely follow the reepithelializing process, but also to be able to prevent a possible infection from spreading to all the wells. This proved to be necessary, as removing the infected samples and cleaning all the remaining samples and well tray inserts prevented the infection from spreading to the rest of the samples.

4.3 White light images

Figure 24 shows the calibrated reflectance of the reflectance reference standard used to convert spectrums to reflectance.

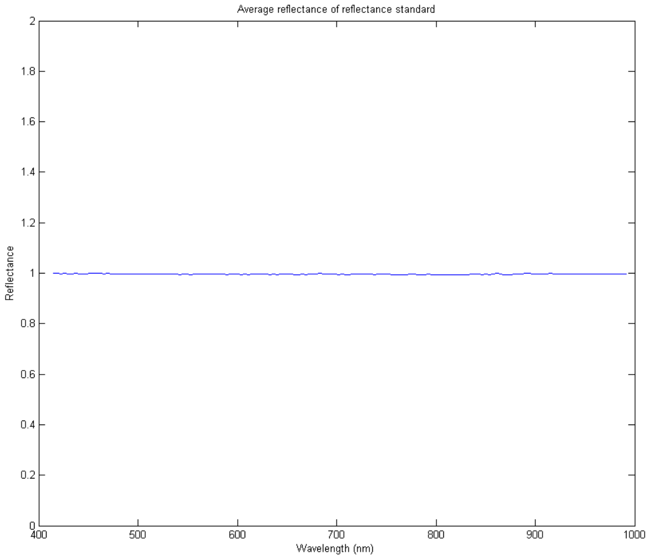

Figure 24: Average reflectance of white reference standard.

4.3.1 RGB images of wound models

In this section, a collection of RGB images of the samples will be presented. These images were created using code in Appendix A.6. The images have been edited using Gimp [37], where brightness, contrast and color curves were adjusted to brighten the image. Figure 25 show an RGB image of wound model I-1-A with arrows indicating where the intact skin, wound and wound edge are located.

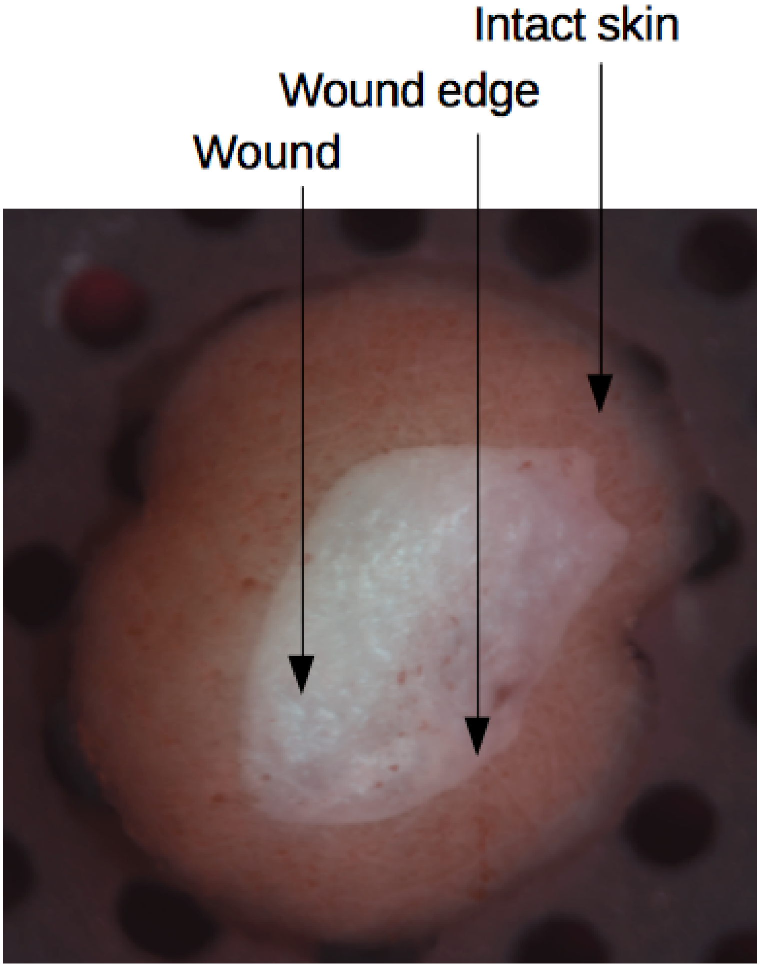

Figure 25: RGB image of I-1-A on day 1

Figure 26 shows an RGB image of I-4-A, which is a sample without a wound. The skin used for these wound models had quite a few stretchmarkes, which is quite visible in Figure 26.

Another sample without wound can be seen in Figure 27, which shows II-1-A. This image is from day 2, as the samples in tray II were made after imaging of

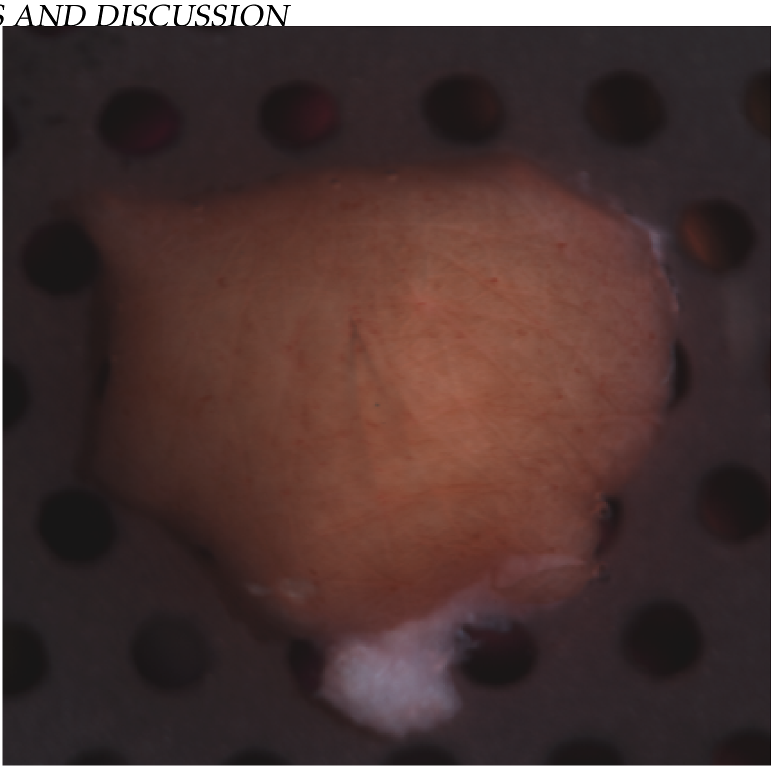

Figure 26: RGB image of I-4-A on day 1

tray I and III, and were first imaged on the second day.

On the second day of imaging, it was discovered that the well tray inserts provided favorable conditions for cell growth, and in Figure 28, RGB image of II-3-A, some of these new cells can be seen in the bottom left corner.

Figure 29 shows an RGB image of wound model III-5-A from day 1. The rest of the RGB images from samples presented here can be found in Appendix A.12.

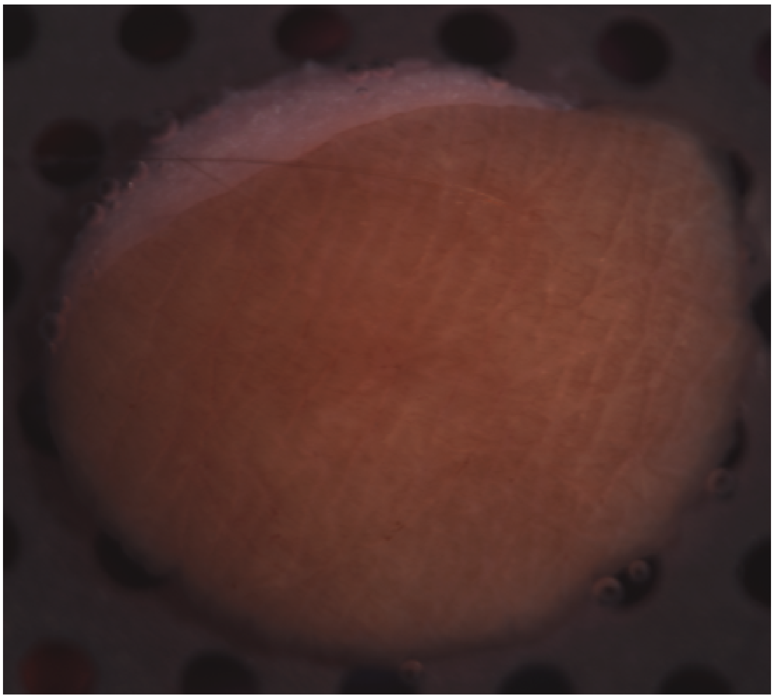

Figure 27: RGB image of II-1-A on day 2

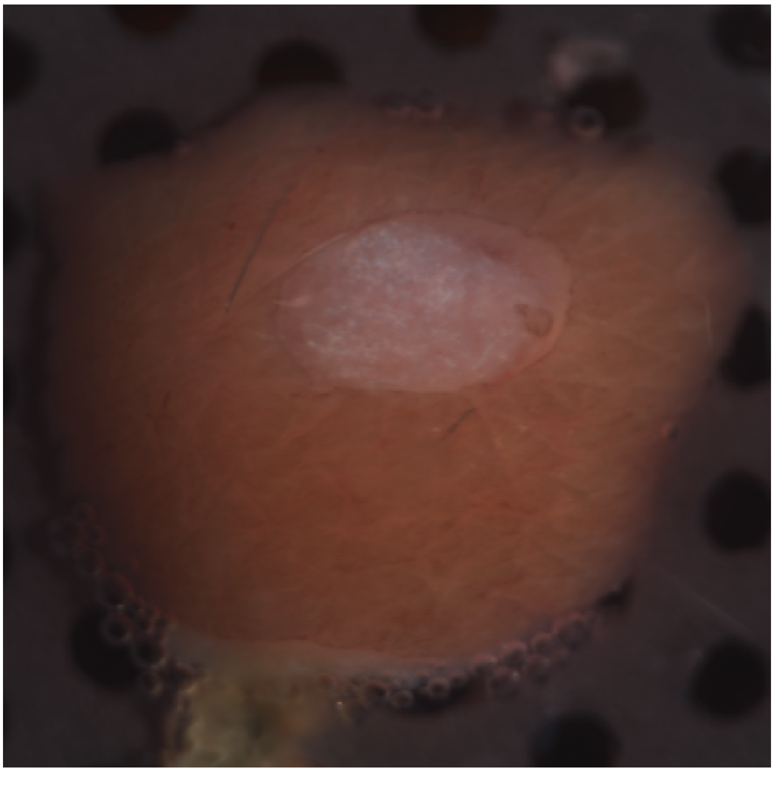

Figure 28: RGB image of II-3-A on day 2

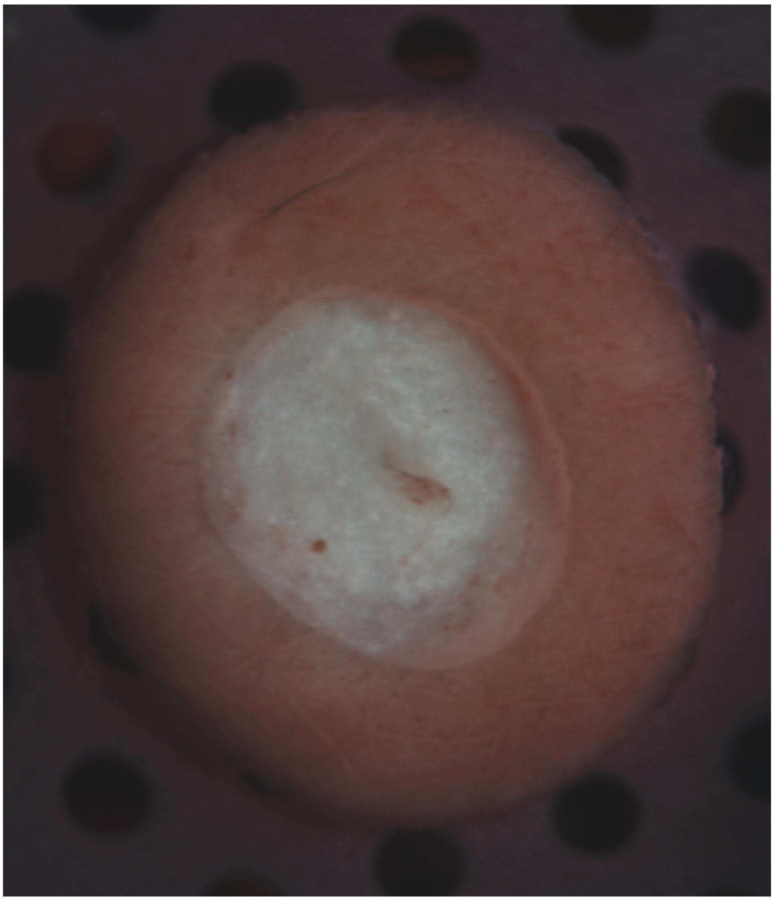

Figure 29: RGB image of III-5-A on day 1

4.3.2 Reflectance spectrums

This section will present reflectance spectrums from the wound models.

There is no data from the 7. measurement of I-4-A, I-5-A and I-6-A due to vibration that moved the reflectance standard out of the detection area, and the images could thus not be calibrated. The reflectance spectrums not presented here can be found in Appendix A.13 The imaging was done with light settings purposely chosen to avoid specular reflections, and visually it was not possible to find any specular reflections in any of the images. However, there might still be some saturated pixels, and these will impact the reflectance if they are included in the chosen regions. Due to the wound edge being very small, it is hard to accurately chose the correct region, hence the results may be affected and give misleading values.. RGB images provides better conditions than a black and white image, but it is still challenging to indentify the wound edge.

In Figure 30, the average reflectance of the intact skin, wound and wound edge for I-1-A is plotted against the wavelength.

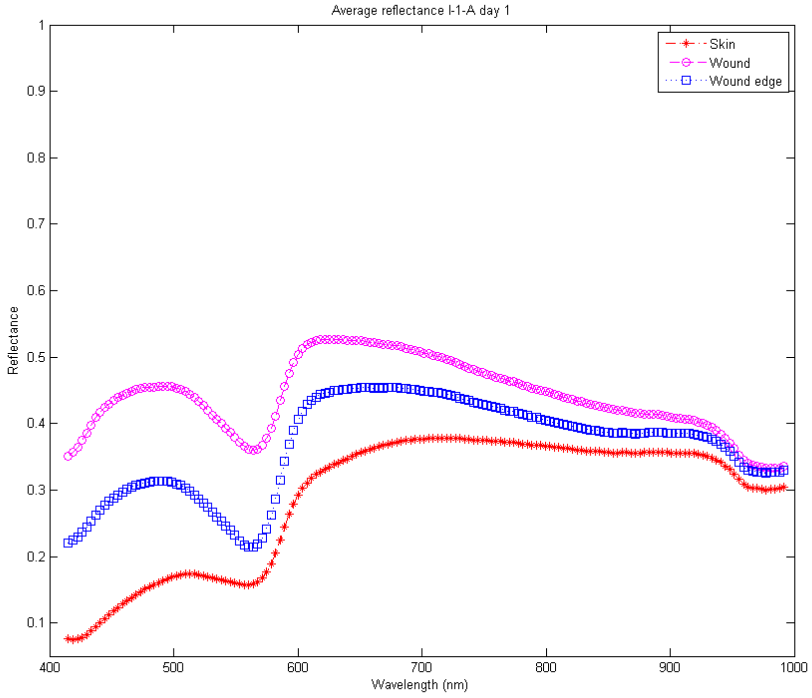

Figure 30: Average reflectance spectrum of skin, wound and wound edge for I-1-A from day 1

Figure 31 shows the reflectance for the same wound model, at day 8, the measurement before the wound model got infected. For I-1-A, the skin has the lowest reflectance, and the wound has the highest reflectance. The most distinct change between day 1 and day 8 is that the reflectance of the wound has some change in shape, and the reflectance of the skin and wound edge are more similar from 750 nm to the end of the spectrum.

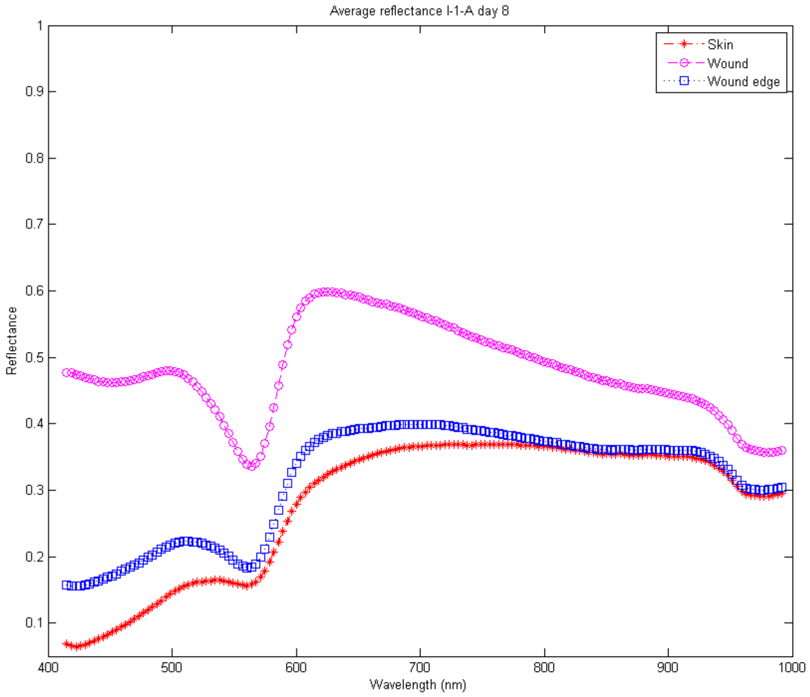

Figure 31: Average reflectance spectrum of skin, wound and wound edge for I-1-A from day 8

Figure 32 shows the average reflectance of the intact skin, the wound and the wound edge of III-5-A on day 1, Figure 33 shows III-5-A on day 8, Figure 34 shows III-5-A on day 16 and Figure 35 shows III-5-A on day 22.

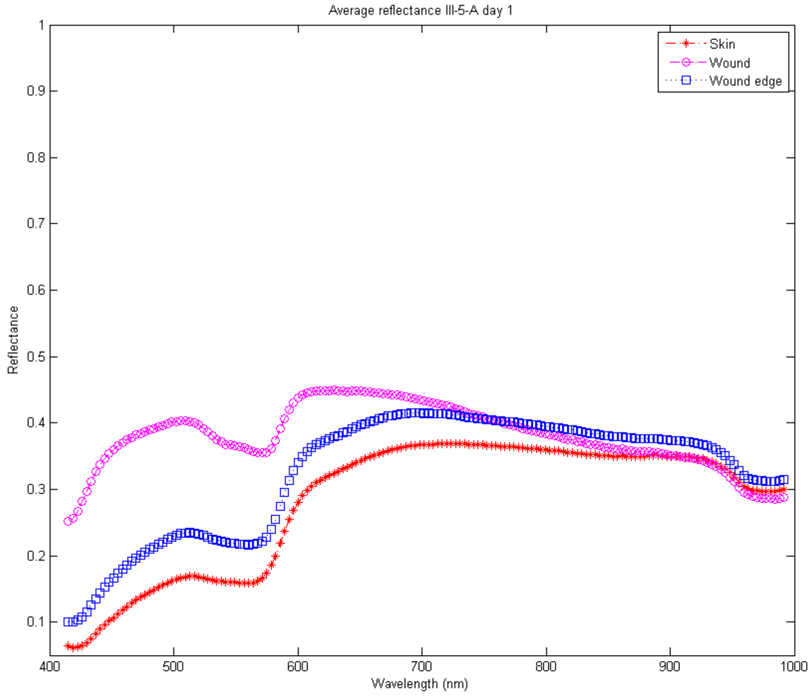

Figure 32: Average reflectance spectrum of skin, wound and wound edge for III-5-A from day 1

As III-5-A did not get infected, reflectance spectrums from the whole imaging period can be plotted. The reflectance of all classes do not change significantly througout the period, and from day 8 the reflectance of the skin is always the lowest, and the reflectance of the wound is always the highest. However on the first day, the reflectance of the wound is lower than the reflectance of the wound edge from 750 nm. This same behaviour can be found in III-2-A and II-2-A (see Appendix A.13).

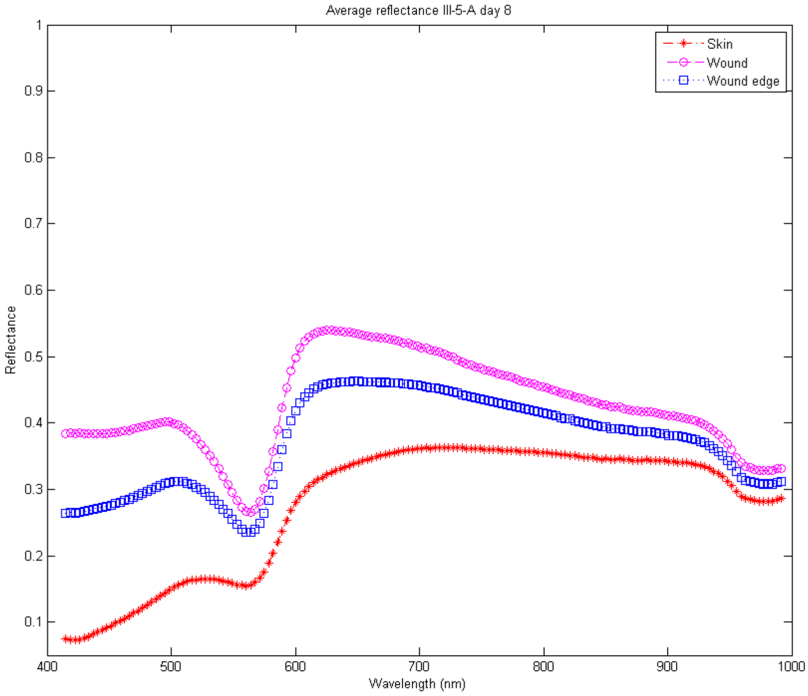

Figure 33: Average reflectance spectrum of skin, wound and wound edge for III-5-A from day 8

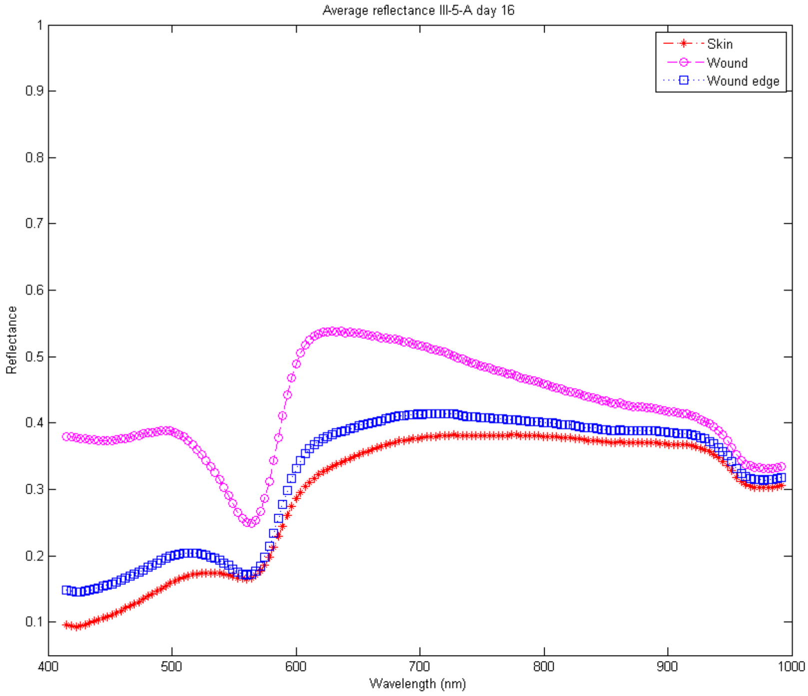

Figure 34: Average reflectance spectrum of skin, wound and wound edge for III-5-A from day 16

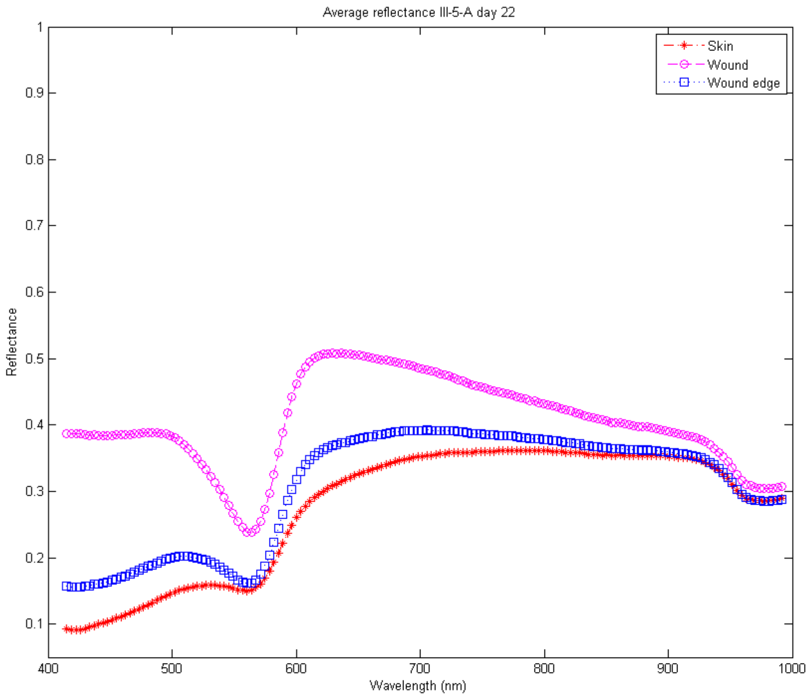

Figure 35: Average reflectance spectrum of skin, wound and wound edge for III-5-A from day 22

Figure 36 and Figure 37 shows the reflectance of the skin, wound and wound edge of II-3-A on day 2 and day 8. There is obviosly a lot of change in the reflectance for all classes, most likely due to the infection, even though the infection was not apparent until day 10. The most noticeable change is the overall lower reflectance values, but also the more flat shape between 500 nm and 700 nm. Also, in Figure 37, the wound has the lowest reflectance for most of the spectrum.

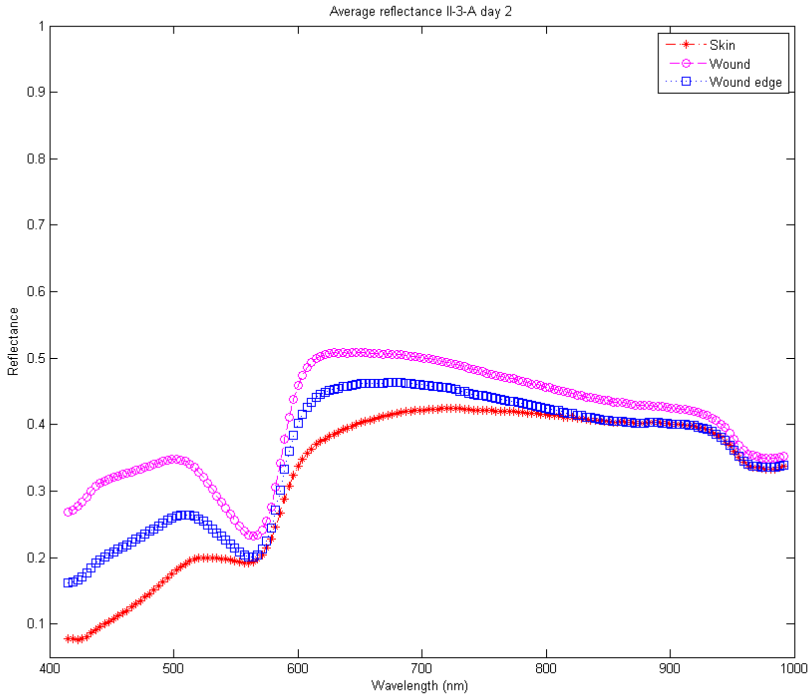

Figure 36: Average reflectance spectrum of skin, wound and wound edge for II-3-A from day 2

From Appendix A.13, it can be seen that the reflectance of I-2-A does not change as drastically as II-3-A, but the reflectance of the skin exceeds the wound edge from 560 nm. From [8] the reflectance of the skin was expected to be the lowest and the wound the highest, and the results from the spectrums presented here confirms this. The reflectance values depends on how much light is detected, and thus depends on how much lights is scattered and absorbed in the layers of the skin. Thus it seems like wound might be less scattering than skin. The thickness of the sample will also affect the scattering and absorption of light, and as the wound models will vary slightly in shape and thickness this will also have an effect on the measured reflectance. The differences in thickness of the wound will also cause the wounds to heal differently.

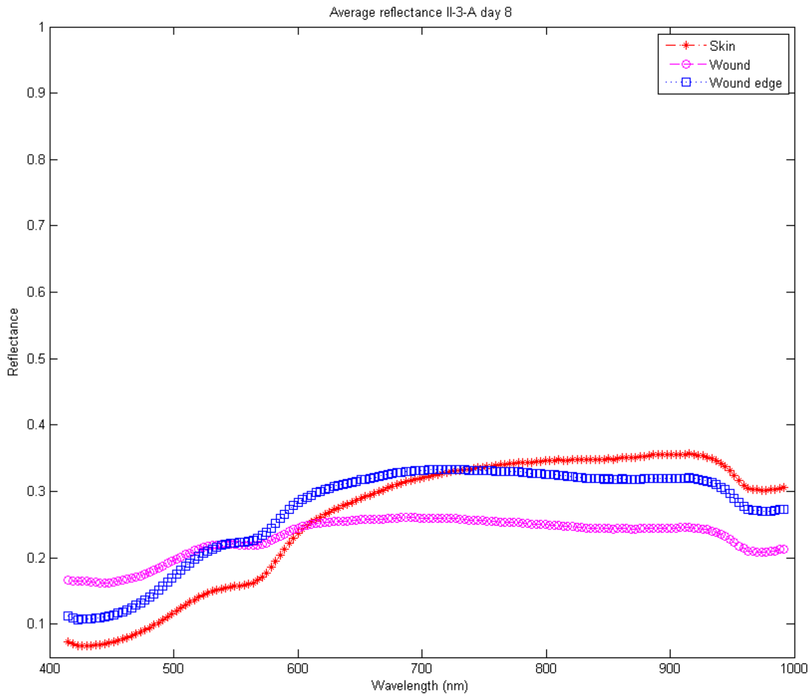

Figure 37: Average reflectance spectrum of skin, wound and wound edge for II-3-A from day 8

In Figure 38 the average reflectance of the skin for I-1-A is plotted to show the change over time. The reflectance on day 8 is distinctly lower than the previous days, which indicates that something has happened to the skin, perhaps causing it to be more scattering.

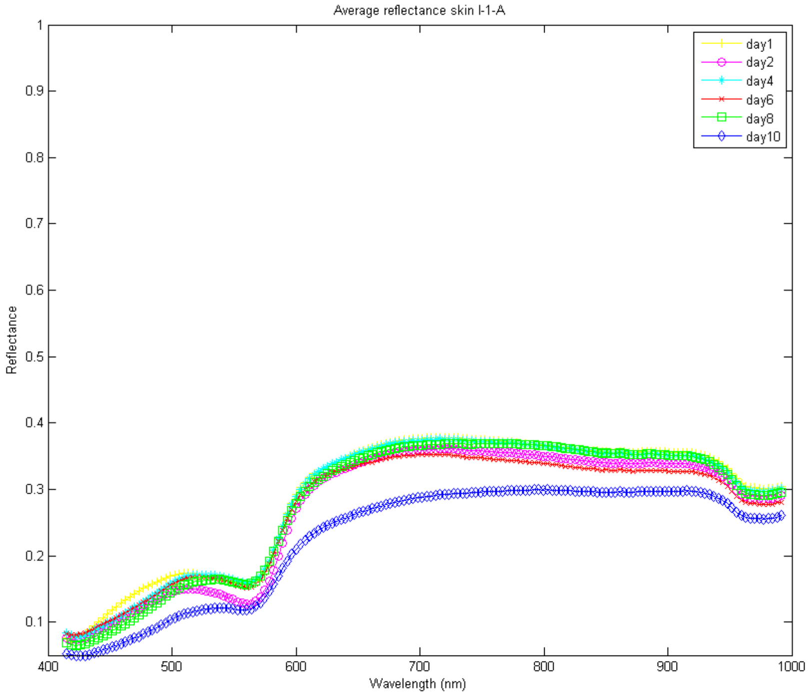

Figure 38: Average reflectance spectrum of the skin I-1-A

Similarly, the same plot has been made for the wound, in Figure 39. Here, the reflectance values are more varied. However in Figure **??** where the change in wound edge is plotted, the reflectance values are lowest on the last days.

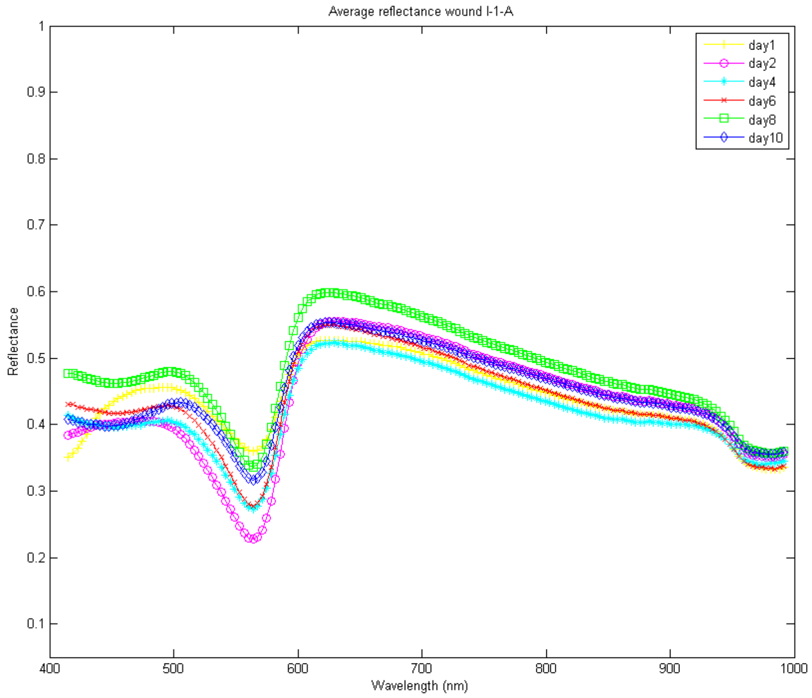

Figure 39: Average reflectance spectrum of the wound I-1-A

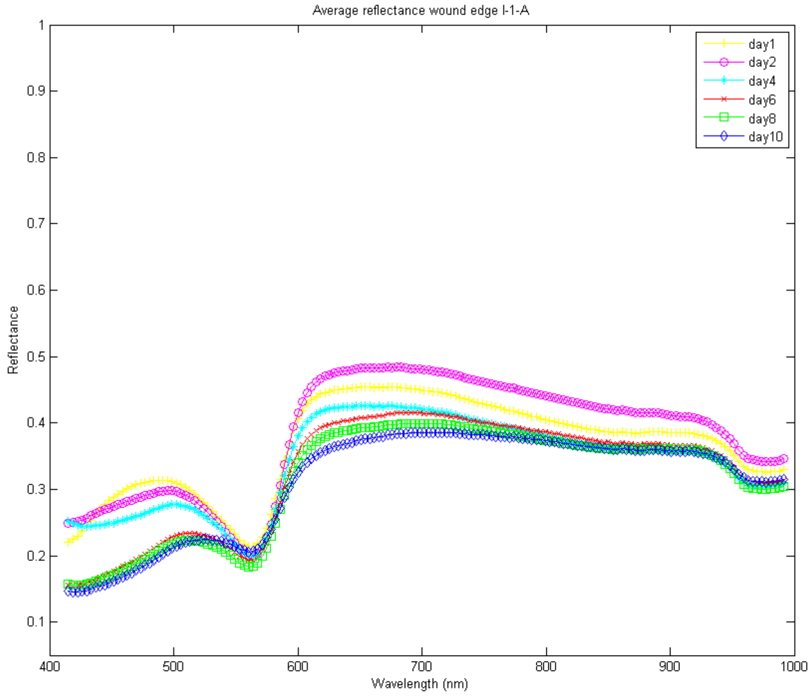

Figure 40: Average reflectance spectrum of the wound edge I-1-A

Figure 38 shows the change in reflectance of I-4-A. This sample had no wound as it was made as a reference sample. I-4-A did not get infected, and the values of the reflectance did not change significantly, but it seems like the reflectance increased slightly with time from 750 nm.

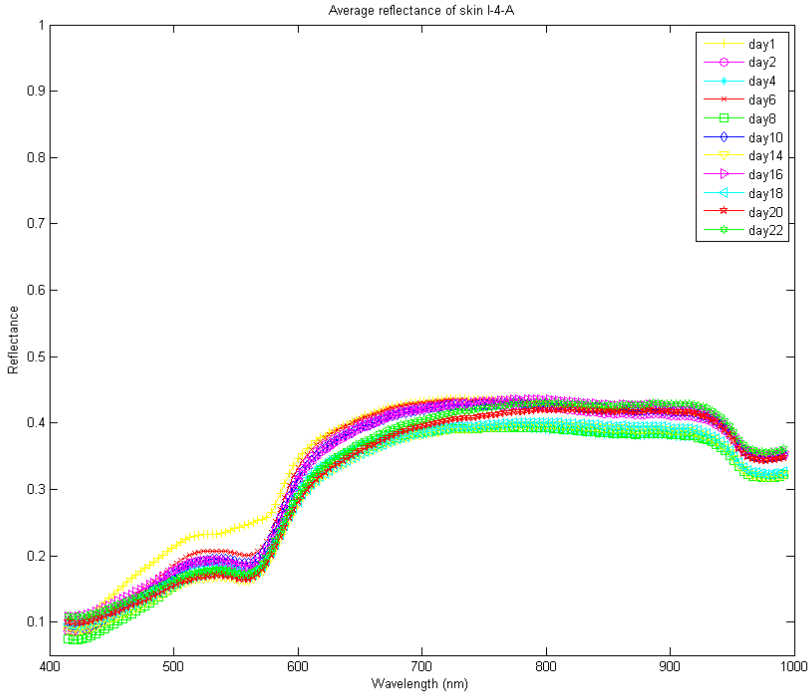

Figure 41: Average reflectance spectrum of the skin I-4-A

Similar plots for the samples not presented here were also created, but will not be presented. Generally, they showed that the reflectance decreased with time, and changed significantly for the infected samples.

In Figure 42, the average reflectance of the medium is plotted against the wavelength.

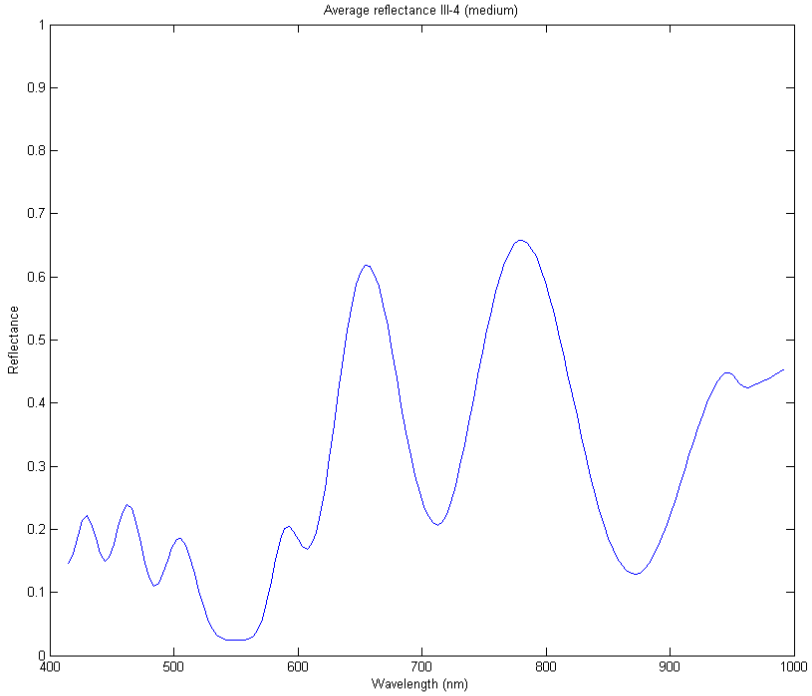

Figure 42: Average reflectance spectrum of the medium from day 1

There is a lot of minimas and maximas in the spectrum of the medium, and the reflectance looks nothing like the reflectance of the medium in [1], where the medium was more similar in shape to that of the wound model. Here, the medium was only analysed for the first day of imaging. The most distinct maximas are located at 655 nm, 781 nm and 948 nm. The most distinct minimas are located at 553 nm, 607 nm, 712 nm, 872 nm and 963 nm.

4.3.3 Normalized reflectance spectrums

To be able to identify the changes over time, the spectrums were normalized at a wavelength where there was no significant maxima or minima. Most of the spectrums were normalized at band 105, which corresponds to a wavelength of 788 nm.

Figure 43, Figure 44 and Figure 45 shows the normalized average reflectance spectrums for the skin, wound and wound edge of I-1-A. In Figure 43, there is maximas at 524 nm, 689 nm and 919 nm, and minimas at 560 nm, 872 nm and 973 nm. In Figure 44 the maximas are located at 502 nm, 621 nm and 919 nm, and the minimas at 564 nm and 977 nm. In Figure 45 there are maximas at 491 nm - 524 nm (shifting to the right with time), 672 nm and 923 nm, and minimas at 564 nm, 858 nm and 974 nm.

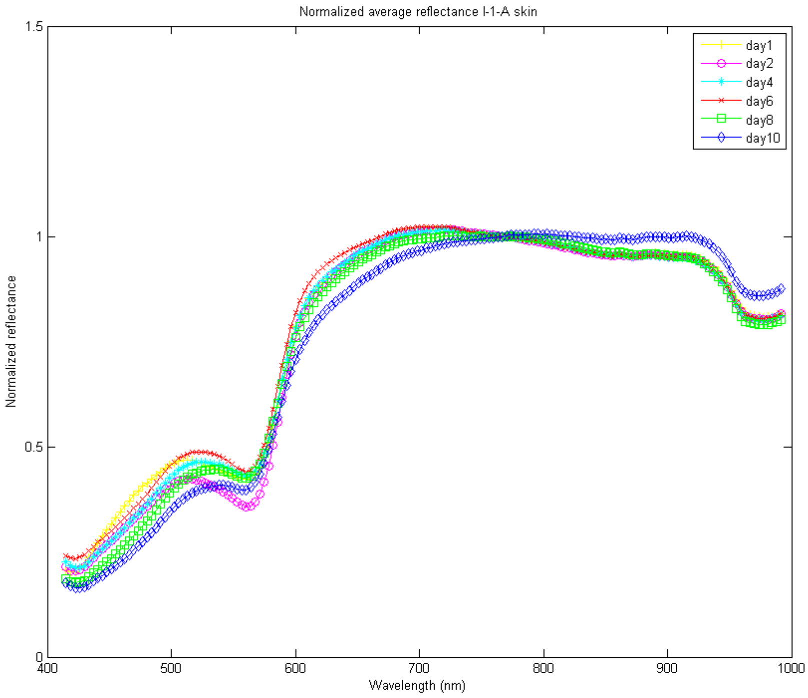

Figure 43: Normalized average reflectance spectrum of the skin I-1-A

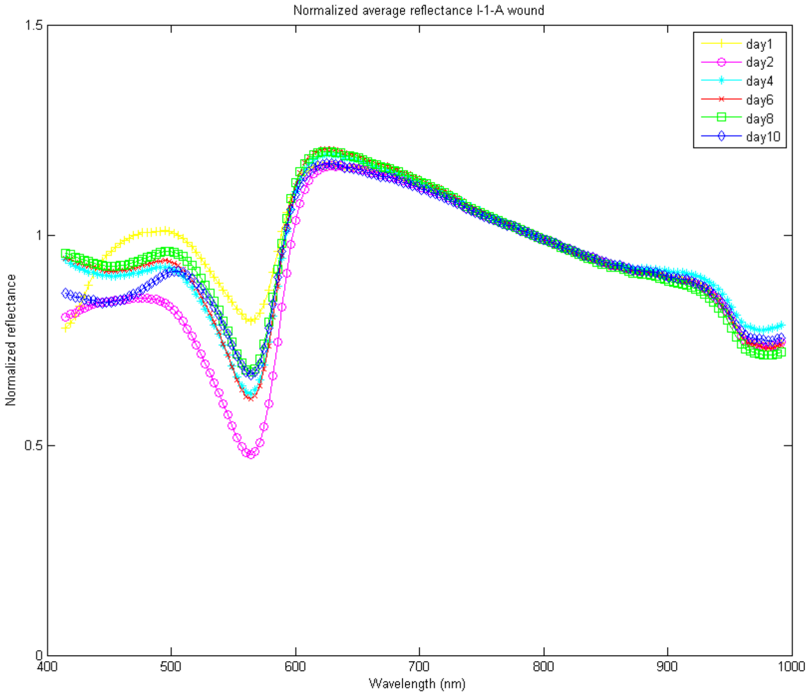

Figure 44: Normalized average reflectance spectrum of the wound I-1-A

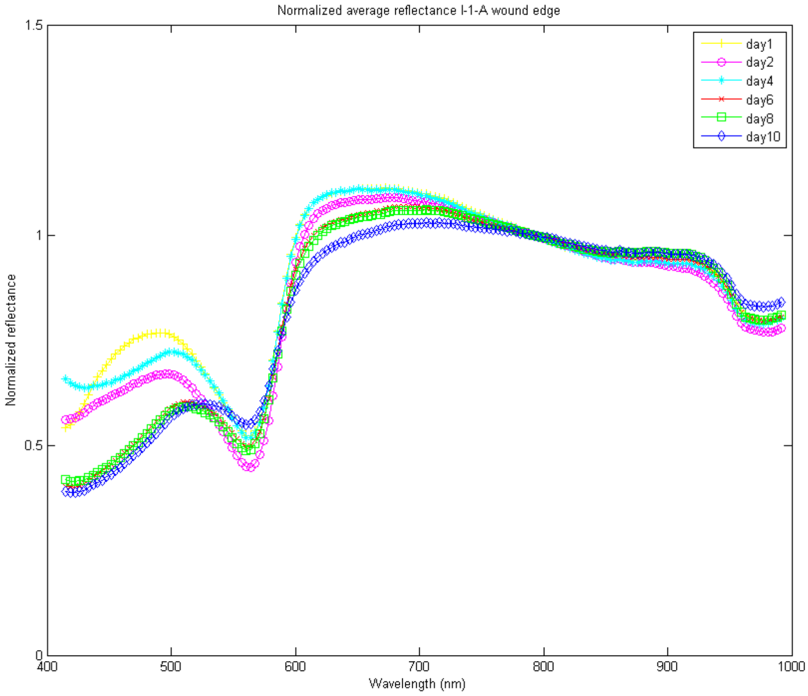

Figure 45: Normalized average reflectance spectrum of the edge I-1-A

Figure 46 shows the normalized average reflectance of I-4-A, sample without wound. As can be seen in the plot, there is not much change in the reflectance, except from day 1, where the reflectance is higher at 500 nm - 600 nm. However, the rest of the measurements seems fairly aligned, and the reason for the higher reflectance at day 1 might be that this measurement was done directly after the wound models were made. The maximas are located at 527 nm, 730 nm and 919 nm, and the minimas at 560 nm, 857 nm and 977 nm.

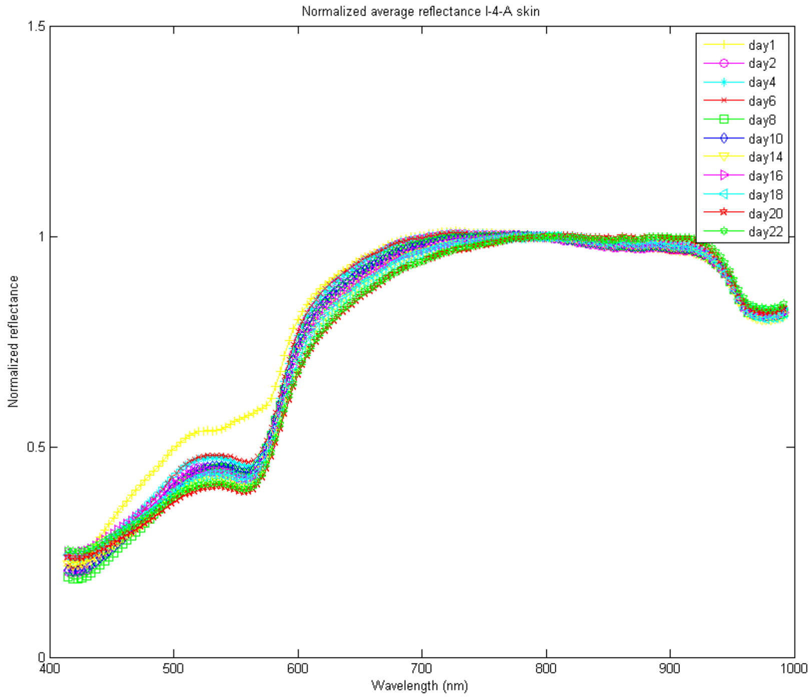

Figure 46: Normalized average reflectance spectrum of the skin I-4-A

Figure 47, Figure 48 and Figure 49 shows the normalized average reflectance of III-5-A for skin, wound and wound edge. The skin changes very little, almost nothing during the time period. Here, the maximas are 516 nm, 712 nm and 915 nm, and the minimas 560 nm, 857 n and 974 nm. The reflectance of the wound on day 1 is higher than the rest of the period from 450 nm to 600 nm. Except from this day, all other maximas are located at 499 nm, 624 nm and 918 nm, and the minimas at 564 nm and 974 nm. For the wound edge, there are maximas at 509 nm, 648 nm and 922 nm, and minimas at 564 nm, 857 nm and 974 nm.

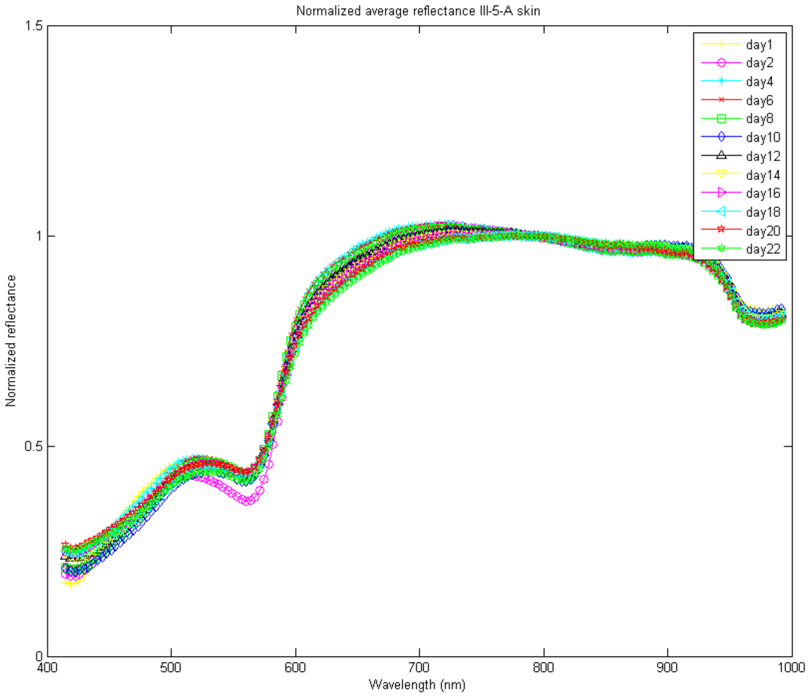

Figure 47: Normalized average reflectance spectrum of the skin III-5-A

Similar normalized reflectance spectrums for samples not presented here can be found in Appendix A.13.4.

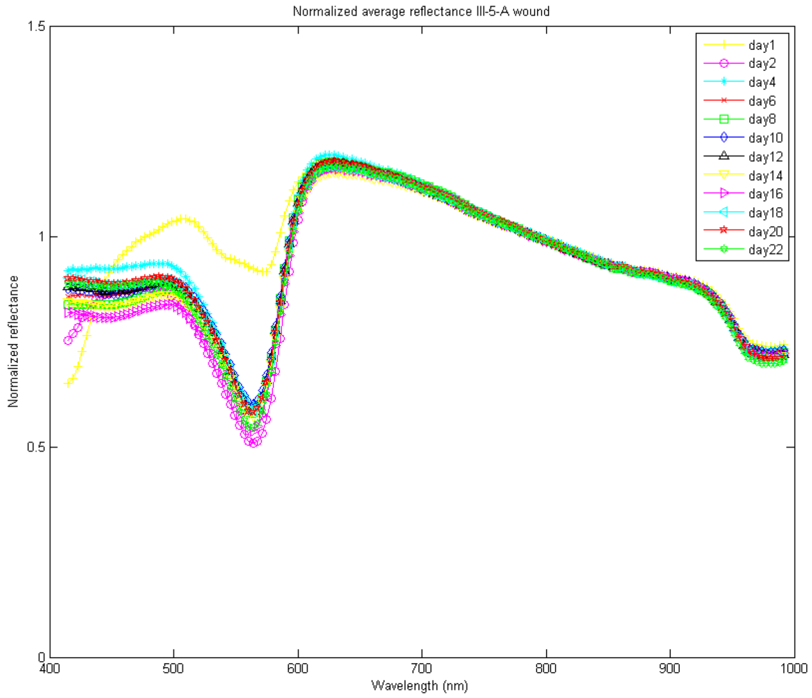

Figure 48: Normalized average reflectance spectrum of the wound III-5-A

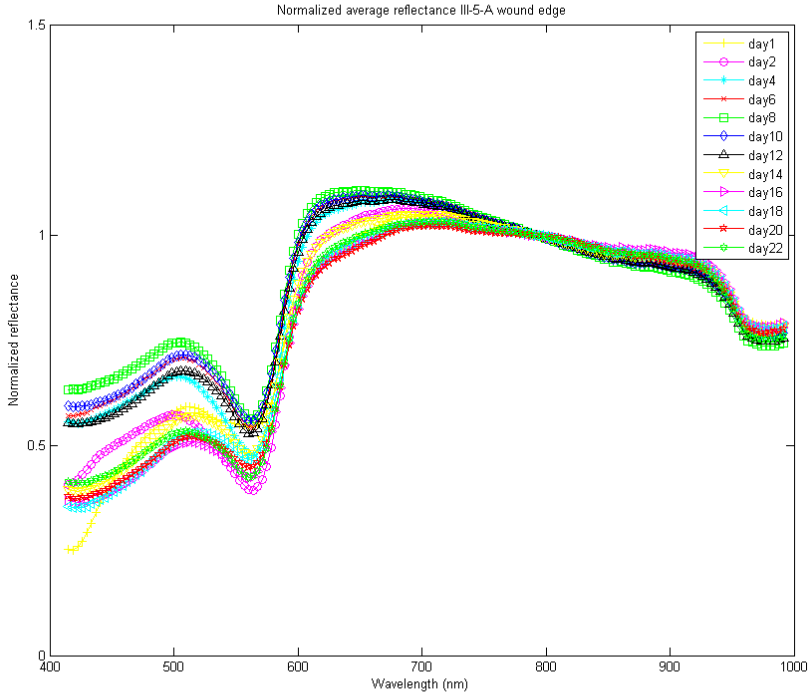

Figure 49: Normalized average reflectance spectrum of the edge III-5-A

Overall, from both the average reflectance spectrums and the normalized spectrums, it seems that the reflectance decreases with time, also according to the findings of [8] and [38]. Gnyawalli et al. describes hyperspectral images of in vivo wound models, with limited access to blood, and found that the reflectance decreased with time. Considering the results found here, and Hegstad's results and conclusion, strengthens the belief that an in vitro model can give similar results as an in vivo model with limited blood access.

4.3.4 Chromophores

By comparing all the normalized reflectance spectrums, it is evident that there are some features common to all spectrums.

Table 4: Characteristic maxima and minima for intact skin

Wavelength	Skin reflectance
520	Maximum
560	Minimum
700	Maximum
850-870	Minimum
920	Maximum
973-977	Minimum

In table 4 the most characteristic maxima and minima for the intact skin is listed. These were found by comparing all the normalized average reflectance spectrums for the samples presented in the previous section and in Appendix A.13.4. In table 5, similar features are presented for the wound.

Table 5: Characteristic maxima and minima for wound

Wavelength	Wound reflectance
500	Maximum
564	Minimum
623	Maximum
857	Minimum
920	Maximum
976	Minimum

In table 6, these features are also listed for the wound edge.

Table 6: Characteristic maxima and minima for wound edge

Wavelength	Wound edge reflectance
510	Maximum
564	Minimum
650-700	Maximum
860	Minimum
922	Maximum
974	Minimum

By comparing these results, there are only slight differences between the classes. The maxima at 500 nm for wound is shifted to 510 nm for the wound edge and 520 nm for the skin. The minima at 564 nm seems consistent with all classes.The minima at 974 nm is also the same in all classes.

Some of the maxima and minima can be identified as absorption peaks by comparing them to absorption spectrums of common chromophores i skin. From [39] the minima at 974 nm corresponds to water absorption. Water also have higher harmonics of the absorption peak, at 870 nm - 890 nm. From [40], lipid has absorption peaks at 900 nm and 770 nm, and a minima in any of these regions may be caused by lipid absorption.

In human skin, absorption peaks of oxy- and deoxyhemoglobin dominates wavelengths shorter than 700 nm [39] [40]. The wound models used here should not contain any blood after cutting off the subcutis and cleaning the skin. The epidermis have no blood vessels, so the only possible place for blood to be present is in the wound itself as the wound should be deep enough to penetrate all of epidermis and a fraction of dermis. The maxima at 500 nm - 520 nm in the reflectance spectrums for skin, wound and the wound edge looks like the absorption mimimum of hemoglobin at 500 nm in [40]. However, considering the lack of blood in the samples, these peaks may be absorption of some other chromophore.

All samples have distinct minima at 560 nm - 564 nm. From Figure 5 [17], cytochrome Fe(III)c' has an absorption peak in the same region. From the same figure, Fe(II)c'NO6 coord has an absorption peak around 540 nm. Fe(III)c' and Fe(II)c'NO5 coord have absorption peaks at 400 nm, Fe(III)c'NO has a peak at 420 nm and Fe(II)c' has a peak at 430 nm. All the samples have reflectance minima in the same region. This might indicate that the maxima and minima seen in the spectrums from the wound models where blood absorption usually takes place, actually are absorption of cytochromes. The same results were found in [1].

4.3.5 Spectral angle mapper

The SAM analysis were done using reference spectrums from day 4, the third day of measurement. Ideally, it would have been better to mask the images before applying SAM, but there were some issues where the well tray insert and the medium were classified as something else, and not metal plate and medium, most likely due to the cell growth around the samples that started already on day 2. Choosing the right thresholds for the classification is also challenging, and may cause too many or too few pixels to be classified as any of the classes.

Figure 50 shows plots of the SAM results of I-1-A from day 1, 8 and 10. This sample got infected between day 8 and 10. From the SAM classification, more pixels are classified as wound edge on day 8 than day 1. On day 10, almost no pixels were classified as wound edge, but there is a gap between the skin and the wound, which may be caused by the infection.

The SAM result from I-5-A is plotted in Figure 51. On day 1, no pixels were classified as wound edge, thus the wound edge on day 1 is omitted in this figure. From day 8 to day 22, it looks like the amount classified as skin has increased, which would be an indication of the wound healing. On day 16, a lot more pixels than day 8 and 22 are classified as wound edge. Some pixels classified as wound edge might be new skin since thin skin will let through more light and reflect more.

Figure 52 shows SAM plots for III-2-A. Also here, more pixels are classified as skin with time. There are some unclassified pixels as well. More SAM plots were analyzed, but will not be presented here. From these, in generel, none of the sampled seemed to heal completely, the infection had a huge impact on the classification, and a lot of pixels were not classified as any of the classes in the infected samples. For some images, some of the well tray were classified as wound or wound edge, and this might indicate that there was a reepithelilization process going on around the samples as well as in the middle, and cells classified as wound here might actually be new skin and should rather have been classified as wound edge. II-2-A in particular had a lot of pixels classified as wound on the well tray insert (on the metal plate, not the holes/medium) from day 8 to day 22.

SAM analysis of I-4-A and III-1-A, samples without wound, classified almost all of the sample as skin for the whole period, with no pixels outside the sample, with I-4-A showing somewhat better results than III-1-A. If a reference spectrum for wound or wound edge were compared to these images, there might have been classified some new cells on the well tray insert, as these wells also had undesired cell growth outside the sample.

(a) Skin day 1. (b) Wound day 1. (c) Edge day 1. (d) Skin, wound and edge day 1.

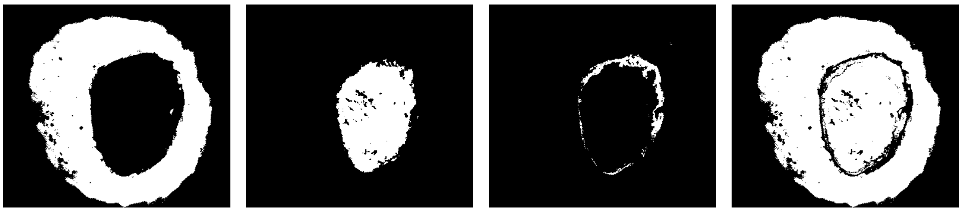

(e) Skin day 8. (f) Wound day 8. (g) Edge day 8. (h) Skin, wound and edge day 8.

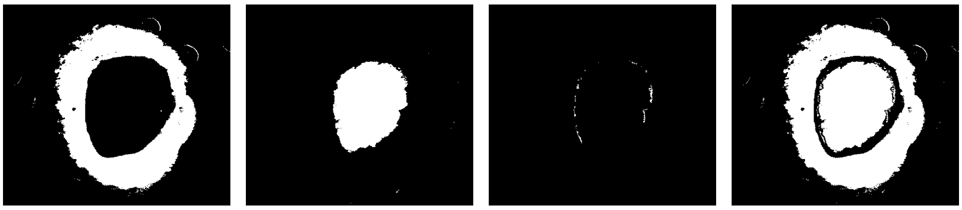

(i) Skin day 10. (j) Wound day 10. (k) Edge day 10. (l) Skin, wound and edge day 10.

Figure 50: SAM I-1-A day 1, 8 and 10.

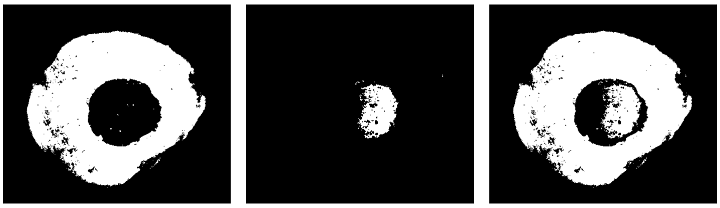

(a) Skin day 1. (b) Wound day 1. (c) Skin, wound and edge day 1.

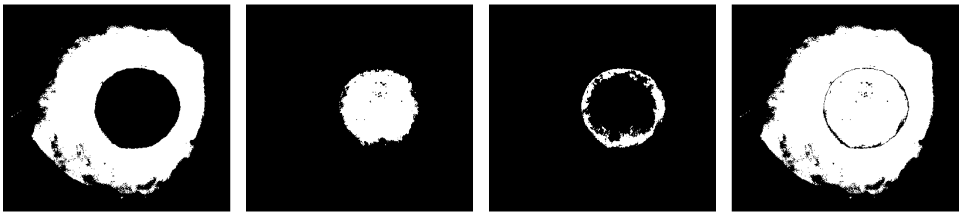

(d) Skin day 8. (e) Wound day 8. (f) Edge day 8. (g) Skin, wound and edge day 8.

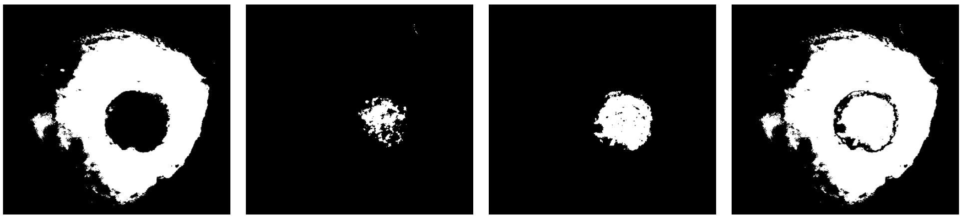

(h) Skin day 16. (i) Wound day 16. (j) Edge day 16. (k) Skin, wound and edge day 16.

(l) Skin day 22. (m) Wound day 22. (n) Edge day 22. (o) Skin, wound and edge day 22.

Figure 51: SAM I-1-A day 1, 8, 16 and 22.

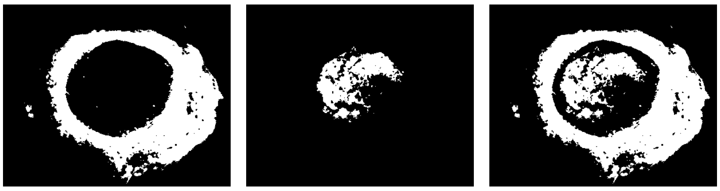

(a) Skin day 1. (b) Wound day 1. (c) Skin, wound and edge day 1.

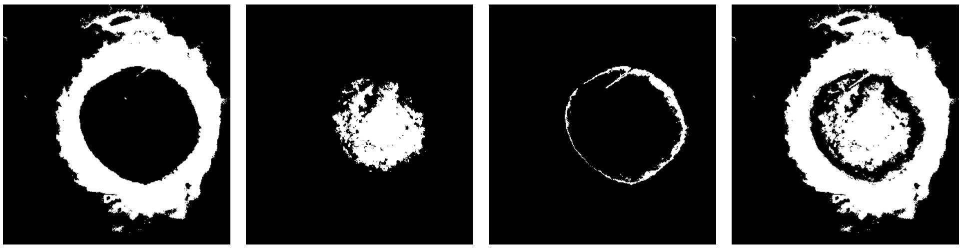

(d) Skin day 8. (e) Wound day 8. (f) Edge day 8. (g) Skin, wound and edge day 8.

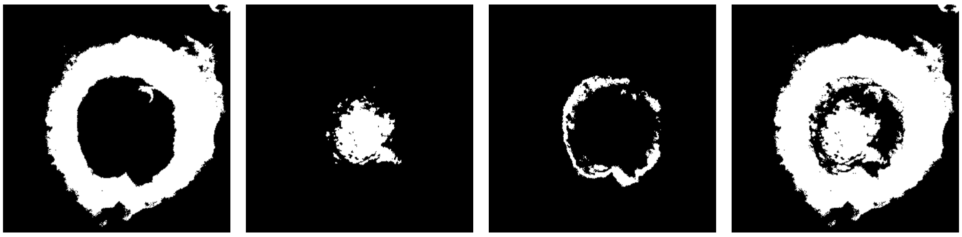

(h) Skin day 16. (i) Wound day 16. (j) Edge day 16. (k) Skin, wound and edge day 16.

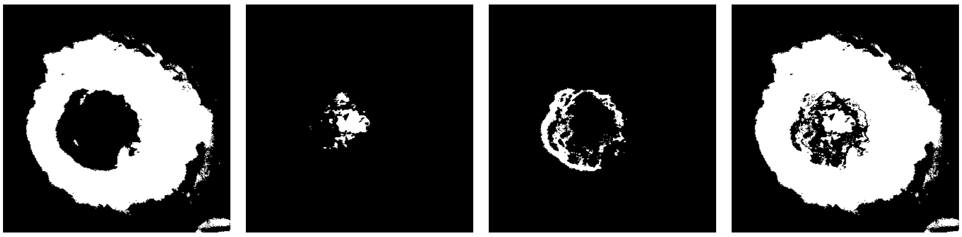

(l) Skin day 22. (m) Wound day 22. (n) Edge day 22. (o) Skin, wound and edge day 22.

Figure 52: SAM III-2-A day 1, 8, 16 and 22.

4.3.6 Relative ratios SAM analysis

The amount of pixels classified as skin, wound or wound edge in the SAM analysis were summed, and the relative ratios of pixels from the different classes calculated. Here, 100% is the sum of pixels classified as skin, wound and wound edge.

In Figure 53, the relative ratios of skin, wound and wound edge for I-1-A are plotted for day 1, 2, 4, 6, 8, and 10. Here, the ratios does not change significantly, but more pixels are classified as wound on day 10, and fewer as wound and wound edge.

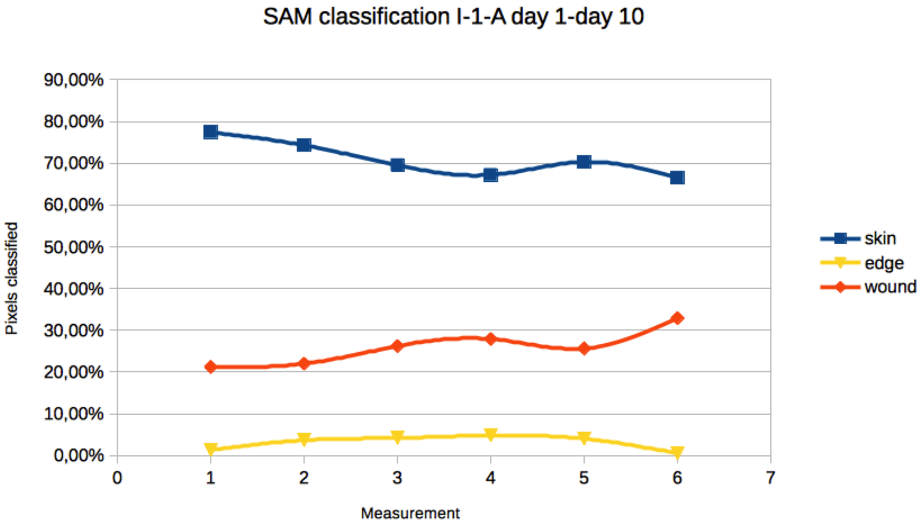

Figure 53: Relative ratios of skin, wound and wound edge from SAM of I-1-A.

In Figure 54 the relative ratios of skin, wound and wound edge are plotted for I-5-A for the whole period of 22 days. Notice that there are no values from day 12. The ratio of pixels classified as skin increased with time, and the ratios of wound and wound edge decreased. More plots of relative ratios can be found in Appendix A.14.

From SAM analysis and visual inspection of the wound models, it can be assumed that none of the wound models healed completely, even though some showed signs of reepithelializing occuring in the sample. From [8] and [2], the expected healing period is 6 - 21 days. The reason why none of these wounds healed might be the infection, or other factors. Thus it is not possible to either validate or dis-

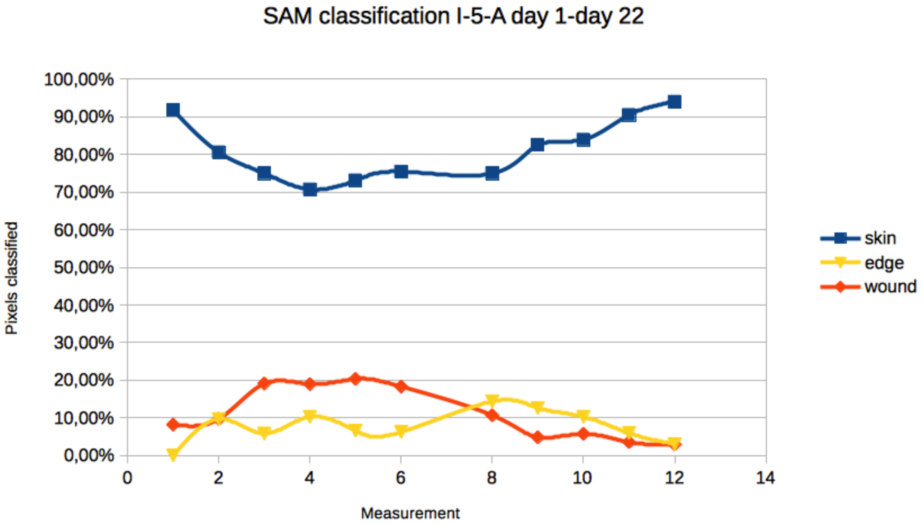

Figure 54: Relative ratios of skin, wound and wound edge from SAM of I-5-A.

card the theory that it should be possible to predict the amount of time it takes for this kind of wounds to heal. Anyway, it seems like SAM classification alone is not sufficient, as pixels outside the sample are classified as wound or wound edge and too many pixels might remain unclassified. At least the image must be masked, remaining only the wound model itself.

The thickness of the wound models might have had an impact on the healing process. If dermis is too thick, the nutrition medium will not be able to reach the epidermis. Without this nutrition, the wound cannot heal [9]. This could have been avoided if the wound model preparation had been done with a custom made wound cutter. This was also discussed in [1]. Even though it has already been attempted, the first version, made by Tore Landsem, was unsuccessful. An optimized method for making the wound models could yield better results in similar researches.

Even though no wound models seemed to heal completely, the infected samples provided an opportunity to study the effect of unexpected cell behaviour on reflectance spectrums and SAM classification. The most apparent changes from healthy to infected sample can be seen in the reflectance spectrums, where the spectrums from the infected day have both a different shape and in some regions much higher or lower values. In Figure 37, it is interesting to see that in this sample, II-3-A, already on day 8 the reflectance values for skin, wound and wound edge are so much different. This might indicate that the infection started in II-3-A in tray II. The reason for the infection and how the infection spread from one tray to the other two, or if an infection occured separetely in all three trays in the same couple of days, is not known. However, it is more likely that the infection spread from one tray to the other two.

The only occasions where the samples were exposed to risk of infection, was during the imaging. The lid of the well tray had to be taken off, and therefore exposing the wound models to air. This was unavoidable, as the whole camera setup could not be placed inside a laminar flow cabinet, which might have saved the wound models from getting infected.

4.3.7 Monte Carlo simulation

A Monte Carlo simulation was done by Matija Milanic for bloodless skin and wound. As melanin is stored in the keratinocytes in epidermis, skin versus wound can be compared by removing the melanin from the skin data. As can be seen in Figure 55, there are distinct differences between skin and wound.

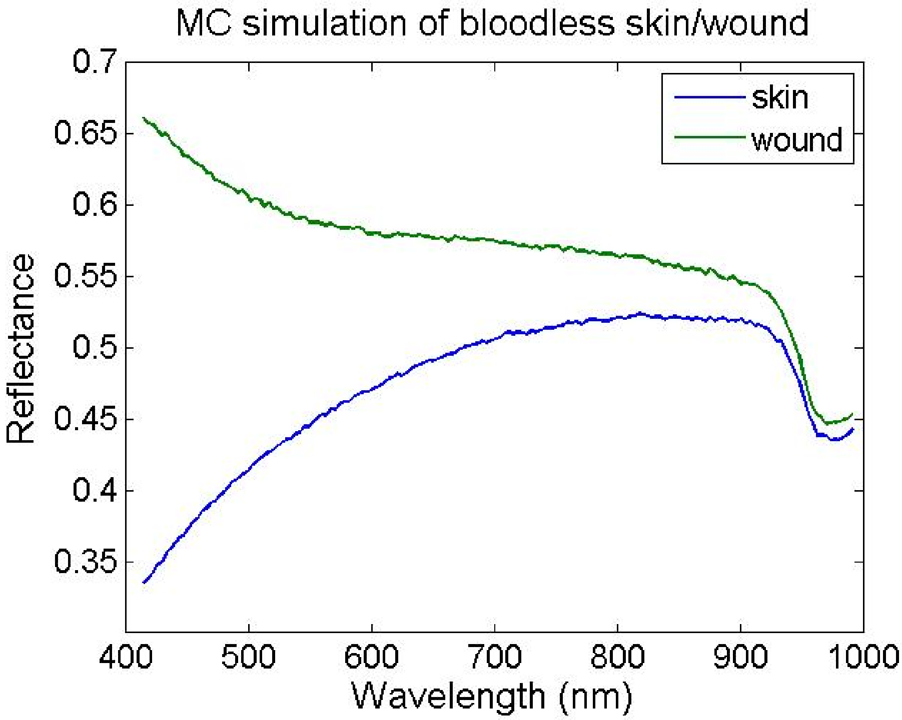

Figure 55: Monte Carlo simulation of bloodless skin and wound.

This corresponds to the results from the reflectance spectrums where the skin has the lowest reflectance and the wound the highest, and the spectrums are more separated at shorter wavelengths. The water absorption peak from [39] at 974 nm can also be seen in Figure 55.

The large differences in reflectance value at 400 nm in both the averaged reflectance spectrums and the Monte Carlo simulation can most likely be explained by scattering.

5 Conclusions

Hyperspectral imaging of in vitro wound models from human skin have been performed using white light. The imaging period was 22 days. Analysis has been performed using Matlab.

The hyperspectral images were analysed using Matlab. This was done by analysing reflectance spectrums, SAM classification and Monte Carlo simulation.

Reflectance spectrums showed that the reflectance overall decreased with time, and that skin had the lowest reflectance and wound had the highest reflectance. SAM analysis showed that in some samples, the wound partly healed, but no wound closed completely in the 22 days the wounds were followed. Monte Carlo simulation resulted in large differences in reflectance between the intact skin and the wound. From the reflectance spectrum analysis, some chromophores in skin could be identified using absorption spectrums, and the reflectanc spectrums might reveal cytochromes present in the skin.

Both reflectance spectrum analysis and SAM analysis showed that an infection in the wound models will give detectable changes in reflectance.

The preparation of the wound models might have caused the wounds to not heal. Too thick dermis does not allow the nutrition to reach the epidermis, thus epithelialization would be impossible. The reason for why none of the wound healed completely might also be affected by the infection that occurred in some of the samples.

Bibliography

[1] I. Haneberg, *Hyperspectral imaging of in vitro wound models from human skin*, Norwegian University of Science and Technology, Department of Physics, 2014.

[2] G. Kratz, *Modeling of Wound Healing Processes in Human Skin Using Tissue Culture*, Microscopy research and technique 42:345-350, 1998

[3] M. Martin et al., *Development of an Advanced Hyperspectral Imaging (HSI) System with Applications for Cancer Detection*, Annals of Biomedical Engineering, Vol 34, No. 6, pp. 1061-1068, 2006.

[4] L. L. Randeberg et al., *In vivo hyperspectral imaging of traumatic skin injuries in a porcine model*, Progress in Biomedical Optics and Imaging - Proceedings of SPIE, vol. 6426, 2007.

[5] E. L. P. Larsen et al., *Hyperspectral imaging of atherosclerotic plaques in vitro*, Journal of Biomedical Optics 16(2), 026011, 2011.

[6] D. Yudovskyet al., *Foot technology, part 2 of 2: Hyperspectral imaging in diabetic foot wound care*, Journal of diabetes science and technology, vol. 4, no. 5, p. 1099, 2010.

[7] L. V. Wang and W. Hsin-L, *Biomedical Optics Principles and Imaging*, Wiley, 2007.

[8] J-L. Hegstad, *Hyperspektral avbildning av in vitro sårmodeller fra menneskehud*, Norwegian University of Science and Technology, Department of Electronics and Telecommunications, Student Master thesis, 2013.

[9] T. Langeland, *Huden, i Store medisinske leksikon*, 2009. http://sml.snl.no/huden. *Accessed October 2. 2013*

[10] PromoCell GmbH, Sickingenstraße 63/65, D-69126 Heidelberg, Germany, http://www.promocell.com/fileadmin/promocell/Kapitelbilder/Keratinocytes_2.jpg *Accessed January 5, 2014.*

[11] A. Baroni et al., *Structure and function of the epidermis related to barrier properties*, Clinics in Dermatology, 2012, 257-267

[12] D. A. Tamarkin, *Repair of skin*, 2011. http://faculty.stcc.edu/AandP/AP/AP1pages/Units1to4/skin/repairof.htm *Accessed December 2. 2013*

[13] D. Hudson, *The integumentary system*, University of Miami, 2008, http://www.as.miami.edu/chemistry/2008-1-MDC/2085/Chap5_New/chap5_classversion.htm. *Accesed October 7. 2013*

[14] V. Arnoux et al., *Cutaneous wound reepithelialization* in Rise and Fall of Epithelial Phenotype, Molecular Biology Intelligence Unit, pp. 111-134, Springer US, 2005.

[15] R. Nave, *Cytochrome Complex in Electron Transport*, http://hyperphysics.phy-astr.gsu.edu/hbase/organic/cytochrome.html *Accessed January 19, 2014*

[16] Y-L. P. Ow et al., *Cytochrome c: functions beyond respiration*, Nat Rev Mol Cell Biol, Nature Publishing Group, 2008.

[17] http://www.biochemsoctrans.org/bst/033/0187/bst0330187f02.htm?resolution=STD *Accessed January 19, 2014.*

[18] S. A. Nelson, *Properties of light and examination of isotropic substances*, Tulane University, 2011, http://www.tulane.edu/ sanelson/eens211/proplight.htm *Accessed December 7. 2013*

[19] A. Bjørgan and L. L. Randeberg, *Estimation of Skin Optical Parameters for Real-Time Hyperspectral Imaging Applications*, Proc. of SPIE Vol. 8926, 2014.

[20] R. C. Haskell et al., *Boundary Conditions for the Diffusion Equation in Radiative Transfer*, J Opt Soc Am A, 1994;11(10):2727-2741.

[21] L. Svaasand et al., *Tissue parameters determining the visual appearance of normal skin and port-wine stains.*, Laser Med Sci, 10:55 65, 1995.

[22] T. Siiskonen, M. Tapiovaara, A. Kosunen, M. Lehtinen, and E. Vartiainen, *Monte Carlo simulations of occupational radiation doses in interventional radiology*, British Journal of Radiology 80(954), 460-468, 2007.

[23] T.C. Haas, *Statistical assessment of spatio-temporal pollutant trends and meteorological transport models*, Atmospheric Environment 32(11), 1865-1879, 1998.

[24] P.E. Labeau, *Probabilistic dynamics: Estimation of generalized unreliability through efficient Monte Carlo simulation*, Annals of Nuclear Energy 23(17), 1355-1369, 1996.

[25] A. Bjørgan, *Estimation of Skin Optical Parameters for Real-Time Hyperspectral Imaging Applications using GPGPU Parallel Computing.*, Student Master thesis, Norwegian University of Science and Technology, Department of Physics, 2013.

[26] H. Hernandez-Palacios and L.L. Randeberg, *Intercomparison of EMCCD- and sCMOS-based imaging spectrometers for biomedical applications in low-light conditions.*, Proc. of SPIE Vol. 8215 82150Q-1, 2012.

[27] A. A. Nielsen, R.Larsen, *Restoration of GERIS Data Using the Maximum Noise Fractions Transform*, IMSOR Image Analysis Group, Institute of Mathematical Modelling, Technical University of Denmark, Lyngby, Denmark, 1994.

[28] B. Luc et al., *Optimized Spectral Angle Mapper classification of spatially heterogeneous dynamic dune vegetation, a case study along the Belgian coastline*, The 9th International Symposium on Physical Measurements and Signatures in Remote Sensing (ISPMSRS). Beijing, October 17-19, 2005.

[29] K. Jansson, G. Kratz and A. Haegerstrand, *Characterization of a new in vitro model for studies of reepithelialization in human partial thickness wounds*, In Vitro Cellular & Development Biology - Animal, vol. 32, no. 9, pp. 534-540, 1996.

[30] Standa Ltd, Svitrigailos 4-39, 03222 Vilnius, Lithuania, http://www.standa.lt *Accessed May 12. 2014*

[31] Norsk Elektro Optikk AS, Lørenskog, Norge

[32] HySpex Main Specifications, VNIR-1600, http://www.hyspex.no *Accessed October 4. 2013*

[33] Exelis Visual Information Solutions, http://www.exelisvis.com/ProductsServices/ENVI/EN *Accessed October 4. 2013*

[34] MathWorks, https://www.mathworks.se *Accessed October 4. 2013*

[35] Labsphere, http://www.labsphere.com/products/reflectance-standards-and-targets/spectralon-reflectance-standards/diffuse-reflectance-standards.aspx *Accessed May 11. 2014*

[36] Asahi Spectra USA, Inc., 23505 Crenshaw Boulevard, Suite 229 Torrance, CA 90505, USA, http://www.asahi-spectra.com/opticalfilters/detail.asp?key=XHQA440 *Accessed May 11. 2014.*

[37] GIMP - The GNU Image Manipulation Program, http://www.gimp.org

[38] S.C. Gnyawalli et al., *Hyperspectral imaging of ischemic wounds*, Proc. SPIE, vol. 8229, pp. 822910-822910-7. 2012.

[39] I. V. Meglinski, S. J. Matcher, *Computer simulation of the skin reflectance spectra*, Computer Methods and Programs in Biomedicine 70(2):179-186, 2003.

[40] P. Beard, *Biomedical photoacoustic imaging*, Department of Medical Physics and Bioengineering, University College London, 2011.

A Appendix

A.1 Reading header files

The script readHyperHeader is used to read the hyperspectral headerfile corresponding to the converted image. The script read the size of the image, the number of bands and data types, and returns the wavelengths.

Code 1: readHyperHeader.m

```
function info = readHyperHeader(hdrfile)
[path name ext] = fileparts(hdrfile);
current_dir = pwd;
if ~isempty(path)
    cd(path)
end
hdrfile = [name '.hdr'];
fid = fopen(hdrfile);
if fid > 0
    info.headerExists = 1;
    while fid;
        line = fgetl(fid);
        if line == -1
            break
        else
            eqsn = findstr(line,'=');
            if ~isempty(eqsn)
                param = strtrim(line(1:eqsn-1));
                param(findstr(param,'␣')) = '_';
                value = strtrim(line(eqsn+1:end));
                if isempty(str2num(value))
                    if ~isempty(findstr(value,'{')) && isempty(findstr(value,'}'))
                     while isempty(findstr(value,'}'))
                         line = fgetl(fid);
                         value = [value,strtrim(line)];
                     end
                    end
                    eval(['info.',param,'␣=␣''',value,''';'])
                else
                    eval(['info.',param,'␣=␣',value,';'])
```

```
                end
            end
        end
    end
    fclose(fid);
    %% Put wavelengths into an array:
    if isfield(info,'wavelength')
        lambda = sscanf(info.wavelength(2:end-1), '%f,');
        info.wavelength = lambda;
    else
        info.wavelength = [];
    end
    if isfield(info,'default_bands')
        rgbBands = cell2mat(textscan(info.default_bands,'{%d8,%d8,%d8}'));
        info.default_bands = rgbBands;
    else
        info.default_bands = [];
    end
    if isfield(info,'description')
        description = info.description(2:end-1);
        info.description = description;
    else
        info.description = '';
    end
    %% Set binary format parameters
    switch info.byte_order
        case {0}
            info.byte_order = 'ieee-le';
        case {1}
            info.byte_order = 'ieee-be';
        otherwise
            info.byte_order = 'n';
    end
    switch info.data_type
        case {1}
            info.data_type = 'uint8';
        case {2}
            info.data_type= 'int16';
```

```
        case{3}
            info.data_type= 'int32';
        case {4}
            info.data_type= 'single';
        case {5}
            info.data_type= 'double';
        case {6}
            disp('>>␣Sorry,␣Complex␣(2x32␣bits)data␣currently␣
               not␣supported');
            disp('>>␣Importing␣as␣double-precision␣instead');
            info.data_type= 'double';
        case {9}
            error('Sorry,␣double-precision␣complex␣(2x64␣bits)␣
               data␣currently␣not␣supported');
        case {12}
            info.data_type= 'uint16';
        case {13}
            info.data_type= 'uint32';
        case {14}
            info.data_type= 'int64';
        case {15}
            info.data_type= 'uint64';
        otherwise
            error(['File␣type␣number:␣',num2str(dtype),'␣not␣
               supported']);
    end
else
    info.headerExists = 0;
end
cd(current_dir)
```

A.2 Import images

The script getHSI is used to read the hyperspectral image and import it into Matlab.

Code 2: getHSI.m

```
function [img, lam] = getHSI(filename, info, lamI, region)
%loads HySpex image for Ingvild
% INPUT:
% filename - hyspex filename
% info     - header info, use info = readHyperHeader(hdrfile)
% lamI     - lamI = [lower lam, upper lam]
% region   - region = [x1,x2,y1,y2]
% OUTPUT:
% image - hyspex image
% lam - wavelength region

%find bands
if(isempty(lamI))
    lamI = [info.wavelength(1),info.wavelength(end)];
end
if(length(lamI)==1)
    lamI = [lamI, lamI];
end
lam = info.wavelength;
Nl = length(lam);
la = find(lam<=lamI(1));
if(~isempty(la))
    la = la(end);
else
    la = 1;
end

lb = find(lam>=lamI(2));
if(~isempty(lb))
    lb = lb(1);
else
    lb = length(lam);
end
lam = lam(la:lb);
```

```

%find region
rX = info.samples;
rY = info.lines;

if(isempty(region))
    x1 = 1;
    x2 = rX;
    y1 = 1;
    y2 = rY;
else
    x1 = region(1);
    x2 = region(2);
    y1 = region(3);
    y2 = region(4);
end

if(x1>x2)
    x = x1;
    x1 = x2;
    x2 = x;
end
if(y1>y2)
    y = y1;
    y1 = y2;
    y2 = y;
end
if(x1>rX)
    fprintf('\n␣x1␣too␣large\n');
    return;
end
if(x2>rX)
    x2 = rX;
end
if(y1>rY)
    fprintf('\n␣y1␣too␣large\n')
    return;
end
if(y2>rY)
```

```
    y2 = rY;
end

%read image
I = zeros(rX, length(lam));
img = zeros(length(lam),x2-x1+1,y2-y1+1);

fid = fopen(filename);
%read first line
tline = fread(fid,8,'*uchar');
if (tline ~= [72;89;83;80;69;88;0;0])
    fprintf('\nNot␣a␣hyspex␣file.\n');
    return;
end
%move to the HSI
fseek(fid,info.header_offset, 'bof');
%read image
if(strcmp(info.data_type,'single'))
    fini = (y1-1)*rX*Nl*4;%4 bytes
    fseek(fid,fini,'cof');
    for(i=1:(y2-y1+1))
        I = fread(fid,rX*Nl,info.data_type);
        I = reshape(I,rX,Nl);
        I = I';
        img(:,:,i) = I(la:lb,x1:x2);
        fprintf('.');
        if(mod(i,150)==0)
            fprintf('\n');
        end
    end
else%int
    fini = (y1-1)*rX*Nl*2;%2 bytes
    fseek(fid,fini,'cof');
    for(i=1:(y2-y1+1))
        I = fread(fid,rX*Nl,info.data_type);
        I = reshape(I,rX,Nl);
        I = I';
        img(:,:,i) = I(la:lb,x1:x2);
        fprintf('.');
```

```
            if(mod(i,150)==0)
                  fprintf('\n');
            end
      end
end
fclose(fid);
fprintf('\n');
return
```

A.3 Convert to reflectance

The script img2R converts radiance data to reflectance data.

Code 3: img2R.m

```matlab
function imgR = img2R(imgS,imgWS, lam)
% converts image from radiance to reflectance
% INPUT:
%   imgS - img of sample (lam, x, y)
%   imgWS - img of WS (lam, x, yWS)
%   lam - wavelengths
% OUTPUT:
%   imgR - img in R (lam, X, y)

Nl = size(imgS,1);
Nx = size(imgS,2);
Ny = size(imgS,3);
NyS = size(imgWS,3);

% mean of WS
calWS = mean(imgWS,3);

% reflectance of WS
WS = load('SRT-99-050.txt');
RWS = interp1(WS(:,1),WS(:,2), lam);

% calibrate
imgR = zeros(Nl, Nx, Ny);

for i = 1:Ny
    for j = 1:Nx
        imgR(:,j,i) = imgS(:,j,i).*RWS./calWS(:,j);
    end
end
```

A.4 Forward MNF transformation

The script MNF performs a forward MNF transformation.

Code 4: MNF.m

```
function [imgMNF, V, eigval, mimg] = MNF(img,NaboNo,satur)
%Calculates MNF of a hyspex image
% Based on Asgeirs C++ code
% INPUT:
%   img - HySpex image (Nl, Nx, Ny)
%   NaboNo - neigbhour points included in noise matrix estimation order
%             values >= 0
%   satur - find saturation points (0=off/1=on)
% OUTPUT:
%   V - MNF vectors
%   eigval - eigenvalues
%   mimg - mean values of the image

Nl = size(img,1);
Nx = size(img,2);
Ny = size(img,3);


if(satur==1)
    for i=1:Ny
        for j=1:Nx
            if(max(img(:,j,i))>=8e-4)
                img(:,j,i)=0;
            end
        end
    end
end

% rearange img from 3d to 2d
img2 = reshape(img, Nl, Nx*Ny);

%% forward MNF

% Remove mean from data
```

```
mimg = mean(img2,2);
for i = 1:Nl
    img2(i,:) = img2(i,:) - mimg(i);
end

% calculate img covariance matrix
imgCov = (img2*img2.')/(Nl-1);

% estimate nose covaraiance matrix
% find local mean
if(NaboNo>0)
lmimg = zeros(Nl,Nx,Ny);
for i = 1:Ny
    for j = 1:Nx
        lx = j-NaboNo;
        hx = j+NaboNo;
        ly = i-NaboNo;
        hy = i+NaboNo;
        if(lx<=0)
            lx = 1;
        end
        if(ly<=0)
            ly = 1;
        end
        if(hx>Nx)
            hx = Nx;
        end
        if(hy>Ny)
            hy = Ny;
        end
        m = img(:,lx:hx,ly:hy);
        m = reshape(m,Nl,size(m,2)*size(m,3));
        %remove zero vectors
        sizm = size(m,2);
        for k = 1:sizm
            ik = sizm-k+1;
            ms = sum(m(:,ik));
            if(ms==0)
                m(:,ik)=[];
```

```
            end
        end
        if(isempty(m))
            m = zeros(Nl,1);
        end
        lmimg(:,j,i) = mean(m,2);
    end
end
%estimate noise
noise = img - lmimg;
noise = reshape(noise, Nl, Nx*Ny);
noiseCov = (noise*noise.')/(Nl-1);

% 0-order =  using value from previus line (Asgeir)
else
noise = zeros(Nl,Nx-1,Ny);
    for i = 1:Nx-1
        noise(:,i,:) = img(:,i,:) - img(:,i+1,:);
    end
%estimate noise
noise = reshape(noise, Nl, (Nx-1)*Ny);
noiseCov = (noise*noise.')/(Nl-1);
end

% generalized eigenvalue problem
[V,D] = eig(imgCov,noiseCov);

% extracts eigvals from D
eigval = zeros(size(D,1),1);
for i = 1:size(D,1)
    eigval(i) = D(i,i);
end

% sort by eigenvalue magnitude
[eigval,IX] = sort(eigval,'descend');

% sort eigen vectors
v = zeros(size(V,1),1);
for i = 1:floor(length(eigval)/2)
```

```
    v = V(:,i);
    V(:,i)=V(:,IX(i));
    V(:,IX(i))=v;
end

% calculate MNF transform
imgMNF = V'*img2;
imgMNF = reshape(imgMNF, Nl, Nx, Ny);
end
```

A.5 Inverse MNF transformation

The script iMNF performs an inverse MNF transformation.

Code 5: iMNF.m

```
function [imgiMNF] = iMNF(imgMNF, vMNF, mimg, N)
%Calculates inverse of MNF transform
% INPUT:
%   imgMNF - MNF transformed image
%   vMNF - MNF vector matrix
%   mimg - img mean
%   N - number of included MNF vectors
% OUTPUT:
%   imgiMNF - inverse of MNF transformed image

Nl = size(imgMNF,1);
if(N>Nl)
    N=Nl;
end
Nx = size(imgMNF,2);
Ny = size(imgMNF,3);

%% Inverse MNF
ivMNF = inv(vMNF);
if(N<Nl-1)
    ivMNF(N+1:end,:)=0;
end
imgMNF = reshape(imgMNF, Nl, Nx*Ny);
imgiMNF = ivMNF'*imgMNF;

for i = 1:Nl
    imgiMNF(i,:) = imgiMNF(i,:) + mimg(i);
end

imgiMNF = reshape(imgiMNF, Nl, Nx, Ny);
end
```

A.6 Create RGB image of sample

The script RGB creates an RGB image of the sample.

Code 6: RGB.m

```
imgRc = squeeze(imgiMNF(66,:,:));
imgGc = squeeze(imgiMNF(28,:,:));
imgBc = squeeze(imgiMNF(16,:,:));

imgRGB(:,:,1) = imgRc;
imgRGB(:,:,2) = imgGc;
imgRGB(:,:,3) = imgBc;

imtool(imgRGB)
```

A.7 Select pixels from the classes skin, wound and wound edge

The script pixel_selection allows for point and click-selection of pixels from the different classes skin, wound and wound edge, and stores the reflectance in arrays and calculates the average reflectance for each wavelength.

Code 7: pixel_selection.m

```
figure; imshow(imgRGB) % change the name of the image

s1  = impoint;
s1_pos = floor(getPosition(s1));
s2  = impoint;
s2_pos = floor(getPosition(s2));
s3  = impoint;
s3_pos = floor(getPosition(s3));
s4  = impoint;
s4_pos = floor(getPosition(s4));
s5  = impoint;
s5_pos = floor(getPosition(s5));
s6  = impoint;
s6_pos = floor(getPosition(s6));
s7  = impoint;
s7_pos = floor(getPosition(s7));
s8  = impoint;
s8_pos = floor(getPosition(s8));
s9  = impoint;
s9_pos = floor(getPosition(s9));
s10  = impoint;
s10_pos = floor(getPosition(s10));
s11  = impoint;
s11_pos = floor(getPosition(s11));
s12  = impoint;
s12_pos = floor(getPosition(s12));
s13  = impoint;
s13_pos = floor(getPosition(s13));
s14  = impoint;
s14_pos = floor(getPosition(s14));
s15  = impoint;
s15_pos = floor(getPosition(s15));
```

```
s16  = impoint;
s16_pos = floor(getPosition(s16));
s17  = impoint;
s17_pos = floor(getPosition(s17));
s18  = impoint;
s18_pos = floor(getPosition(s18));
s19  = impoint;
s19_pos = floor(getPosition(s19));
s20  = impoint;
s20_pos = floor(getPosition(s20));
%%
%%GET SPECTRAL INFORMATION

d1 = imgiMNF(:,s1_pos(2),s1_pos(1));
d2 = imgiMNF(:,s2_pos(2),s2_pos(1));
d3 = imgiMNF(:,s3_pos(2),s3_pos(1));
d4 = imgiMNF(:,s4_pos(2),s4_pos(1));
d5 = imgiMNF(:,s5_pos(2),s5_pos(1));
d6 = imgiMNF(:,s6_pos(2),s6_pos(1));
d7 = imgiMNF(:,s7_pos(2),s7_pos(1));
d8 = imgiMNF(:,s8_pos(2),s8_pos(1));
d9 = imgiMNF(:,s9_pos(2),s9_pos(1));
d10 = imgiMNF(:,s10_pos(2),s10_pos(1));
d11 = imgiMNF(:,s11_pos(2),s11_pos(1));
d12 = imgiMNF(:,s12_pos(2),s12_pos(1));
d13 = imgiMNF(:,s13_pos(2),s13_pos(1));
d14 = imgiMNF(:,s14_pos(2),s14_pos(1));
d15 = imgiMNF(:,s15_pos(2),s15_pos(1));
d16 = imgiMNF(:,s16_pos(2),s16_pos(1));
d17 = imgiMNF(:,s17_pos(2),s17_pos(1));
d18 = imgiMNF(:,s18_pos(2),s18_pos(1));
d19 = imgiMNF(:,s19_pos(2),s19_pos(1));
d20 = imgiMNF(:,s20_pos(2),s20_pos(1));
%%
%SAVE SPECTRA IN ONE VARIABLE

spectra(:,1) = d1;
spectra(:,2) = d2;
spectra(:,3) = d3;
```

```
spectra(:,4) = d4;
spectra(:,5) = d5;
spectra(:,6) = d6;
spectra(:,7) = d7;
spectra(:,8) = d8;
spectra(:,9) = d9;
spectra(:,10) = d10;
spectra(:,11) = d11;
spectra(:,12) = d12;
spectra(:,13) = d13;
spectra(:,14) = d14;
spectra(:,15) = d15;
spectra(:,16) = d16;
spectra(:,17) = d17;
spectra(:,18) = d18;
spectra(:,19) = d19;
spectra(:,20) = d20;
%%
%CALCULATE MEAN SPECTRUM

avgs = squeeze(mean(spectra,2));
```

A.8 Plot the average reflectance

The script plotaverage plots the average reflectance for skin, wound and wound edge versus the wavelength.

Code 8: plotaverage.m

```
%PLOT AVERAGE SPECTRUMS
%   avgs = average spectrum of intact skin
%   avgw = average spectrum of wound
%   avge = average spectrum of wound edge

figure;
plot(lam,avgs,'-.r*')
hold on
plot(lam,avgw,'--mo')
plot(lam,avge,':bs')
hold off

xlabel('Wavelength␣(nm)');
ylabel('Reflectance');
legend('Skin','Wound','Wound␣edge');

%REMEMBER to add title and check axis
%%

%PLOT CHANGE IN REFLECTANCE

figure;
plot(lam,day1,'-y+');
hold on
plot(lam,day2,'-mo');
%hold on
plot(lam,day4,'-c*');
plot(lam,day6,'-rx');
plot(lam,day8,'-gs');
plot(lam,day10,'-bd');
%plot(lam,day12,'-k^');
%plot(lam,day14,'-yv');
%plot(lam,day16,'-m>');
%plot(lam,day18,'-c<');
```

```
%plot(lam,day20,'-rp');
%plot(lam,day22,'-gh');
hold off

xlabel('Wavelength (nm)');
ylabel('Reflectance');
legend('day1','day2','day4','day6','day8','day10');
```

A.9 Spectral angle mapper

The script SAM performs spectral angle mapper classification.

Code 9: SAM.m

```
function [imgSAM] = SAM(img, endm)
%Calculates spectral angle mapper
% INPUT:
%   img - image (lam, x, y)
%   endm - end member
% OUTPUT:
%   imgSAM - SAM image

Nl = size(img,1);
Nx = size(img,2);
Ny = size(img,3);

imgSAM = zeros(Nx,Ny);

for i=1:Ny
    for j=1:Nx
        a = img(:,j,i)';
        imgSAM(j,i) = a*endm/(norm(a)*norm(endm));
    end
end


end
```

A.10 Plot SAM results

The script plotSAM plots the results from the SAM classification and sums the number of pixels in each class.

Code 10: plotSAM.m

```
%%% PLOT SAM RESULTS

[skinSAM] = SAM(imgiMNF,avgs);
%imtool(skinSAM)
skinSAMbw = skinSAM > 0.995;
imtool(skinSAMbw);
%%

[woundSAM] = SAM(imgiMNF,avgw);
woundSAMbw = woundSAM > 0.997;
imtool(woundSAMbw);
%%

[edgeSAM] = SAM(imgiMNF,avge);
edgeSAMbw = edgeSAM > 0.9995;
imtool(edgeSAMbw);
%%

class = double(skinSAMbw) + 2*double(woundSAMbw) + 3*double(edgeSAMbw);
imtool(class)
%%

skin = sum(skinSAMbw(:))
wound = sum(woundSAMbw(:))
edge = sum(edgeSAMbw(:))
```

A.11 Plotting normalized reflectance spectrums

The script normplot plots normalized average reflectance spectrums.

Code 11: normplot.m

```
%%% Plot normalized reflectance spectrums
%%%% b = normalization band


avgn1 = avg1;
norm1 = avg1(b);
for i = 1:size(avgn1),
    avgn1(i) = avgn1(i)/norm1;
end

avgn2 = avg2;
norm2 = avg2(b);
for i = 1:size(avgn2),
    avgn2(i) = avgn2(i)/norm2;
end

avgn4 = avg4;
norm4 = avg4(b);
for i = 1:size(avgn4),
    avgn4(i) = avgn4(i)/norm4;
end

avgn6 = avg6;
norm6 = avg6(b);
for i = 1:size(avgn6),
    avgn6(i) = avgn6(i)/norm6;
end

avgn8 = avg8;
norm8 = avg8(b);
for i = 1:size(avgn8),
    avgn8(i) = avgn8(i)/norm8;
end

avgn10 = avg10;
```

```
norm10 = avg10(b);
for i = 1:size(avgn10),
    avgn10(i) = avgn10(i)/norm10;
end

avgn12 = avg12;
norm12 = avg12(b);
for i = 1:size(avgn12),
   avgn12(i) = avgn12(i)/norm12;
end

avgn14 = avg14;
norm14 = avg14(b);
for i = 1:size(avgn14),
    avgn14(i) = avgn14(i)/norm14;
end

avgn16 = avg16;
norm16 = avg16(b);
for i = 1:size(avgn16),
    avgn16(i) = avgn16(i)/norm16;
end

avgn18 = avg18;
norm18 = avg18(b);
for i = 1:size(avgn18),
    avgn18(i) = avgn18(i)/norm18;
end

avgn20 = avg20;
norm20 = avg20(b);
for i = 1:size(avgn20),
    avgn20(i) = avgn20(i)/norm20;
end

avgn22 = avg22;
norm22 = avg22(b);
for i = 1:size(avgn22),
    avgn22(i) = avgn22(i)/norm22;
```

```
end

figure;
plot(lam,avgn1,'-y+');
hold on
plot(lam,avgn2,'-mo');
%hold on
plot(lam,avgn4,'-c*');
plot(lam,avgn6,'-rx');
plot(lam,avgn8,'-gs');
plot(lam,avgn10,'-bd');
plot(lam,avgn12,'-k^');
plot(lam,avgn14,'-yv');
plot(lam,avgn16,'-m>');
plot(lam,avgn18,'-c<');
plot(lam,avgn20,'-rp');
plot(lam,avgn22,'-gh');
hold off

xlabel('Wavelength␣(nm)');
ylabel('Normalized␣reflectance');
legend('day1','day2','day4','day6','day8','day10','day12','day14','day16','day18','day20','day22');
%legend('day2','day4','day6','day8','day10');
%legend('day1','day2','day4','day6','day8','day10','day14','day16','day18','day20','day22');
```

A.12 RGB images of samples

A.12.1 Tray I

Wound models with 3 mm wound, lifted with suction device.

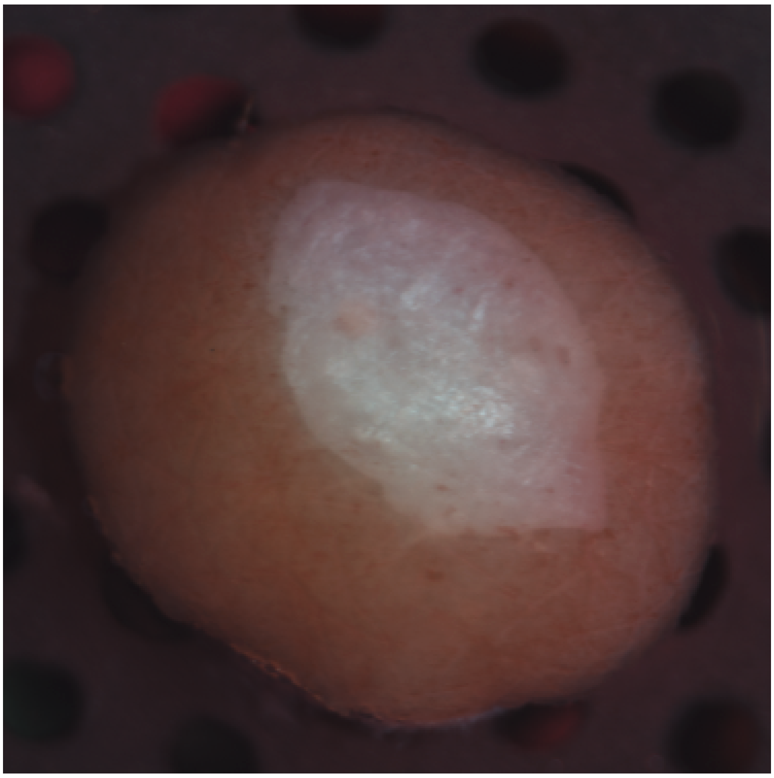

Figure 56: RGB image of I-2-A on day 1

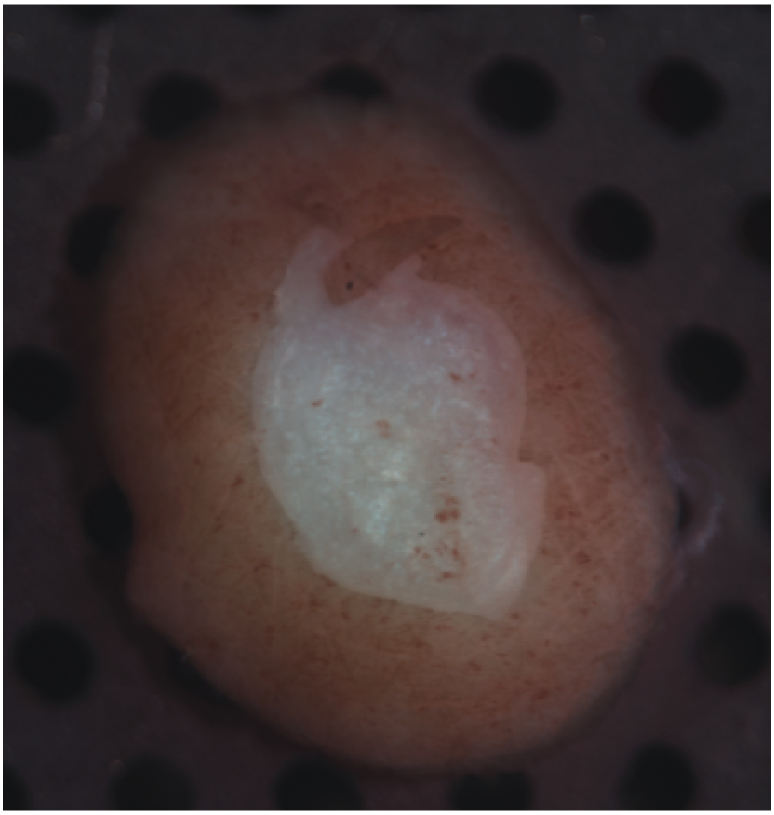

Figure 57: RGB image of I-3-A on day 1

A.12.2 Tray II

Wound models with 3 mm wound, lifted with needle.

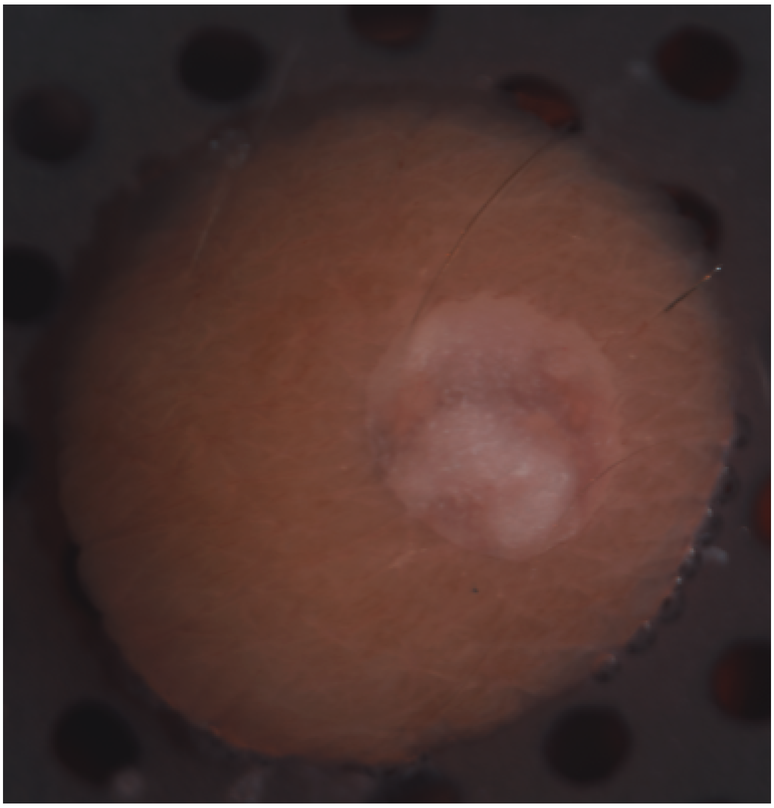

Figure 58: RGB image of II-2-A on day 2

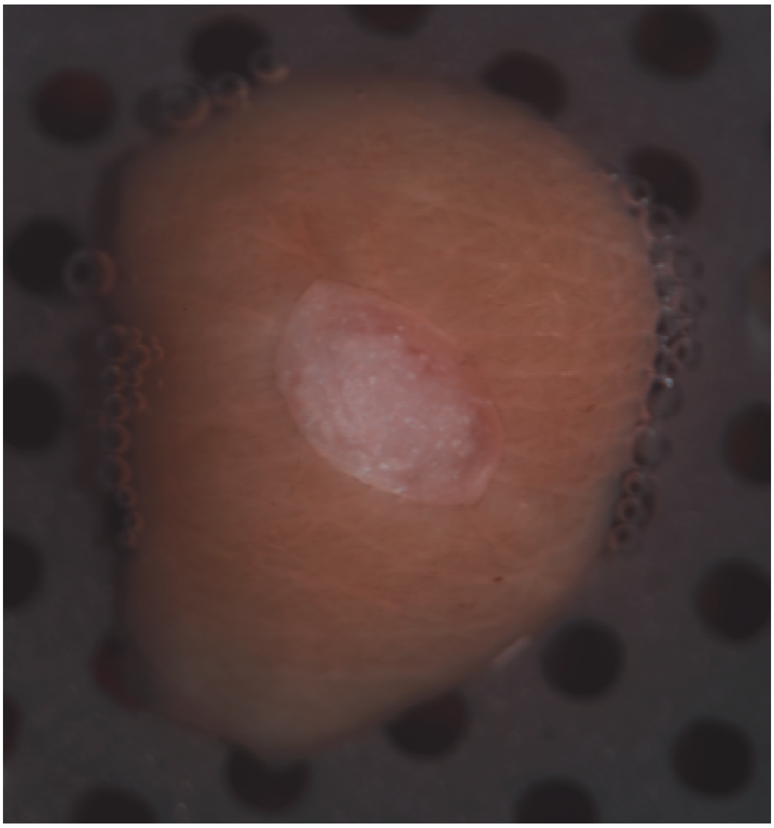

Figure 59: RGB image of II-6-A on day 2

A.12.3 Tray III

Wound models with 4 mm wound lifted with needle.

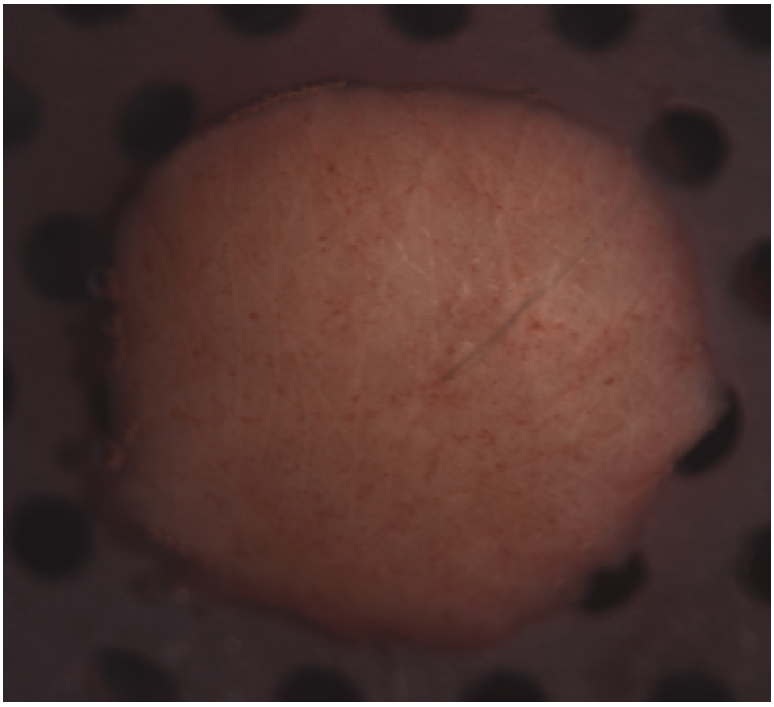

Figure 60: RGB image of III-1-A on day 1

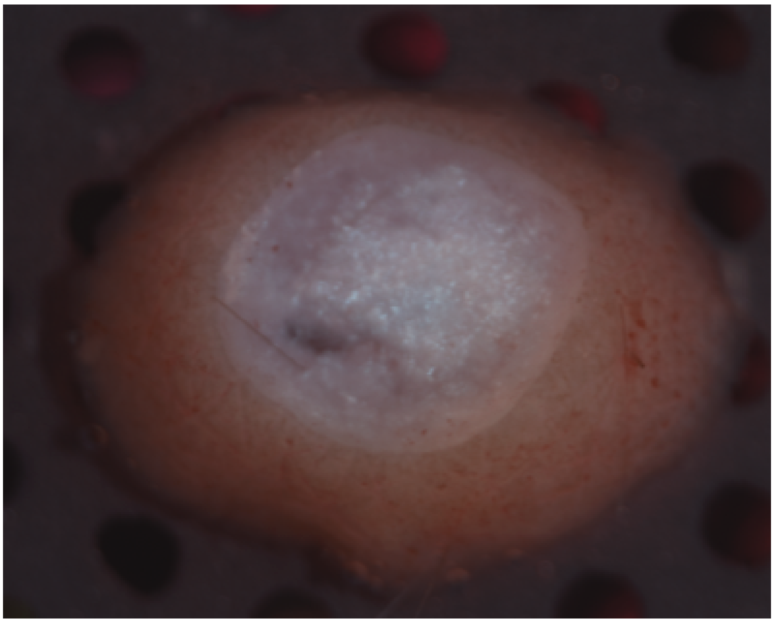

Figure 61: RGB image of III-2-A on day 1

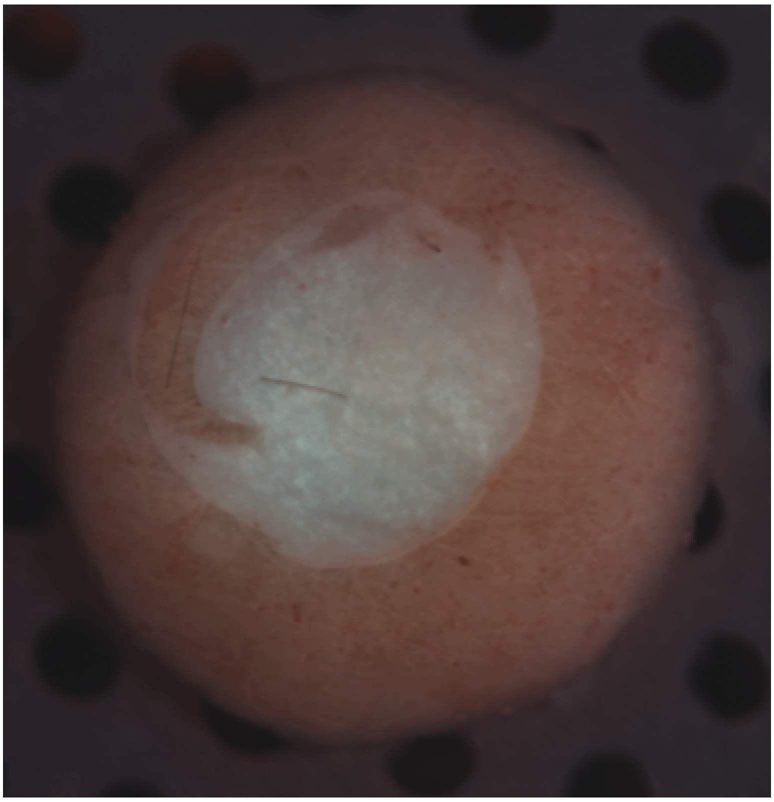

Figure 62: RGB image of III-3-A on day 1

A.13 Reflectance spectrums

A.13.1 Tray I

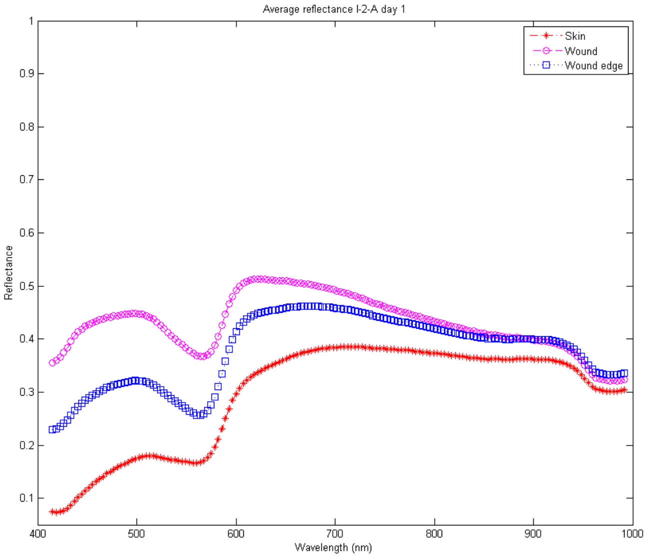

Figure 63: Average reflectance spectrum of skin, wound and wound edge for I-2-A from day 1

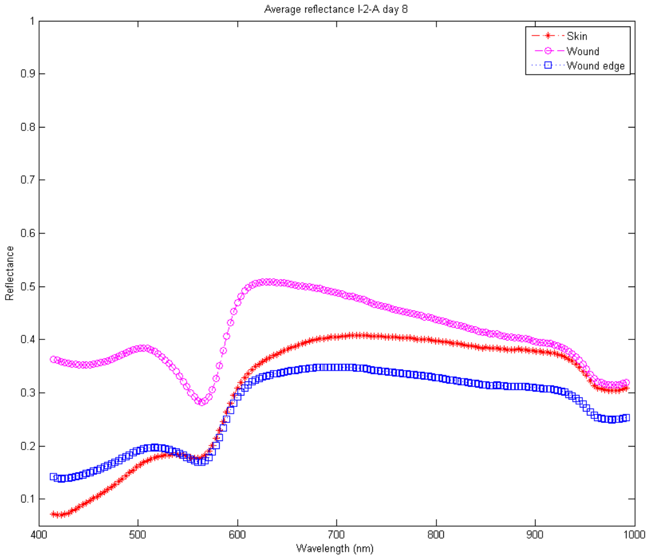

Figure 64: Average reflectance spectrum of skin, wound and wound edge for I-2-A from day 8

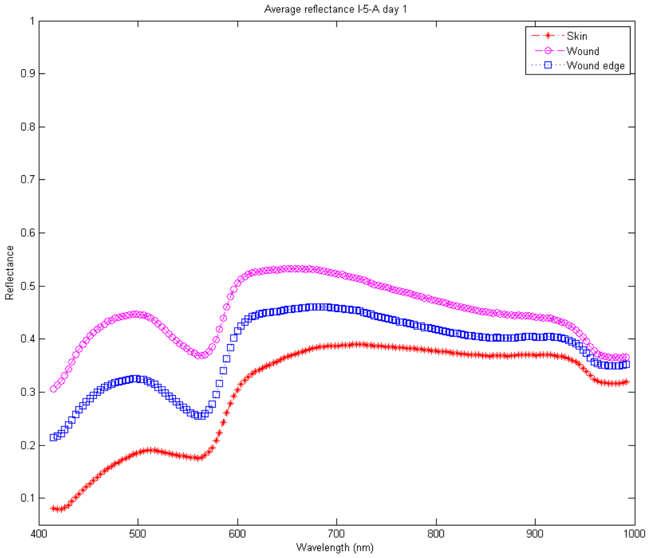

Figure 65: Average reflectance spectrum of skin, wound and wound edge for I-5-A from day 1

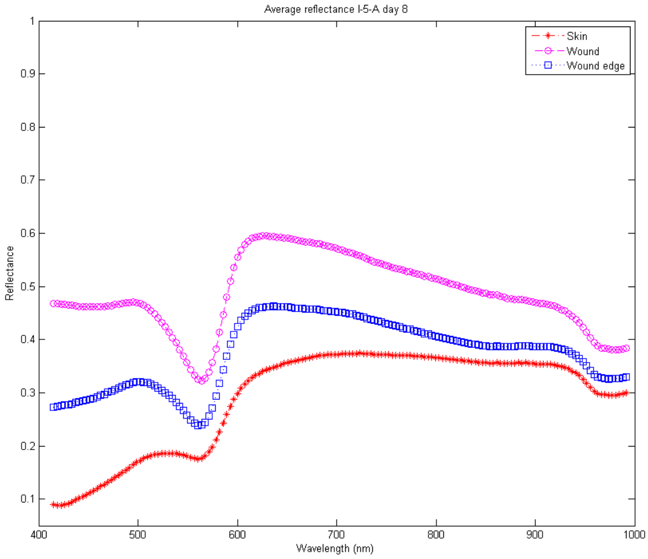

Figure 66: Average reflectance spectrum of skin, wound and wound edge for I-5-A from day 8

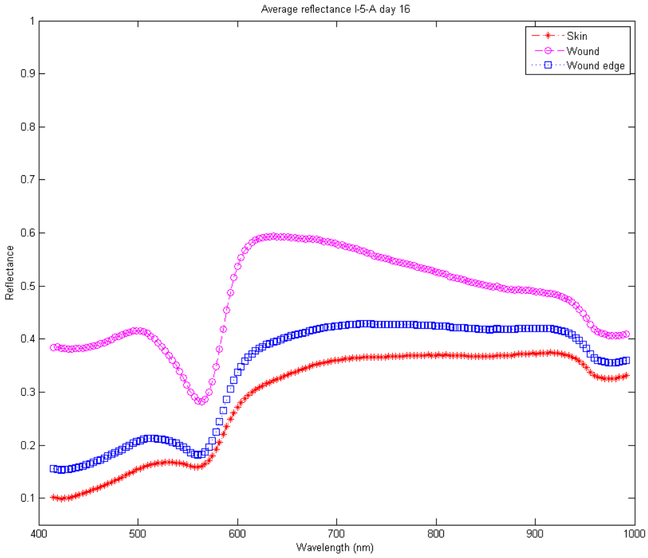

Figure 67: Average reflectance spectrum of skin, wound and wound edge for I-5-A from day 16

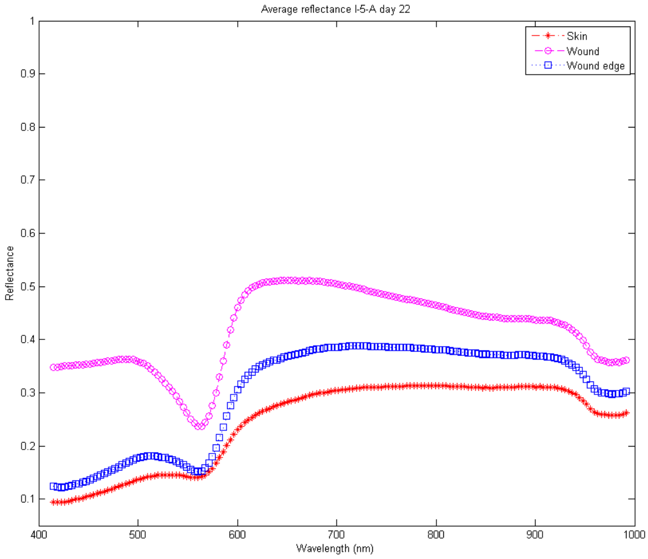

Figure 68: Average reflectance spectrum of skin, wound and wound edge for I-5-A from day 22

A.13.2 Tray II

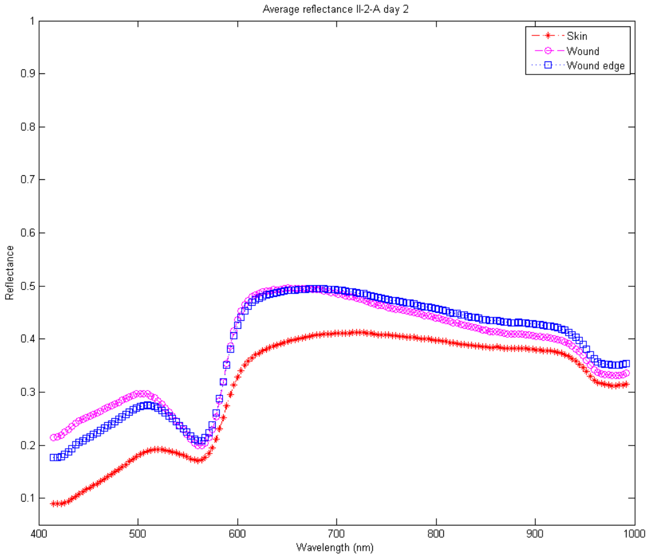

Figure 69: Average reflectance spectrum of skin, wound and wound edge for II-2-A from day 2

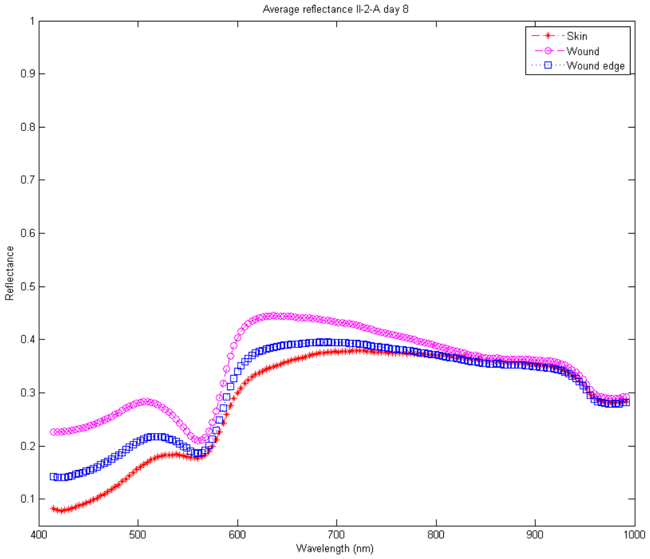

Figure 70: Average reflectance spectrum of skin, wound and wound edge for II-2-A from day 8

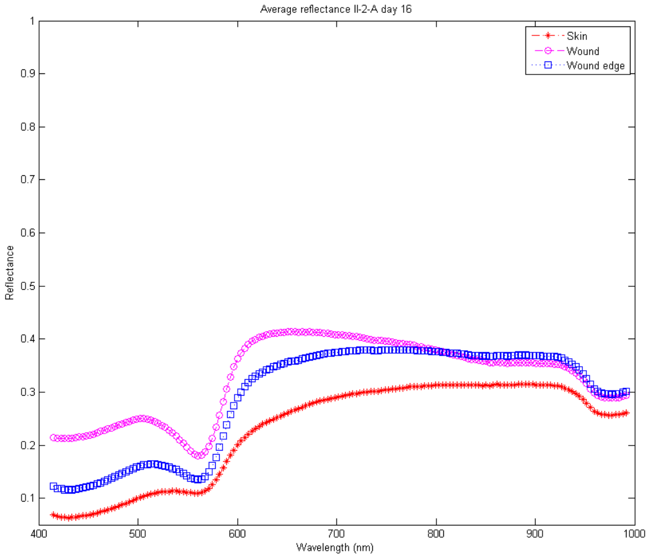

Figure 71: Average reflectance spectrum of skin, wound and wound edge for II-2-A from day 16

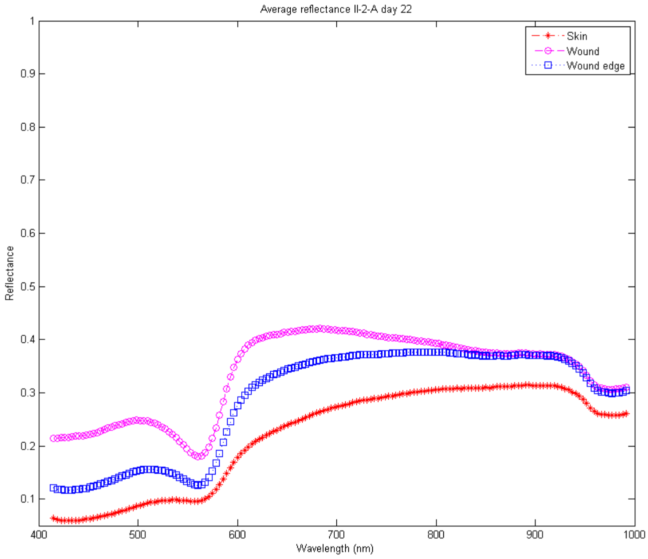

Figure 72: Average reflectance spectrum of skin, wound and wound edge for II-2-A from day 22

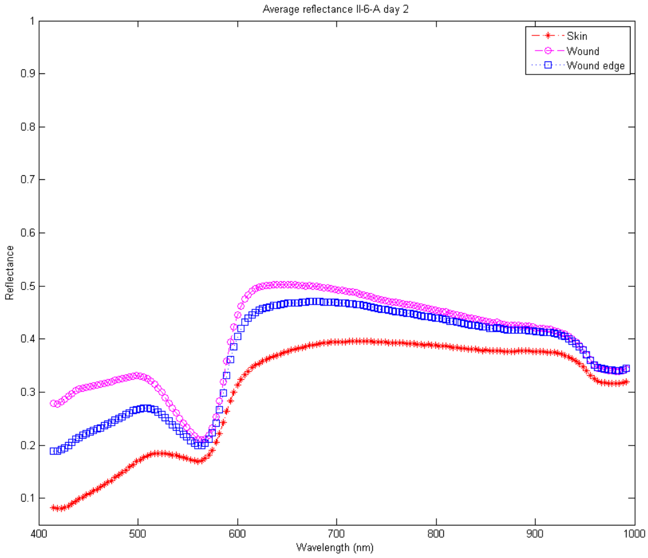

Figure 73: Average reflectance spectrum of skin, wound and wound edge for II-6-A from day 2

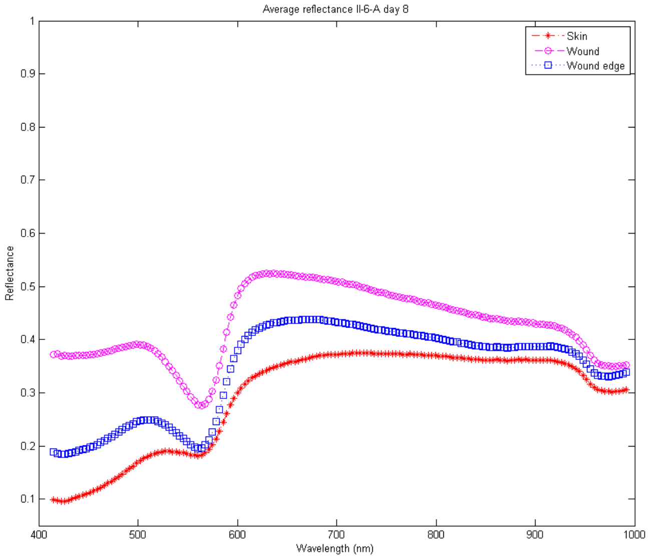

Figure 74: Average reflectance spectrum of skin, wound and wound edge for II-6-A from day 8

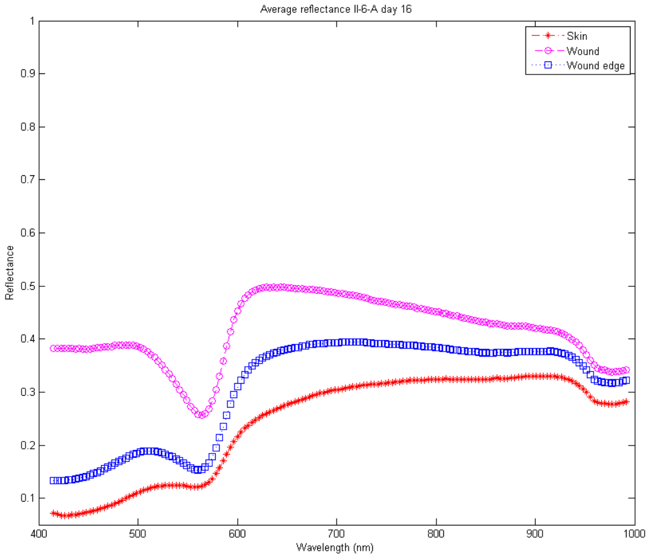

Figure 75: Average reflectance spectrum of skin, wound and wound edge for II-6-A from day 16

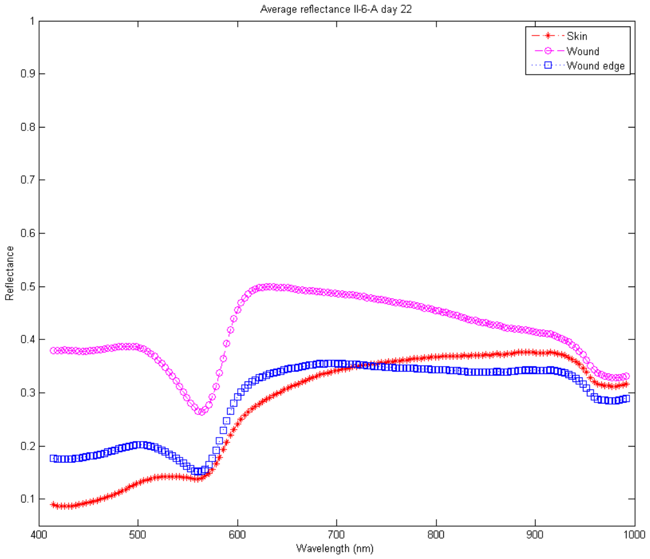

Figure 76: Average reflectance spectrum of skin, wound and wound edge for II-6-A from day 22

A.13.3 Tray III

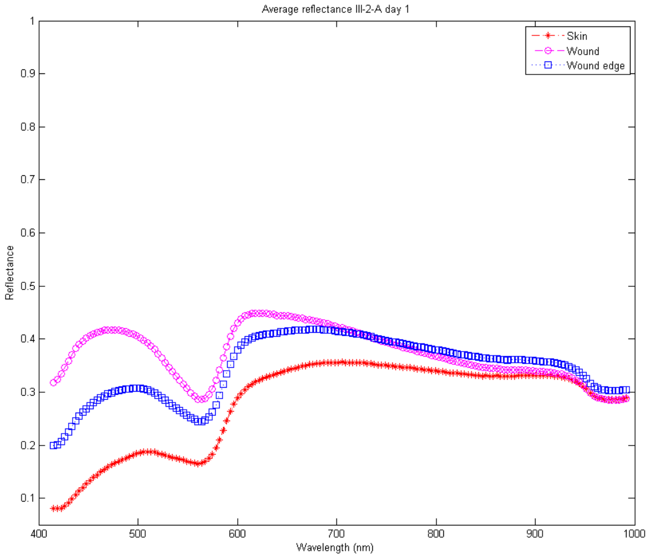

Figure 77: Average reflectance spectrum of skin, wound and wound edge for III-2-A from day 1

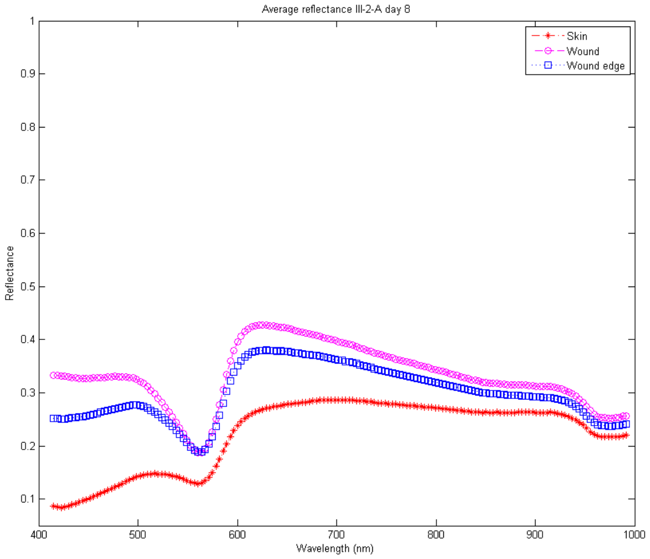

Figure 78: Average reflectance spectrum of skin, wound and wound edge for III-2-A from day 8

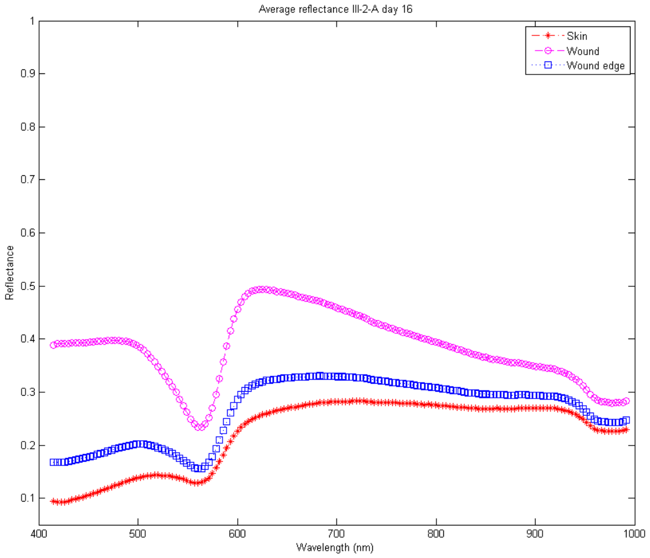

Figure 79: Average reflectance spectrum of skin, wound and wound edge for III-2-A from day 16

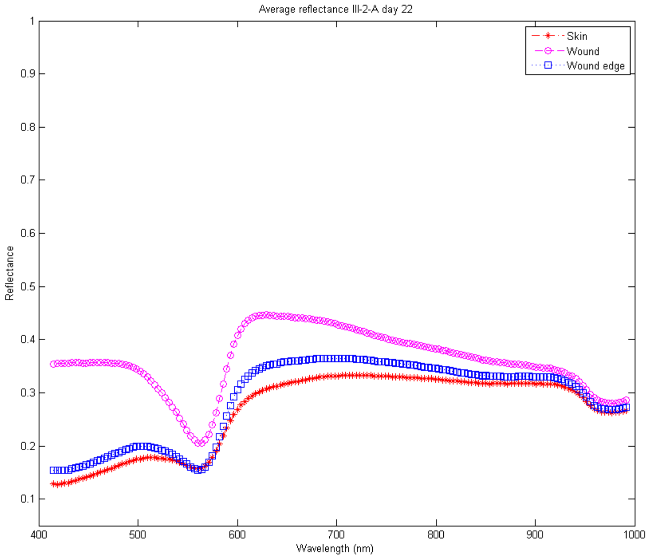

Figure 80: Average reflectance spectrum of skin, wound and wound edge for III-2-A from day 22

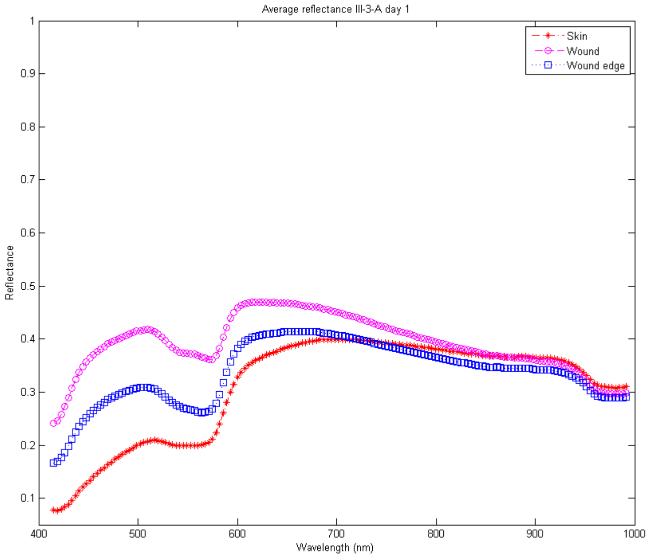

Figure 81: Average reflectance spectrum of skin, wound and wound edge for III-3-A from day 1

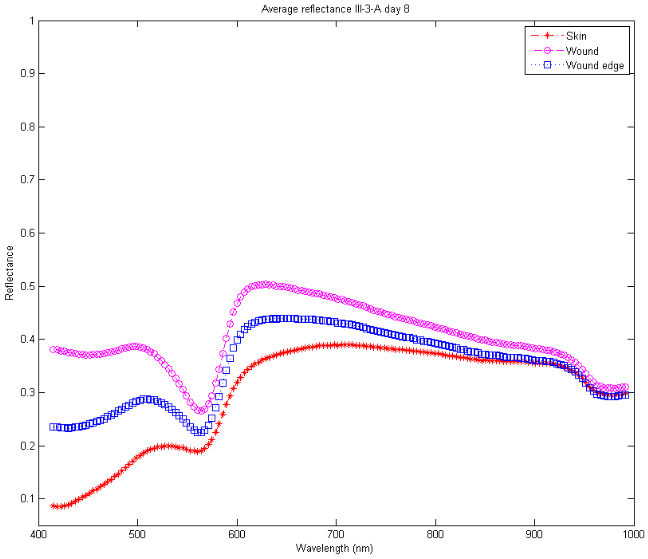

Figure 82: Average reflectance spectrum of skin, wound and wound edge for III-3-A from day 8

A.13.4 Normalized reflectance spectrums

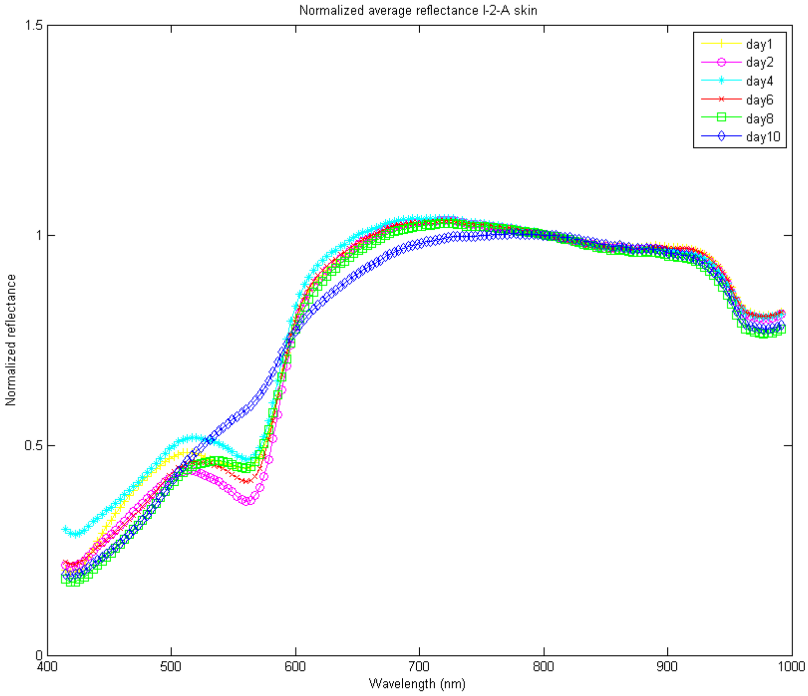

Figure 83: Normalized average reflectance spectrum of the skin I-2-A

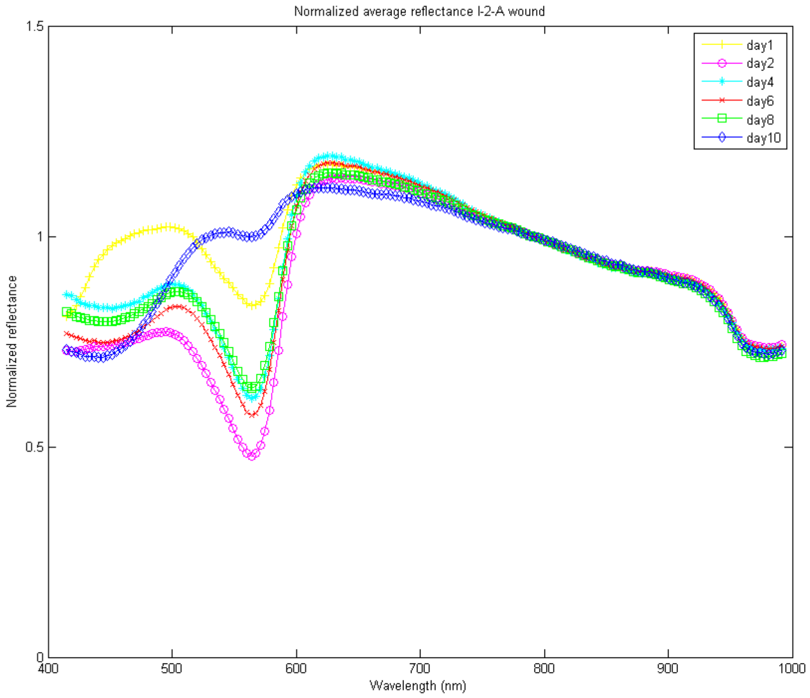

Figure 84: Normalized average reflectance spectrum of the wound I-2-A

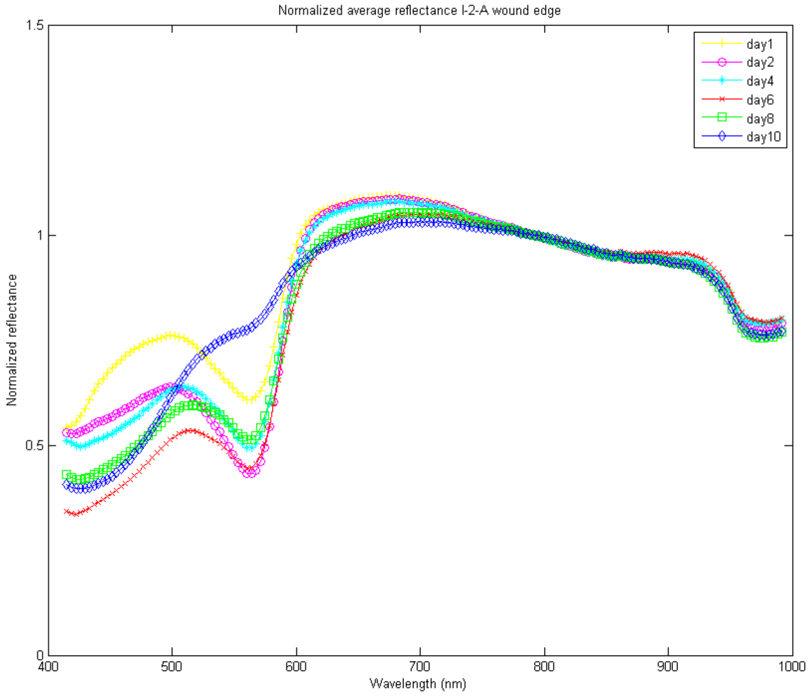

Figure 85: Normalized average reflectance spectrum of the edge I-2-A

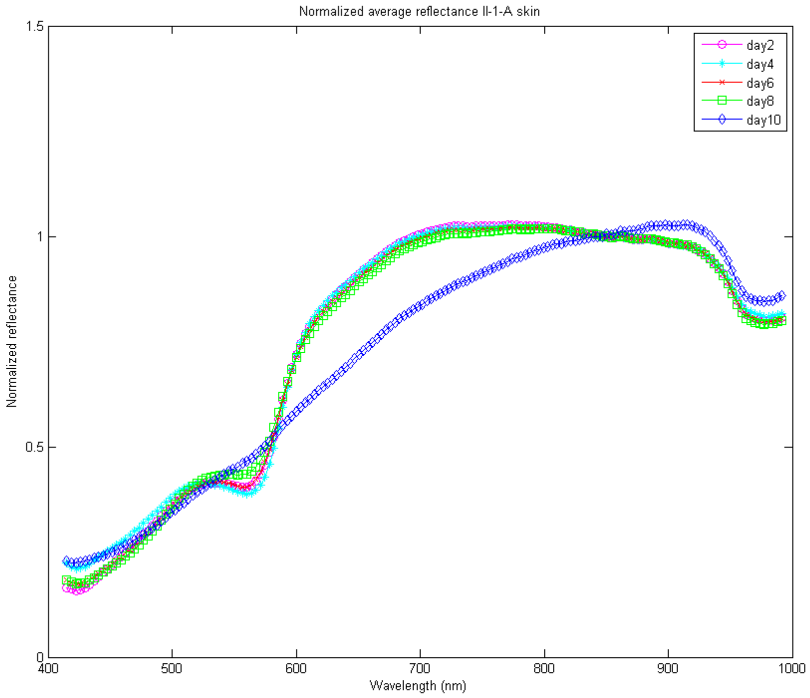

Figure 86: Normalized average reflectance spectrum of the skin II-1-A

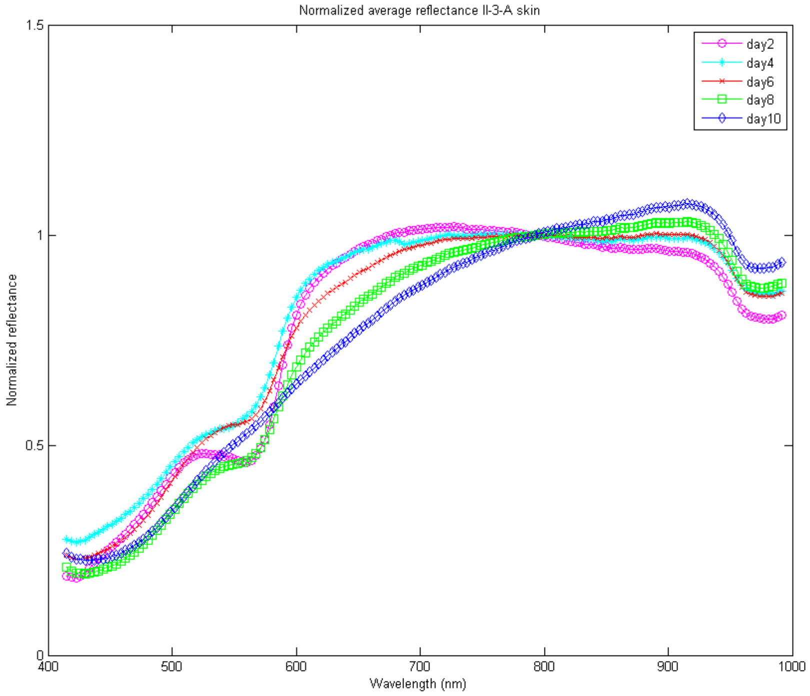

Figure 87: Normalized average reflectance spectrum of the skin II-3-A

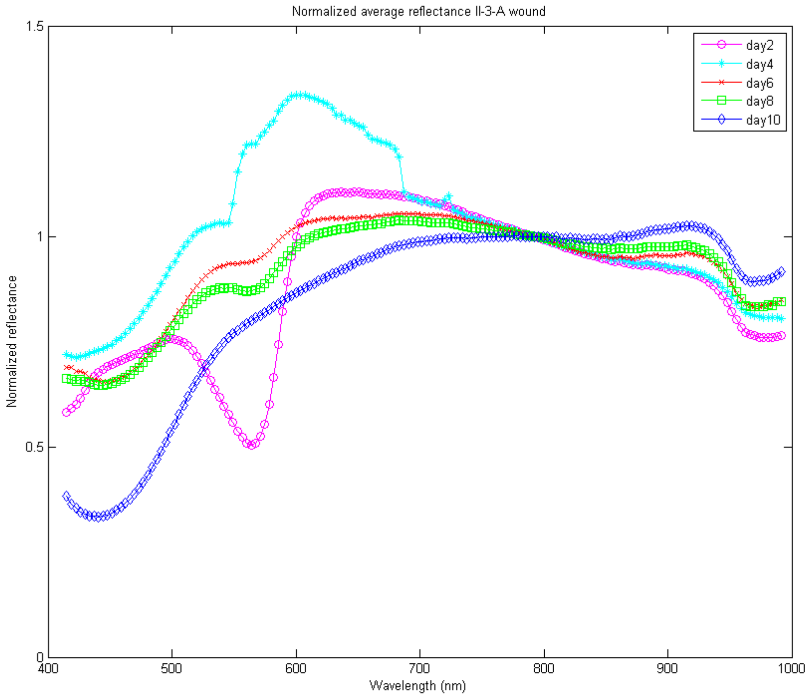

Figure 88: Normalized average reflectance spectrum of the wound II-3-A

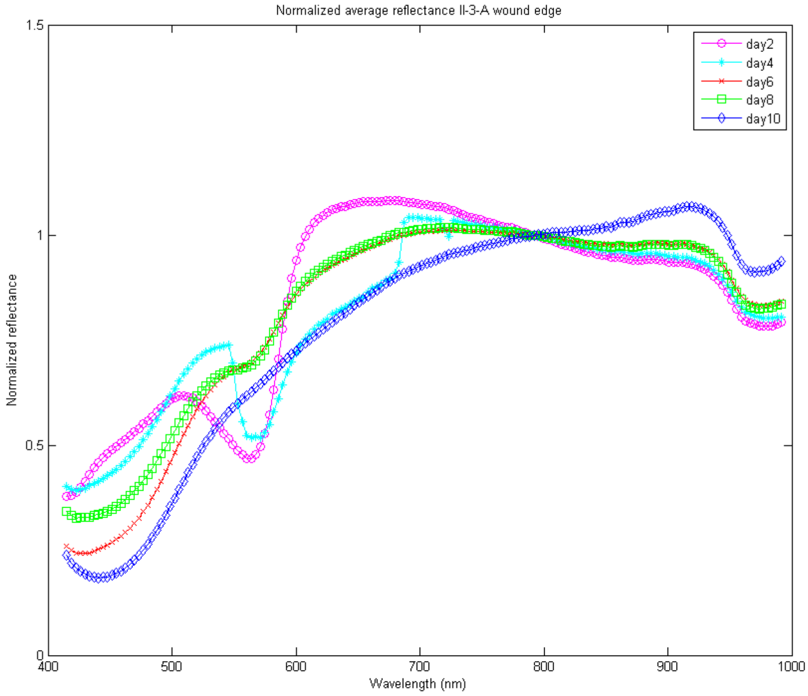

Figure 89: Normalized average reflectance spectrum of the edge II-3-A

A.14 Relative ratios SAM

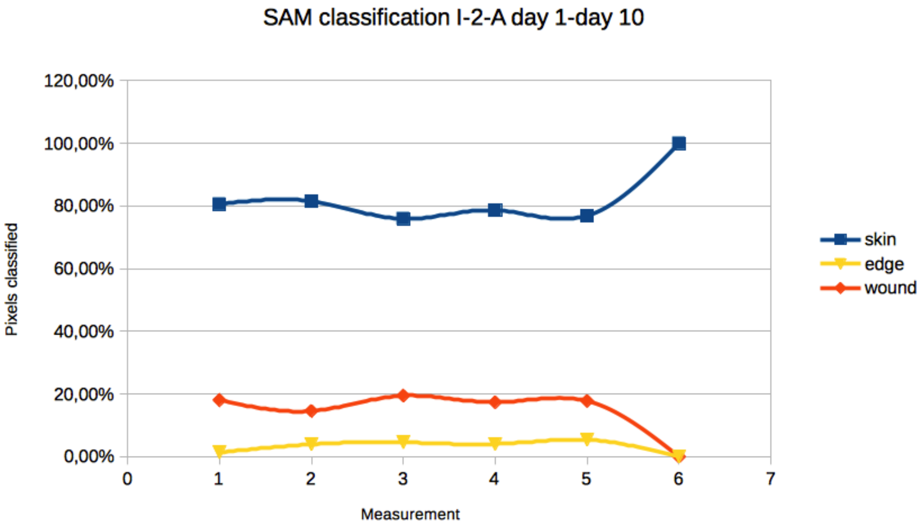

Figure 90: Relative ratios of skin, wound and wound edge from SAM of I-2-A.

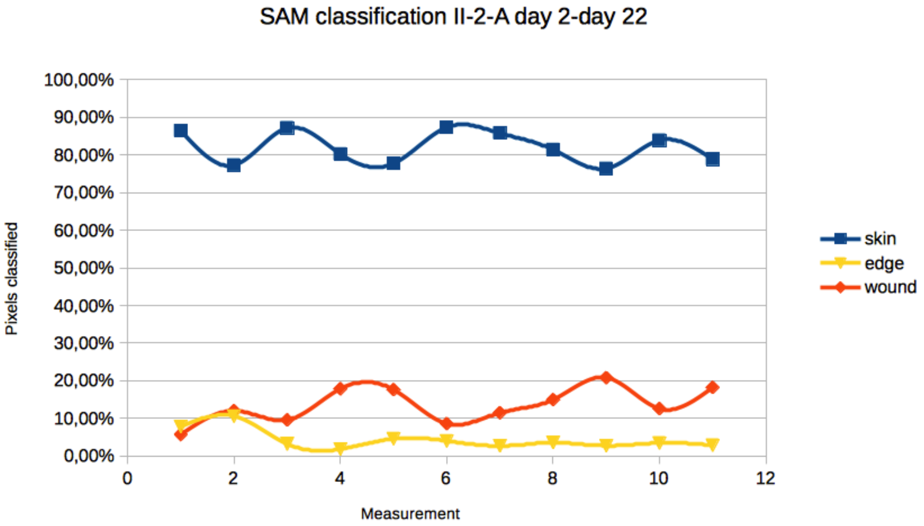

Figure 91: Relative ratios of skin, wound and wound edge from SAM of II-2-A.

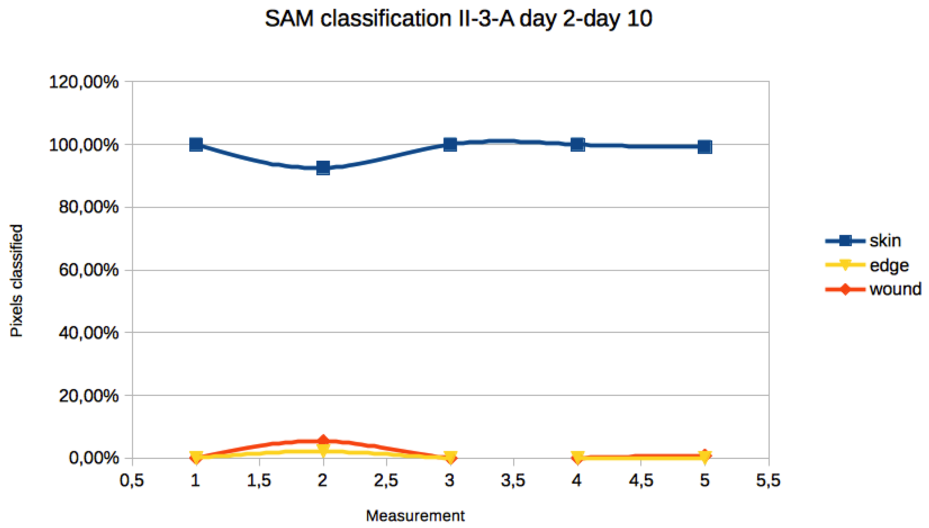

Figure 92: Relative ratios of skin, wound and wound edge from SAM of II-3-A.

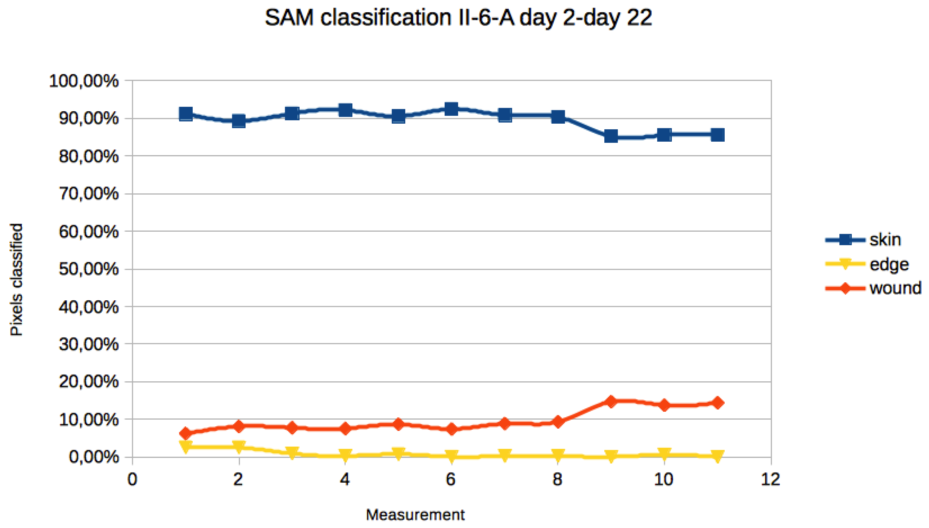

Figure 93: Relative ratios of skin, wound and wound edge from SAM of II-6-A.

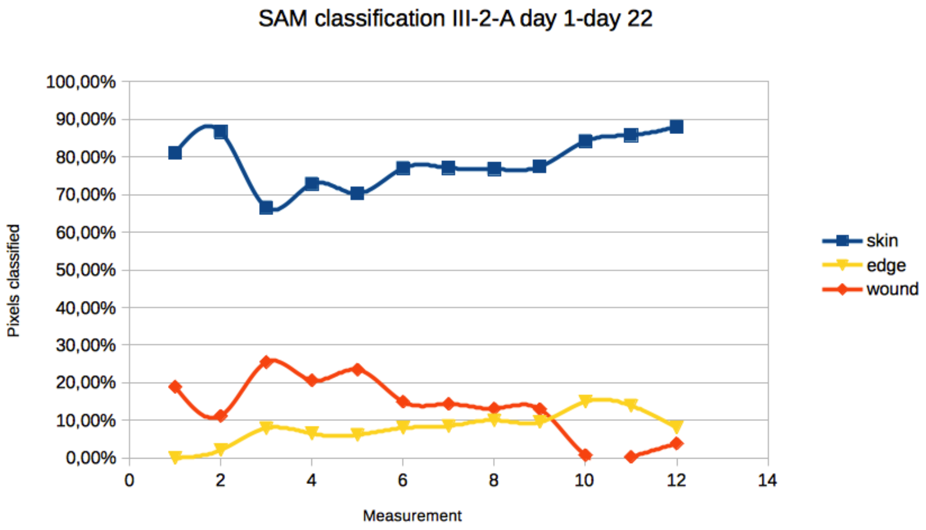

Figure 94: Relative ratios of skin, wound and wound edge from SAM of III-2-A.

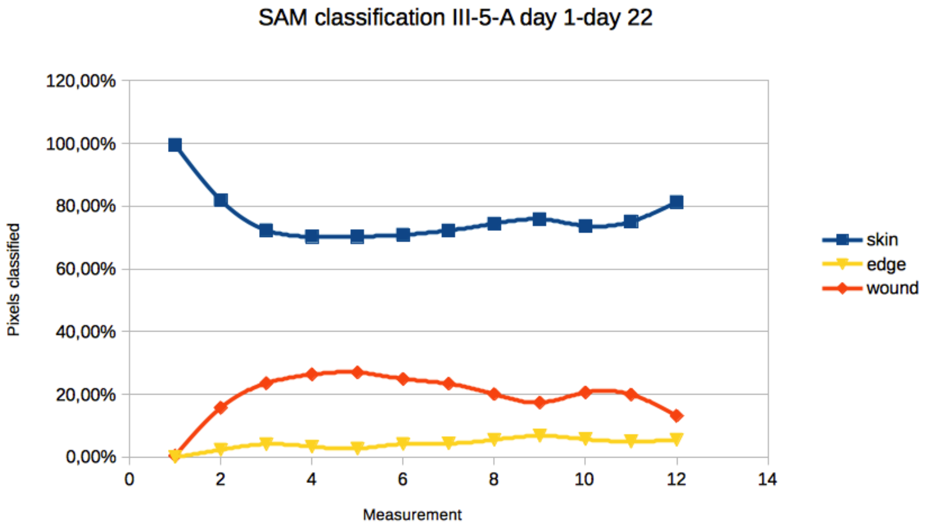

Figure 95: Relative ratios of skin, wound and wound edge from SAM of III-5-A.